

# Polar and Spinor Gases in 1D Optical Lattices

Von der Fakultät für Mathematik und Physik der  
Gottfried Wilhelm Leibniz Universität Hannover

zur Erlangung des Grades

**Doktor der Naturwissenschaften**  
**- Dr. rer. nat. -**

genehmigte Dissertation von  
M.Sc. Arturo Argüelles

geboren am 28. Februar 1978 in Bogotá, Kolumbien

2011

Referent : Prof. Dr. Luis Santos  
Koreferent : Prof. Dr. Temo Vekua  
Tag der Promotion : 28.01.2011

*...to my beloved wife, Karen.*



## Abstract

Ultracold quantum gases are manipulable and robust systems for probing fundamental condensed-matter physics problems, for applications in quantum optics and quantum information<sup>[1]</sup>, and for understanding atomic and molecular physics<sup>[2]</sup>. Loading ultracold quantum gases in artificial periodic potentials of light (optical lattices), opened novel control possibilities and, in many cases, lead to structures beyond those achievable in typical condensed-matter systems<sup>[3]</sup>. One highlight was the observation of the Mott insulator to superfluid transition<sup>[4–6]</sup> where strong correlation effects can be observed<sup>[7]</sup>. Ultracold quantum gases in optical lattices are also viewed as quantum simulators<sup>[8]</sup> since certain important Hamiltonians, which serve as a model for testing fundamental theoretical concepts of quantum many-body effects, can be accessed cleanly by optical manipulation. This Thesis is focused on the analysis of ultra-cold gases loaded in optical lattices.

The physics of dipolar gases is interesting due to the long-range anisotropic character of the dipole-dipole interactions. Polar gases in optical lattices offer fascinating new perspectives for many-body effects. In this Thesis, we study polar bosons in ladder-like potentials, which are characterized by the appearance of two kinds of superfluids: the pair-superfluid and the two-superfluid. We show that the presence of a direct pair-superfluid to Mott insulator transition significantly distorts the shape of the Mott lobes. In particular, the lowest boundary of the first Mott lobe acquires a marked re-entrant configuration which has very relevant consequences if an external harmonic trap is added to the system. The wedding cake structure of Mott and superfluid phases shows a counter-intuitive behavior, since the Mott shells broaden when the hopping increases.

Another remarkable scenario for novel many-body physics is given by spinor lattice gases, where the particles have an internal structure composed of several Zeeman sub-levels. The competition between internal (spin) and external degrees of freedom leads to a rich physics concerning both ground-state properties and dynamics. In this work we consider two different spinor lattice systems, namely, spin-3/2 fermions and spin-1 bosons. We mainly focus

on the hard-core Mott regime (one particle per site) and thus, the problems reduce to the analysis of effective spin models.

The fermionic spin-3/2 model constitutes the smallest system where hard-core fermions undergo spin-changing collisions. We consider the dynamics after a spin flip in a fully polarized gas loaded in a 1D optical lattice. We show that the interplay between quadratic Zeeman effect (QZE) and spin-changing collisions leads to the possibility of a novel type of repulsively bound states of exciton-like and bi-exciton-like excitations. These states may be highly metastable, showing intriguing dynamics depending on the system parameters.

Secondly, we analyze the ground-state magnetic properties of spin-3/2 chains in the presence of both QZE and spin-changing collisions. We consider the regime where the scattering length of the channel with total spin 2 is larger than that of total spin 0. In this regime, a dimerized (spin Peierls) state is expected in absence of an external field. We show that when the QZE grows, the system undergoes a phase transition between the dimerized phase and an isotropic pseudo-spin-1/2 Heisenberg anti-ferromagnet. We resolve this transition by means of level spectroscopy, showing that it belongs to the Kosterlitz-Thouless universality class.

Furthermore, we consider the case of repulsive spin-1 bosons in the anti-ferromagnetic domain, where for no quadratic Zeeman coupling a dimerized phase is expected. We show that for a sufficiently large positive QZE the system undergoes a Kosterlitz-Thouless transition into an  $XY$ -nematic phase. On the other hand, for large enough negative QZE, the system undergoes an Ising-like phase transition into a polar phase. Both phase transitions are again studied using level spectroscopy.

The numerical results of this Thesis were obtained with the matrix product states techniques and with Lanczos diagonalization. We describe the methods and their implementation in detail.

Keywords: Ultracold Quantum Gases, Spinor Gases, 1D systems.

## Zusammenfassung

Ultrakalte Quantengase sind manipulierbare und robuste Systeme, die die Untersuchung fundamentaler Fragen der Physik der kondensierten Materie ermöglichen, wie z. B. die Beobachtung des Überganges von einem Mott-Isolator zu einem Superfluid<sup>[4-6]</sup>. Weiterhin sind Anwendungen in der Quantenoptik und der Quanteninformation<sup>[1]</sup> sowie in der Atom- und Molekülphysik von Bedeutung. Setzt man solche ultrakalten Quantengase in ein optisches Gitter ein, so kann man künstliche Systeme der Festkörperphysik zu schaffen<sup>[3]</sup>, in denen sich Effekte starker Korrelationen beobachten lassen<sup>[7]</sup>. Ultrakalte Quantengase sind auch als Quantensimulatoren<sup>[8]</sup> geeignet, da optischer Zugriff auf spezielle Hamiltonians möglich ist. Diese Arbeit widmet sich der Untersuchung ultrakalter Gase in optischen Gittern.

Die Physik dipolarer Gase wird durch die Anisotropie und die lange Reichweite der Dipol-Wechselwirkung interessant; polare Gase in optischen Gittern bieten neue Möglichkeiten zur Untersuchung von Vielteilchen-Systemen. In dieser Arbeit untersuchen wir polare Bosonen in Leiter-ähnlichen Potentialen, bei denen zwei Arten von Superfluiden auftreten: das Paar-Superfluid und das Zwei-Superfluid. Es wird gezeigt, dass die Anwesenheit des Paar-Superfluids den Mott-Isolator-Übergang beeinflusst und die Mott-Zungen wesentlich abändert, insbesondere an der untersten Grenze der ersten Mott-Zunge. Die dort entstehende Konfiguration ist für die experimentelle Situation relevant, bei der ein externes harmonisches Potential angelegt wird. Die Torten-ähnliche Struktur der Mott- und superfluiden Phase zeigt ein bemerkenswertes Verhalten, bei dem sich die Mott-Schalen bei Erhöhung des Tunnelns vergrößern.

Spinor Gitter-Gase, bei denen Teilchen eine interne Struktur aus mehreren Zeeman-Niveaus haben, sind ein anderes interessantes Szenario für neue Vielteilchen-Physik. Der Wettbewerb zwischen den inneren (Spin) und äußeren Freiheitsgraden führt zu reichhaltiger Physik bei den Grundzustandseigenschaften und bei der Dynamik. In dieser Arbeit betrachten wir zwei verschiedene Spinor-Gittergase, nämlich Fermionen mit Spin  $3/2$  und Bosonen mit Spin  $1$ . Wir betrachten das Mott Regime (ein Teilchen pro Gitterplatz),

so dass die Fragestellung sich auf die Analyse effektiver Modelle reduziert.

Das fermionische Spin  $3/2$ -Modell stellt das kleinste System dar, bei dem Teilchen mit festem Kern so streuen können, dass der Spin geändert wird. Wir betrachten die Dynamik eines voll polarisierten Gases im eindimensionalen optischen Gitter nach einem Spinflip. Wir zeigen, dass das Wechselspiel des quadratischen Zeemaneffektes und der Spinflip-Prozesse zu einem neuartigen Bindungszustand der Anregungen von Exzitonen- und Bi-Exzitonen-Typ führt. Diese Zustände sind i. A. metastabil und führen zu interessanter Dynamik.

Als nächstes betrachten wir die magnetischen Eigenschaften des Grundzustandes der Spin- $3/2$ -Ketten im Beisein des quadratischen Zeemaneffektes und Spin-ändernder Streuung. Wir betrachten das Regime, wo die Streulänge des Kanals mit Gesamtspin 2 größer ist als die des Kanals mit Gesamtspin 0. Hier erwartet man einen dimerisierten Zustand, wenn kein externes Feld angelegt ist. Wir zeigen, dass bei Vergrößerung des quadratischen Zeemaneffektes das System einen Phasenübergang vom dimerisierten Regime zum isotropen Spin- $1/2$  Heisenberg Antiferromagneten hat. Dieser Übergang wird mit Hilfe von Niveauspektroskopie aufgelöst, und es wird gezeigt, dass er vom Kosterlitz-Thouless-Typ ist.

Desweiteren wird repulsive Spin-1 Bosonen in einer antiferromagnetischen Domäne, wo in Abwesenheit der quadratischen Zeemankopplung eine dimerisierte Phase erwartet wird, untersucht. Wir zeigen, dass für eine genügend große positive quadratische Zeemankopplung das System einen Phasenübergang vom Kosterlitz-Thouless-Typ in die  $XY$ -nematische Phase hat. Für eine genügend große negative Zeemankopplung andererseits gibt es einen Ising-artigen Phasenübergang zu einer polaren Phase. Beide Phasenübergänge werden durch Niveauspektroskopie untersucht.

Die numerischen Untersuchungen dieser Arbeit wurden mit Hilfe der Matrix Product State-Technik und der Lanczos-Diagonalisierung durchgeführt. Beide Methoden und ihre Implementierung werden im Detail beschrieben.

Schlagwörter: Ultrakalte Quantengase, Spinorgase, 1D systemen.



# CONTENTS

<b>I</b>	<b>Ultracold atoms in optical lattices</b>	<b>1</b>
I.1	The Hamiltonian . . . . .	3
I.2	Mean field theory . . . . .	4
I.3	Strong coupling expansion . . . . .	7
I.4	Correlation functions . . . . .	9
I.5	The harmonic trap . . . . .	11
I.6	Overview . . . . .	12
<b>A</b>	<b>Polar lattice bosons</b>	<b>15</b>
<b>II</b>	<b>Polar bosons in ladders</b>	<b>17</b>
II.1	Dipolar quantum gases . . . . .	17
II.1.a	Optical lattices and the DDI . . . . .	19
II.2	The Hamiltonian of two interacting chains . . . . .	20
II.3	Strong coupling analysis . . . . .	22
II.3.a	The $M\bar{n}$ . . . . .	23
II.3.b	Pair superfluid . . . . .	23
II.3.c	Two superfluid . . . . .	26
II.4	Correlation fucntions . . . . .	28
II.5	External harmonic trap . . . . .	32
<b>B</b>	<b>Dynamics of spinor lattice gases</b>	<b>35</b>
<b>III</b>	<b>Spin 3/2 fermions in 1D optical lattices</b>	<b>37</b>
III.1	Spinor gases . . . . .	37
III.1.a	Short-range interactions in spinor condensates . . . . .	38
III.2	Effective spin Hamiltonian without QZE . . . . .	40
III.3	Effective spin Hamiltonian with QZE . . . . .	41

<b>IV</b>	<b>Repulsively bound states in spin-3/2</b>	<b>47</b>
IV.1	Single-flip excitations . . . . .	49
IV.2	Exciton-biexciton repulsively bound states . . . . .	50
IV.2.a	Pairing of excitons and anti-symmetric biexcitons . . . . .	52
IV.3	Dynamical properties of the bound pairs . . . . .	57
IV.3.a	Delocalized spin-flip excitations . . . . .	58
IV.3.b	Localized spin-flip excitations . . . . .	60
IV.4	Multiple spin-flip excitations . . . . .	60
<b>C</b>	<b>Ground-state phases of spinor lattice gases</b>	<b>63</b>
<b>V</b>	<b>Mott phases of spin-3/2 chains</b>	<b>65</b>
V.1	Spin chains . . . . .	65
V.2	Quarter filling phase diagram . . . . .	66
V.3	Effective Hamiltonian . . . . .	67
V.4	Level spectroscopy. . . . .	71
V.5	Complete phase diagram . . . . .	74
<b>VI</b>	<b>AFM phases of spin-1 boson spin chains</b>	<b>77</b>
VI.1	Effective Hamiltonian in absence of QZE . . . . .	78
VI.2	System with QZE . . . . .	79
VI.2.a	$XY$ -Nematic to dimerized phase transition . . . . .	80
VI.2.b	Large- $D$ to dimerized phase transition . . . . .	82
<b>D</b>	<b>Numerics</b>	<b>87</b>
<b>VII</b>	<b>Numerical Methods</b>	<b>89</b>
VII.1	Representation and Speed-up . . . . .	89
VII.1.a	Scheme . . . . .	89
VII.1.b	Product Optimization . . . . .	91
VII.2	Matrix Product States . . . . .	92
VII.2.a	The Ansatz . . . . .	92
VII.2.b	Basic Examples of MPS . . . . .	94
VII.2.c	Orthogonalization of the states . . . . .	99
VII.2.d	Expected values . . . . .	104
VII.2.e	Time evolution . . . . .	105
VII.2.f	Ground state . . . . .	109
VII.3	Lanczos . . . . .	113
<b>VIII</b>	<b>Conclusions and outlook</b>	<b>117</b>
	<b>Bibliography</b>	<b>121</b>

## Ultracold atoms in optical lattices

Since antiquity, attempts to describe the behavior of the different materials saw the rise of several theories such as optics, thermodynamics and solid state physics. Moreover, at the beginning of the 20th century the failure on the description of physical systems gave birth to new and revolutionary ideas that later on transformed into the well-known and nowadays accepted theory of quantum mechanics. Thermodynamics was one of the most challenged theories from the classical era and, just by exploration of its frontiers, S. N. Bose was able to predict a quite spectacular phenomenon that was further developed by A. Einstein: the condensation of particles at very low temperatures into the ground state of the system<sup>[9,10]</sup>. Unfortunately for them, the realization of the so called *Bose-Einstein Condensate* (BEC) was not possible at that time, a fate in which their prediction was not alone.

Several years later when quantum mechanics was growing, band theory was able to successfully describe the electric properties of materials. In spite of that, in 1937 J. H. de Boer and E. J. W. Verwey pointed out that some transition metal oxides expected to be conductors under such theory behave actually as insulators<sup>[11]</sup>. In short, N. Mott and R. Peierls studied the problem and concluded that this anomaly is the result of neglecting, in the at that time current theory, the electron-electron interaction when sharing the same atom<sup>[12]</sup>. In 1963 J. Hubbard proposed the simplest model that takes into account both the kinetic energy of the electrons and the local interaction between them<sup>[13]</sup>. The model was solved with the use of the Bethe ansatz by Lieb and Wu in 1968<sup>[14]</sup> and since then several extensions have been done, for instance, the inclusion of long range interactions in the extended Hubbard model and the boson counterpart: *the Bose-Hubbard Hamiltonian*. However, an experimental realization with total control of the system parameters was again not yet possible.

In time, rather simple ideas from quantum optics developed into the promising technique of laser cooling that would allow, afterwards, scientists to achieve

the required temperatures for the formation of a BEC. Some of the methods are:

**Doppler cooling:** Consists on three sets of counter propagating laser beams slightly detuned from some atomic transition of the atom cloud to be cooled. When an atom travels with a finite velocity towards the beam source “sees” a higher light frequency due to the Doppler effect. In this way, the detuning can be compensated allowing a photon to be absorbed and later on emitted in some other arbitrary direction. After several absorption-emission processes the result is a decreasing kinetic energy of the atom proportional to its velocity (optical molasses). The minimum temperature achievable by this method is  $T_D = \hbar\gamma/2k_B$ , where  $\hbar$  is the reduced Planck constant,  $k_B$  is the Boltzmann constant and  $\gamma$  is the line-width of the transition<sup>[15]</sup>.

**Sisyphus cooling:** Two counter-propagating laser beams orthogonally polarized form a standing sinusoidal electric potential. When a dipole, good approximation for an atom, is moving to one of the potential maxima, it loses kinetic energy. If at the maximum the atom is optically pumped to a second (dressed) state in a potential valley, it starts to climb up once more to one potential maximum while decreasing even further its velocity. This technique reaches the recoil temperature of  $T_r = \hbar^2 k^2 / 2mk_B \sim 1\mu K$ , where  $k$  is the wave vector of the emitted photon that causes the recoil and  $m$  the mass of the particle<sup>[16]</sup>.

**Evaporative cooling:** Let us consider a gas on a trap where the particles are constantly colliding. When decreasing adiabatically the trap depth, the “hottest” particles will overpass the trap boundaries and escape carrying out an amount of kinetic energy higher than the average per particle, allowing the gas to cool down. This method allows for reaching temperatures of the order of  $\sim 100nK$ , or even lower<sup>[17]</sup>.

The development and implementation of the laser-cooling techniques by S. Chu, C. Cohen-Tannoudji and W. D. Phillips was honored with the Nobel price in 1997<sup>[18]</sup>. And thanks to it in 1995 the first BEC, by the group of E. A. Cornell and C. E. Wiemann<sup>[19]</sup> besides the independent work of W. Ketterle<sup>[20]</sup>, was achieved, and again honored with the prestigious reward<sup>[21]</sup>. Furthermore, the superfluid to Mott insulator transition was observed seven years later by M. Greiner *et al*<sup>[6]</sup>. These achievements have attracted a huge interdisciplinary interest from scientists working in disparate fields as quantum optics, condensed-matter physics, non-linear physics, quantum information and computer science. In this chapter, we focus on the basic Hamiltonian modeled by cold lattice bosons, the Bose-Hubbard Hamiltonian. We also explore numerical and analytical approaches in order to investigate the ground state properties the model.

## 1.1 The Hamiltonian

Let us consider a  $d$ -dimensional repulsively-interacting gas of spin-less bosons of mass  $m$  loaded onto an optical lattice that generates the potential

$$(1.1) \quad V_0(\vec{x}) = \sum_{j=1}^d V_{0,j} \sin^2(kx_j),$$

where  $k$  is the wave vector of the laser light: We consider an additional external trapping potential  $V_T(\vec{x})$  slowly varying in the scale of the lattice site. Thus, the Hamiltonian  $\hat{H}$  for the boson field operator  $\hat{\psi}(x)$  is<sup>[5]</sup>

$$(1.2) \quad \begin{aligned} \hat{H} = \int d^3x \hat{\psi}^\dagger(\vec{x}) & \left[ -\frac{\hbar^2}{2m} \nabla^2 + V_0(\vec{x}) + V_T(\vec{x}) \right] \hat{\psi}(\vec{x}) \\ & + \frac{2\pi a_s \hbar^2}{m} \int d^3x \hat{\psi}^\dagger(\vec{x}) \hat{\psi}^\dagger(\vec{x}) \hat{\psi}(\vec{x}) \hat{\psi}(\vec{x}), \end{aligned}$$

where the interaction potential is approximated by a short-range pseudo-potential with the  $s$ -wave scattering length  $a_s$ . Here, we consider that all the relevant energies of the system are small enough to neglect the existence of the second band, associated to the periodic potential, leaving only the first one under consideration. Within this approximation, it is possible to expand the field operator in the basis of the Wannier functions,  $\omega_i(\vec{r})$  (maximally localized at site  $i$ )

$$(1.3) \quad \hat{\psi}(\vec{x}) = \sum_i \hat{b}_i w_i(\vec{x}),$$

being  $\hat{b}_i$  the annihilator operator of a boson at the site  $i$ . The creator operator  $\hat{b}_i^\dagger$  is defined similarly. They obey, naturally, the canonical commutation relation  $[\hat{b}_i, \hat{b}_j^\dagger] = \delta_i^j$  and form the number operator  $\hat{n}_i = \hat{b}_i^\dagger \hat{b}_i$ . By plugging the definition for the field operator into the Hamiltonian (1.2) we have the well known expression of the *Bose-Hubbard Hamiltonian* (BHH)

$$(1.4) \quad \hat{H} = \sum_i \left[ -t \sum_{\delta=1}^z \left( \hat{b}_i^\dagger \hat{b}_{i+\delta} + \hat{b}_{i+\delta}^\dagger \hat{b}_i \right) + \frac{U}{2} \hat{n}_i (\hat{n}_i - 1) + \epsilon_i \hat{n}_i \right],$$

where  $z = 2d$  is the number of nearest-neighbors or coordination number explored by  $\delta$ ,  $U$  quantizes the strength of the on-site repulsion in a given lattice site,  $t$  is the hopping rate between neighboring sites, and  $\epsilon_i$  describes

the energy offset of each lattice site. The values of those parameters are

$$(1.5) \quad U = \frac{4\pi a_s \hbar^2}{m} \int d^3x |w_i(\vec{x})|^4,$$

$$(1.6) \quad t = \int d^3x w_i^*(\vec{x}) \left[ -\frac{\hbar^2}{2m} \nabla^2 + V_0(\vec{x}) \right] w_{i+\delta}(\vec{x}),$$

$$(1.7) \quad \epsilon_i = \int d^3x V_T(\vec{x}) |w_i(\vec{x})|^2 \approx V_T(\vec{x}_i).$$

In the resulting Hamiltonian of Eq. (1.4), we have neglected higher order terms like the tunneling to next-nearest neighbors and inter-site interactions, which typically are much smaller, at least when considering short-range interacting gases.

If we consider the grand-canonical ensemble of particles, we have to include the chemical potential  $\mu$  as well just by adding the term  $-\mu \sum_i \hat{n}_i = -\mu \hat{N}$ . A pioneering analysis of the system by means of *mean field theory* (MF) was done in 1989 by Fischer *et al.*<sup>[4]</sup>, showing the existence of two different phases. Let us have a look into that MF approach.

## 1.2 Mean field theory

We will focus on the ground state properties of the Hamiltonian (1.4) by means of the MF where second order coupling between the number fluctuations in different sites is totally neglected. As a result, this method is not a good approximation for one dimensional systems where the fluctuations play a key role.

Let us redefine the creation operator by using the *superfluid* (SF) order parameter

$$(1.8) \quad \Psi \equiv \langle \hat{b}_i \rangle = \langle \hat{b}_i^\dagger \rangle.$$

We introduce fluctuations around this mean value  $\hat{b}_i = \Psi + \Delta \hat{b}_i$ . Hence, the hopping term of the Hamiltonian takes the form

$$(1.9) \quad -t \sum_{i,\delta} \hat{b}_i^\dagger \hat{b}_{i+\delta} \approx zt \sum_i \left[ \Psi^2 - \Psi (\hat{b}_i^\dagger + \hat{b}_i) \right].$$

Then, the Hamiltonian becomes the sum over local Hamiltonians  $\hat{H} = \sum_i \hat{H}_i$  where at each site we have  $\hat{H}_i = \hat{H}_0 + t\hat{H}_1$ . After setting  $\epsilon_i = 0$  and dropping the site dependence, we thus have

$$(1.10) \quad \hat{H}_0 = \frac{U}{2} \hat{n}(\hat{n} - 1) - \mu \hat{n} + zt \Psi^2,$$

$$(1.11) \quad \hat{H}_1 = -zt \Psi (\hat{b}^\dagger + \hat{b}).$$

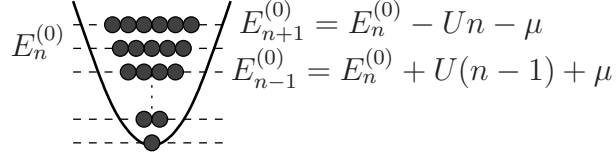


Figure 1.1: On-site eigenstates for the Bose-Hubbard Hamiltonian with  $t = 0$ . When considering the state  $|n\rangle$  with  $n$  particles, the virtual states are  $|n-1\rangle$  and  $|n+1\rangle$  in the mean field approximation.

The main features of this problem can be analyzed by perturbation theory on the hopping parameter  $t$ , which is considered small-enough. The first step is to read-off the eigen-energies of the Hamiltonian  $\hat{H}_0$  which is already diagonal in the Fock basis,  $E_n^{(0)} = Un(n-1)/2 - \mu n + zt\Psi^2$  and apply the well-known second order expression

$$(1.12) \quad E_n^{(2)} = \sum_{\nu} g_{\nu} \frac{|\langle n | \hat{H}_1 | \nu \rangle|^2}{E_n^{(0)} - E_{\nu}^{(0)}}.$$

In this case, the virtual states  $|\nu\rangle$  are the result of the ladder operators that appear on the hopping term  $\hat{H}_1$  which act on the unperturbed eigen-states as

$$(1.13) \quad \hat{b}^{\dagger} |n\rangle = \sqrt{n+1} |n+1\rangle,$$

$$(1.14) \quad \hat{b} |n\rangle = \sqrt{n} |n-1\rangle,$$

whose energies are depicted in Fig. 1.1 and their multiplicity is  $g_{\nu} = 1$ . Then, after putting together all this, the expression for the energy up to second order in the hopping parameter  $t$  for a state with an average number of particles  $\bar{n}$  is given by

$$(1.15) \quad E_{\bar{n}} = \frac{U}{2} \bar{n}(\bar{n}-1) - \mu \bar{n} + zt\Psi^2 \underbrace{\left( 1 + \frac{ztn}{U(\bar{n}-1) + \mu} - \frac{zt(n+1)}{U\bar{n} - \mu} \right)}_{r_{\bar{n}}}.$$

The ground state requires this energy to be minimal, thus we have three possibilities. If

**$r_{\bar{n}} > 0$**  The energy is minimized only if  $\Psi = 0$ . This means that the number of particles has no fluctuations and, since all the sites are considered identical ( $\epsilon_i \equiv 0$ ), the total number of particles is commensurate with the total number of sites  $L$ , or in other words  $\hat{N} = \bar{n}L$  with  $\bar{n}$  integer. Hence, even though there is a finite hopping, the particles tend to be very localized making the system fall into a Mott insulator (MI) phase.

**$r_{\bar{n}} < 0$**  In this case, in order to minimize the energy  $\Psi \neq 0$ . Local fluctuations in the number of particles are allowed and, although  $[\hat{H}, \hat{N}] = 0$ , the

total number of particles is no longer commensurate with the system size. This fluctuation in the number of particles comes from the fact that they move throughout the lattice and the system enters into the superfluid state.

$\mathbf{r}_{\bar{n}} = \mathbf{0}$  When the superfluid to Mott insulator phase transition takes place, the energy of the two phases coincide. This will allow us to depict the ground-state phase diagram for the system since this is exactly the transition boundary.

After setting  $r_{\bar{n}} = 0$  and equating for  $\tilde{\mu} \equiv \mu/U$  as a function of  $\bar{n}$  and  $\tilde{t} \equiv t/U$  we have

$$(1.16) \quad \tilde{\mu}_{\pm} = \frac{1}{2} \left[ (2\bar{n} - 1) - z\tilde{t} \pm \sqrt{1 - 2z\tilde{t}(2\bar{n} + 1) + (z\tilde{t})^2} \right].$$

In Fig. 1.2 the parabolic form of the MI lobes is depicted from Eq. (1.16) taking  $z = 4$  and  $\bar{n} = 0, 1, 2, 3$ .

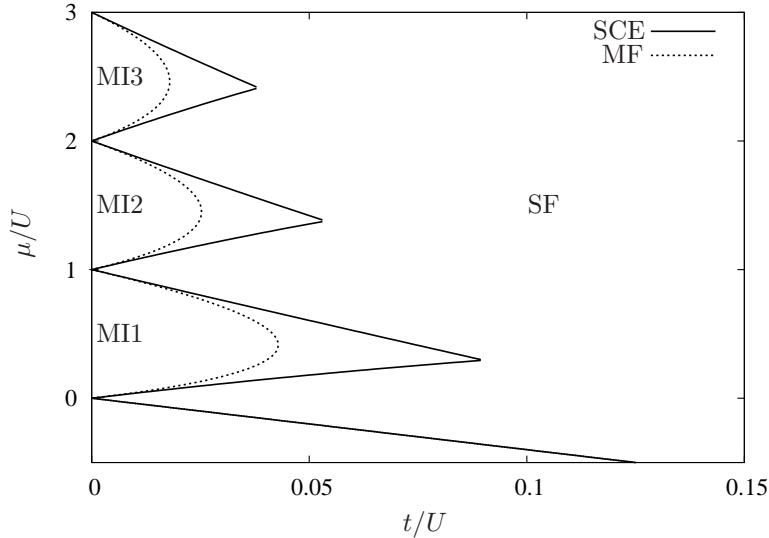


Figure 1.2: MI and SF boundaries for two dimensional lattices showing the difference between MF and SCE predictions.  $MI\bar{n}$  is the Mott insulating lobe with  $\bar{n}$ -commensurate.

In the following two sections we introduce, in the frame work of the Bose-Hubbard model, two important ideas which we will employ throughout this work. They are the strong-coupling expansion and the correlation functions.



### I.3 Strong coupling expansion

Perturbation theory in the hopping term can be further exploited to approximately calculate the phase boundaries between the MI and the SF without neglecting the quantum fluctuations in the way MF does. This idea was developed by J. K. Freericks and H. Monien in 1996<sup>[22]</sup> giving very good analytical results for both one and higher dimensional systems.

The main idea is to take the Hamiltonian (I.4) in the atomic limit, where only the on-site part is left since  $t \rightarrow 0$ , as the initial Hamiltonian. Then, use the kinetic term as a perturbation on the eigen-states of the atomic part. Three initial states are considered: the unperturbed MI, characterized by a commensurate filling, and defective superfluid states with an extra particle or an extra hole respectively.

Let us first consider the Mott state with  $\bar{n}$  particles per site,  $MI\bar{n}$ , given by the expression

$$(I.17) \quad |\phi_{MI}(\bar{n})\rangle^{(0)} = \prod_i \frac{1}{\sqrt{\bar{n}!}} (b_i^\dagger)^{\bar{n}} |\emptyset\rangle,$$

where  $|\emptyset\rangle$  denotes the vacuum state. The action of the kinetic term on this state is to make a particle hop into any of the  $z$  neighboring sites. This process, regarding Eq. (I.12), can be summarized as follows

State	$\tilde{E}_\nu$	$g_\nu$	$-\tilde{E}_\nu^{(2)}/z\tilde{t}^2$
	$\tilde{E}_{MI}^{(0)} = \bar{n}L [(\bar{n} - 1)/2 - \tilde{\mu}]$		
	$\tilde{E}_{Mott}^{(0)} + 1$	$zL$	$L\bar{n}(\bar{n} + 1)$

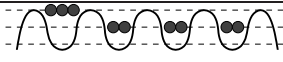
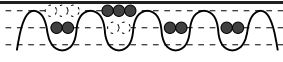
where the tilde denotes the normalization in units of the on-site repulsive interaction  $U$ . By plugging these results into the perturbation term (I.12), we obtain for the Mott state energy up to second order in the hopping

$$(I.18) \quad \tilde{E}_{MI}(\bar{n}) = \bar{n}L \left[ \frac{1}{2}(\bar{n} - 1) - \tilde{\mu} - z\tilde{t}^2(\bar{n} + 1) \right].$$

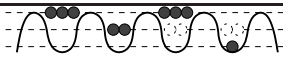

An identical procedure is applied to the defect state

$$(I.19) \quad |\phi_P(\bar{n})\rangle^{(0)} = \frac{1}{\sqrt{L}} \sum_i \frac{\hat{b}_i^\dagger |\phi_{MI}(\bar{n})\rangle^{(0)}}{\sqrt{\bar{n} + 1}},$$

that describes a superfluid system with an extra particle on top of the  $MI\bar{n}$ . It is important to note that in this case we have a contribution from the first order in perturbation theory, as shown in the next scheme, since one hopping of the extra particle on top of the Mott gives an state that also lies on the same manifold as the original one.

Initial state	$\tilde{\Delta}_p^{(0)}$
	$\bar{n} - \tilde{\mu}$
Equivalent state	$-\tilde{E}_p^{(1)}/z\tilde{t}$
	$\bar{n} + 1$

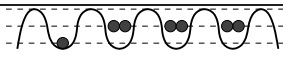

where  $\tilde{\Delta}_p = \tilde{E}_p^{(0)} - \tilde{E}_{\text{MI}}^{(0)}$ . The second order in perturbation theory is more elaborated than in the case of the Mott, but still quite straightforward. A picture of the virtual states, the energies and the degeneracy is presented in the next table.

Virtual states	$\tilde{E}_\nu$	$g_\nu$	$-\tilde{E}_\nu^{(2)}/z\tilde{t}^2$
	$\tilde{E}_p^{(0)} + 1$	$z(L-1)$	$(L-1)\bar{n}(\bar{n}+1)$
	$\tilde{E}_p^{(0)} + 2$	$z$	$\frac{\bar{n}(\bar{n}+2)}{2}$

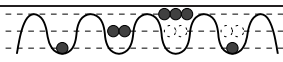
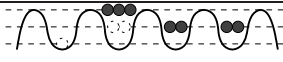
In the same way as in the MF procedure, by equating the MI energy with the SF energy and solving for  $\tilde{\mu}$  we are able to predict, within the approximation, the upper boundary of the MI lobe. The strong coupling expansion (SCE) thus gives

$$(1.20) \quad \tilde{\mu}_+(\bar{n}) = \bar{n} - (\bar{n} + 1)z\tilde{t} + \frac{1}{2}\bar{n}^2 z\tilde{t}^2.$$

The procedure is finally applied to an state with an extra hole on top of the MI  $\bar{n}$ . Again, first and second order terms in perturbation theory have a non vanishing contribution. First we have the hole hopping that keeps the system in the same manifold.

Initial state	$\tilde{\Delta}_h^{(0)}$
	$-(\bar{n} - 1) + \tilde{\mu}$
Equivalent state	$-\tilde{E}_p^{(1)}/z\tilde{t}$
	$\bar{n}$

And for the second order, the states that are connected by the Hamiltonian with  $|\phi_p(\bar{n})\rangle^{(0)}$  that are out of the manifold, their degeneracy and contribution are

Virtual states	$\tilde{E}_\nu$	$g_\nu$	$-\tilde{E}_\nu^{(2)}/z\tilde{t}^2$
	$\tilde{E}_h^{(0)} + 1$	$z(L-1)$	$(L-1)\bar{n}(\bar{n}+1)$
	$\tilde{E}_h^{(0)} + 2$	$z$	$\frac{(\bar{n}^2-1)}{2}$

Combining the matrix elements and the energies we retrieve, finally, the expression for the lower boundary of the Mott is

$$(1.21) \quad \tilde{\mu}_-(\bar{n}) = (\bar{n} - 1) + \bar{n}z\tilde{t} - \frac{1}{2}z\tilde{t}^2(\bar{n} + 1)^2.$$

In Fig. 1.2 the SCE predictions are compared with the ones of MF and in Fig. 1.3 with those of the *matrix product state* (MPS) technique described below. From the figures is clear that the SCE approach is far better approximation than the MF one since the description of the boundaries agrees with the MPS results almost up to the tip. Moreover, the use of higher order SCE could lead to even better agreements.

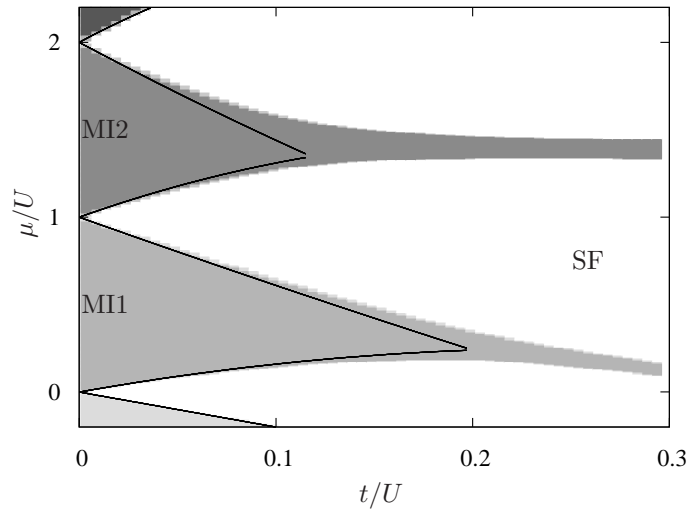


Figure 1.3: Comparison between SCE calculation of the Mott lobes from Eq. (1.20) and (1.21) for 1D lattices,  $z = 2$ , and MPS numerical results, which are depicted as follows, in grey scale the commensurate fillings and in white the incommensurate fillings. From the fact that  $L = 18$ , the width of the commensurate SF is finite and the tip is not spot directly. However, for lower values of  $t/U$  we can see a very good agreement.

## 1.4 Correlation functions

In this section, we will briefly discuss the behavior of correlation functions in 1D systems of lattice bosons, which characterize the properties of the different phases. To this aim, we introduce the single-particle correlation function

$$(1.22) \quad \mathcal{G}(\Delta) = \langle \hat{b}_0^\dagger \hat{b}_\Delta \rangle,$$

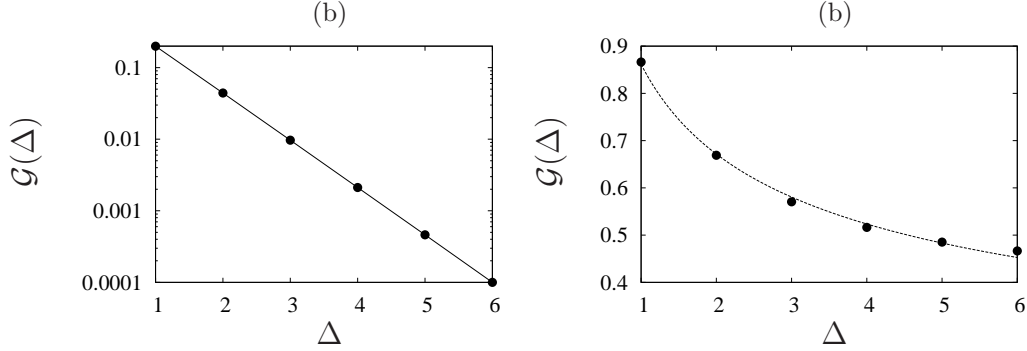


Figure 1.4: Plot of the correlation function (1.22) for the ground state of the Bose-Hubbard Hamiltonian using variational MPS calculation taking a system size of  $L = 60$ , an entropy parameter  $\chi = 20$  and a hopping  $t = 0.05$ , within both (a) the Mott-Insulator phase for  $\mu = 1/2$  where it shows an exponential decay, and (b) the superfluid phase for  $\mu = 1$  where an algebraic decay is observed. The line represents the best fit.

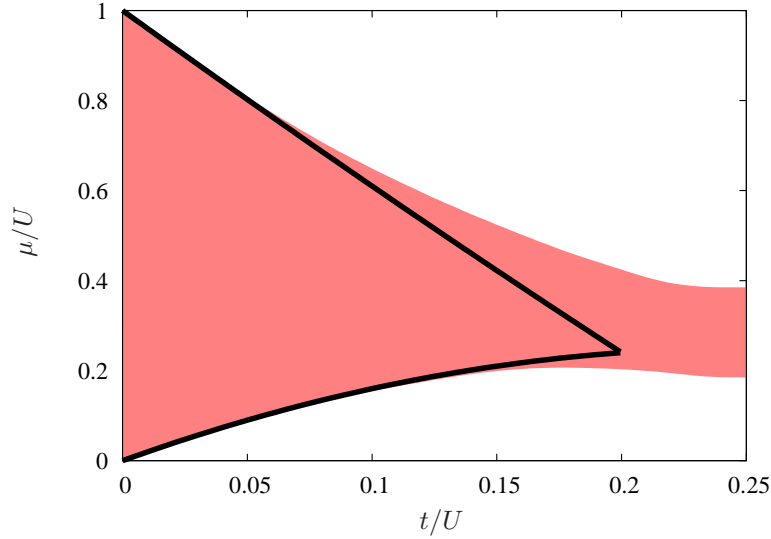


Figure 1.5: Comparison between MPS and SCE calculation of the phase-space for the Bose-Hubbard model. In gray the set of states with a correlation function  $\mathcal{G}(\Delta)$  that decays exponentially and on white those with an polynomial decay.

where 0 indicates the center of the chain. This correlation function decays exponentially to zero within the Mott insulator regime. On the other hand, it has a Luttinger-liquid (polynomial) decay within the superfluid region.  $\mathcal{G}(\Delta)$  may be calculated by means of matrix product state techniques (MPS), described in detail in chapter VII. Figure 1.4 shows the behavior of the single-particle correlation function for a MI case and for a SF one. As expected, the distinction between the two phases can be clearly seen even at the Mott tip where

the average number of particles per site gives no difference. In figure 1.5 the results of the analysis of the correlation function are presented besides the SCE results. A very good agreement is clear.

A particular value of the correlation function is  $\mathcal{G}(0) = \langle \hat{n}_0 \rangle$ , which is the density at the middle of the chain. A parameter space scan of it is depicted in Fig. 1.3 showing, as mentioned above, an excellent agreement with the SCE results.

## 1.5 The harmonic trap

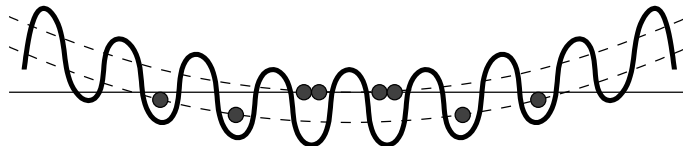


Figure 1.6: Trapping potential plus the optical lattice. A simple local density approximation predicts that the state of the system will show a *wedding cake* shape in the density.

Up to this point we have just considered the homogeneous Bose-Hubbard Hamiltonian ( $\epsilon_i = 0$ ), showing the existence of two distinct phases. In the presence of an additional confinement, that varies slowly in comparison to the lattice parameter, we may approximate, as in Eq. 1.7,  $\epsilon_i \approx V_T(\vec{x}_i)$ . This leads to an effective local chemical potential  $\mu(\vec{x}_i) = \mu_0 - V_T(\vec{x}_i)$ , where  $\mu_0$  is the global chemical potential. As a result, the system explores different regions of the homogeneous phase diagram depending on spatial position. Therefore, a wedding-cake structure of Mott plateaux and SF regions occurs. A scheme of this idea is shown in Fig. 1.6.

A local density approximation can be done in order to calculate the density profile from bosonization techniques and the result is very close to the one retrieved from the DMRG method<sup>[23]</sup>. This DMRG is equivalent to the variational MPS method we employed already and we can directly over-impose the harmonic trapping potential to the Hamiltonian (1.4) by setting  $\epsilon_i = \epsilon_0 i^2$ .

The MPS results of the density profile  $\langle \hat{n}_i \rangle$ , for a harmonic confinement, are presented in Fig. 1.7 for several values of the hopping  $t$ . A wedding-cake structure is clearly visible. When the parameter  $t$  increases, the *Mott-shells* get thinner and finally melt down. This scenario is very intuitive since the mobility of the particles increases and the insulator is thus less stable.

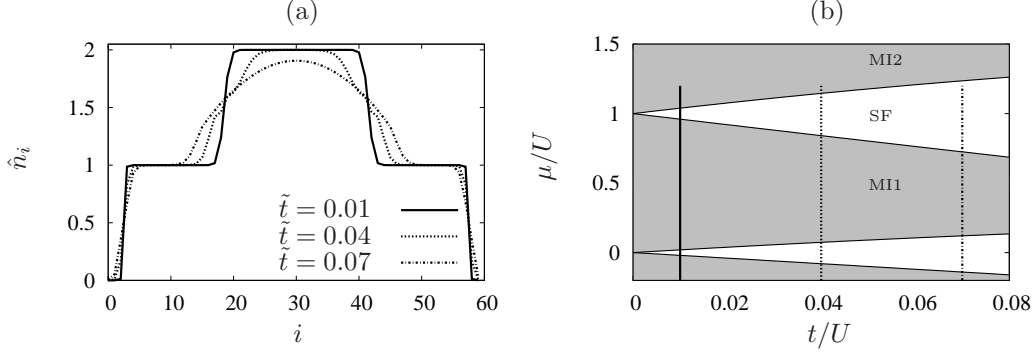


Figure 1.7: Variational-MPS results for a one-dimensional Bose gas in presence of an optical lattice and a harmonic trap. (a) Density profile of the ground state with  $L = 60$ . The wedding cake structure is clearly visible. (b) Scheme of the Mott phases and the scan done by the trap for the three different values of  $\tilde{t} = t/U$ .

## 1.6 Overview

This thesis is devoted to the physics of ultra-cold gases in optical lattices. And thus, it is structured as follows:

Chapter II deals with the problem of polar bosons loaded into ladder-like lattices. By means of MPS and SCE calculations, we determine the phase diagram, characterized by three phases. A pair-superfluid phase characterized by superfluid of composites with a particle at opposite legs, a two-superfluid that presents individual superfluids at each legs, and the Mott insulator. We show that the direct transition between the Mott insulator to pair-superfluid results in distorted Mott lobes, which may acquire a remarkable re-entrant character. The later scenario leads to a counter-intuitive behavior of the Mott plateaux in the presence of an external harmonic confinement.

In chapter III we briefly introduce spinor gases and we calculate the effective Hamiltonian for spin-3/2 fermions in 1D optical lattices. Then, we analyze in chapters IV and V the ground-state magnetic properties of spin-3/2 chains in the presence of both QZE and spin-changing collisions. In particular, we study the regime  $a_2 > a_0$ , where  $a_F$  is the  $s$ -wave scattering length for the collision channel with total spin  $F$ . In this regime, a dimerized (spin Peierls) state is expected in absence of QZE. Our results show that when the QZE grows, the system undergoes a phase transition between the dimerized regime and an isotropic pseudo-spin-1/2 Heisenberg anti-ferromagnet. We analyze this phase transition by means of level spectroscopy showing that it belongs to the Kosterlitz-Thouless universality class.

Chapter VI is devoted to the case of repulsive spin-1 bosons in the anti-ferromagnetic domain. In the absence of QZE a dimerized phase is expected. We show that for a sufficiently large and positive QZE the system undergoes

a Kosterlitz-Thouless phase transition to an  $XY$ -nematic phase. On the contrary, for large enough but negative QZE, the system undergoes an Ising-like phase transition into a polar phase. Both transitions are studied using level spectroscopy.

The numerical results presented throughout the Thesis have been obtained with both matrix-product-states techniques and Lanczos diagonalization. In chapter VII we describe the methods and the details of their implementation.





PART A

POLAR LATTICE BOSONS



## Polar bosons in optical ladder-like potentials

We analyze the Mott-insulator phases of dipolar boson gases placed in two parallel but unconnected 1D optical lattices. The short-range interactions keep the 1D systems independent, whereas the long-range dipole-dipole interaction induces a direct Mott-insulator to pair-superfluid transition which significantly modifies the boundaries of the Mott insulator phase. In particular, the lowest boundary of the first Mott lobe may acquire a re-entrant shape as a function of the hopping rate, which is retained in higher dimensions. We discuss the consequences of this effect on the spatial Mott-insulator plateaux in experiments with additional harmonic confinement, showing that counter-intuitively the plateaux may become wider for increasing hopping. These results are also applicable to non-dipolar boson-boson mixtures.

### II.1 Dipolar quantum gases

We have already analyzed how the interactions play a significant role in the physics of ultracold particles. In particular for the case of 1D optical lattices, we have seen that by tuning the on-site interaction strength  $U$ , the BHH presents a phase transition between an insulating Mott regime and a superfluid one. However, this interaction is short range and therefore its action is limited to one-site effects. Interestingly, long-range effects, in particular the dipole-dipole interaction (DDI), cannot always be neglected. Furthermore, the DDI may significantly alter the physics of quantum gases, as it has been shown in recent analytical studies and experiments<sup>[24]</sup>.

Apart from the long range, one of the main characteristics of the DDI is that it is anisotropic. This fact can be intuitively understood by thinking in two side-by-side dipoles as shown in figure II.1. If they are parallel to each other then they repel, as in (a). On the other hand, if they are anti-parallel then they attract each other, as in (b). In the case of parallel (polarized) dipoles, their relative position is also important, since side-by-side they repel each other, but in a head-to-tail configuration they attract each other, as in

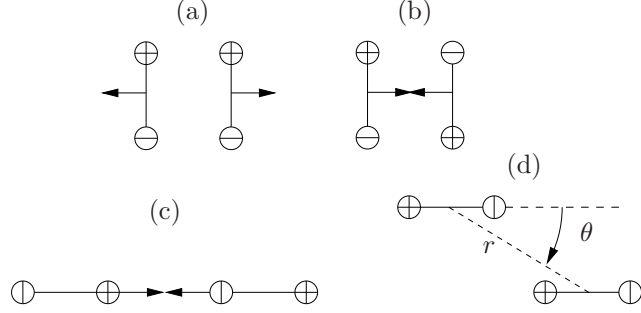


Figure II.1: Anisotropy of the dipolar-dipolar interaction.

(c) . Henceforth we will consider polarized dipoles, like the ones in (d), for which the interaction potential is

$$(II.1) \quad V_{\text{DDI}}(\theta, r) = \frac{C_{\text{dd}}}{4\pi} \frac{1 - 3 \cos^2 \theta}{r^3}.$$

For magnetic dipoles  $C_{\text{dd}}$  is  $\mu_0 \mu^2$ ,  $\mu_0$  is the vacuum permeability and  $\mu$  is the permanent magnetic moment of the particles. In the case of electric dipoles with moment  $d$ ,  $C_{\text{dd}} = d^2/\varepsilon_0$  where  $\varepsilon_0$  is the vacuum permittivity. Equation (II.1) shows clearly that the DDI is both long-range, since it decays as  $1/r^3$ , and anisotropic, as can be seen from its  $1 - 3 \cos^2 \theta$  dependence. Note in particular that for the magic angle  $\theta_m$ , defined by  $\cos^2 \theta_m = 1/3$ , the DDI vanishes. This fact is employed later on in this chapter.

The peculiar behavior of the DDI has important consequences in the BEC stability<sup>[25-27]</sup> and excitations<sup>[28]</sup>. BEC stability has been recently studied in experiments with Cr in 3D traps, where the BEC may become unstable against collapse<sup>[29]</sup> and in 2D traps, where the DDI may allow instabilities without collapse characterized by the formation of an inelastic soliton gas<sup>[30]</sup>. Particularly dipolar BECs present a non-local non-linearity, resembling nematic crystals<sup>[31]</sup>, that leads to novel physics, such as stable 2D bright solitons<sup>[32,33]</sup> and stable 3D dark solitons<sup>[34]</sup>. Moreover, the momentum dependence of the DDI gives place to the appearance of a roton-like minimum in the dispersion law of elementary excitations, which may result in *roton instability*<sup>[35]</sup>. This instability may lead either to local collapses<sup>[36]</sup> or to stabilized modulated density profiles in sufficiently tight traps<sup>[37]</sup>. The influence of the DDI is also crucial in the properties of Fermi gases<sup>[38-43]</sup>, and in the physics of strongly correlated systems<sup>[44-48]</sup>.

Due to their strong electric dipole moment, polar molecules are ideal candidates to show dipolar effects and thus quantum degenerate gases of polar molecules are one of the primary targets of current experiments. Progress has been made recently in cooling of molecules, with techniques such as stark deceleration<sup>[49]</sup> or buffer-gas cooling<sup>[50-52]</sup>, but the densities and temperatures

achieved so far are still orders of magnitude away from quantum degenerate regime. A very promising approach to degeneracy, actively explored by several groups<sup>[53,54]</sup>, is to start from already ultra cold atomic mixtures and then use a Feshbach resonance to create heteronuclear molecules<sup>[55]</sup>. Crated in a highly excited vibrational state, they must then be brought to the rotational ground state, for instance by photo association using STIRAP processes, as demonstrated lately<sup>[56]</sup>. Recent experiments at JILA on KRb molecules are just slightly below the phase-space density required for quantum degeneracy<sup>[57]</sup>.

### II.1.a Optical lattices and the DDI

The special features of the DDI lead to novel physics in lattice gases, and in particular to significant new terms in the Bose-Hubbard Hamiltonian. The on-site parameter  $U$  is given by two contributions  $U_s$  and  $U_{\text{DDI}}$ . The first one arises from the  $s$ -wave scattering shown already in Eq. (1.5), and the second one is due to the on-site DDI

$$(II.2) \quad U_{\text{DDI}} = \frac{1}{2\pi^3} \int \tilde{V}_{\text{DDI}}(\vec{q}) \tilde{n}^2(\vec{q}) d^3q,$$

where

$$(II.3) \quad \tilde{V}_{\text{DDI}}(\vec{q}) = \frac{C_{\text{dd}}}{3} \left( \frac{2q_z^2 - q_x^2 - q_y^2}{q^2} \right)$$

and  $\tilde{n}(\vec{q})$  are the Fourier transforms of the dipole potential and density, respectively<sup>[58]</sup>. Interestingly, the long-range character of the DDI leads to the appearance of significant inter-site interactions, a qualitatively novel fact compared to non-polar gases. The inter-site interaction between particles at two sites  $\vec{i}$  and  $\vec{i} + \vec{l}$ , is characterized by the coupling constant

$$(II.4) \quad U'_l = \int d^3r \int d^3r' \omega_{\vec{i}}(\vec{r}) \omega_{\vec{i}+\vec{l}}(\vec{r}') V_{\text{DD}}(\vec{r} - \vec{r}').$$

For a deep enough square optical lattice, this expression reduces to

$$(II.5) \quad U'_l \approx V_{\text{DD}}(\vec{l}\lambda),$$

where  $\lambda$  is the lattice constant. Then, a lattice of polarized bosons, as sketched in Fig II.2, is described by an *extended Bose-Hubbard* Hamiltonian of the form

$$(II.6) \quad \hat{H} = -t \sum_{\langle \vec{i}\vec{j} \rangle_1} \hat{b}_i^\dagger \hat{b}_j + \sum_i \left[ \frac{U}{2} \hat{n}_i (n_i - 1) - \mu \hat{n}_i \right] + \sum_{\vec{l}} \sum_{\langle \vec{i}\vec{j} \rangle_{\vec{l}}} \frac{U'_l}{2} \hat{n}_i \hat{n}_j,$$

where  $\langle \vec{i}\vec{j} \rangle_{\vec{l}}$  are all the possible sites  $\vec{i}$  and  $\vec{j}$  with a distance  $\vec{l}$  between them.

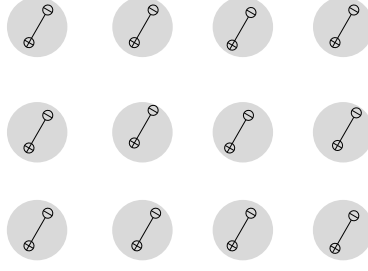


Figure II.2: Scheme of a gas of polarized dipoles in a single 2D layer.

The extended Bose-Hubbard Hamiltonian has been extensively studied<sup>[24]</sup>. Novel phases result from inter-site interactions as the charge-density wave (checkerboard) characterized by an insulating phase with modulated density, and the supersolid phase that presents the coexistence of superfluidity and a periodic spatial modulation of the density which is different from the lattice period<sup>[59–61]</sup>. 1D lattice systems of spinless bosons interacting with long-range interactions possess a further insulating gapped phase, namely a Haldane insulator<sup>[62]</sup>. This insulator resembles the famous Haldane gapped phase in quantum spin-1 chains<sup>[63]</sup>. Unlike in the checkerboard case, the Haldane insulator does not break the translational symmetry of the lattice. However, it is characterized by an underlying hidden order which consists of a nontrivial ordering of the fluctuations which appear in alternating order separated by strings of equally populated sites of arbitrary length<sup>[64]</sup>.

## II.2 The Hamiltonian of two interacting chains

In the following, we consider a ladder-like lattice made of two neighbor one-dimensional optical lattices loaded with dipolar bosons. The ladder legs are disconnected in the sense that no particle can tunnel from one wire to the other. This scheme can be achieved by micro-magnetic confinement<sup>[65]</sup> or using sufficiently strong two-dimensional optical lattices<sup>[66]</sup>. In the latter case, the required two-site configuration may be generated by super-lattice techniques or by selectively emptying one-dimensional sites neighboring the desired pair. The configuration is presented in Fig. II.3.

We will focus mostly on interlayer effects, and hence we consider a configuration for which only the (attractive) dipole-dipole interaction between particles at the same rung and different wire plays a significant role. This is the case when the dipoles are oriented forming an angle  $\theta_m$  with the axis of the wires such that  $\cos^2 \theta_m = 1/3$  (the magic angle, discussed in section II.1). Under that condition, the dipole-dipole interaction between neighbor particles at the same wire vanishes, whereas for particles in the same rung and different wires is attractive. There is, in principle, an additional nonzero diagonal

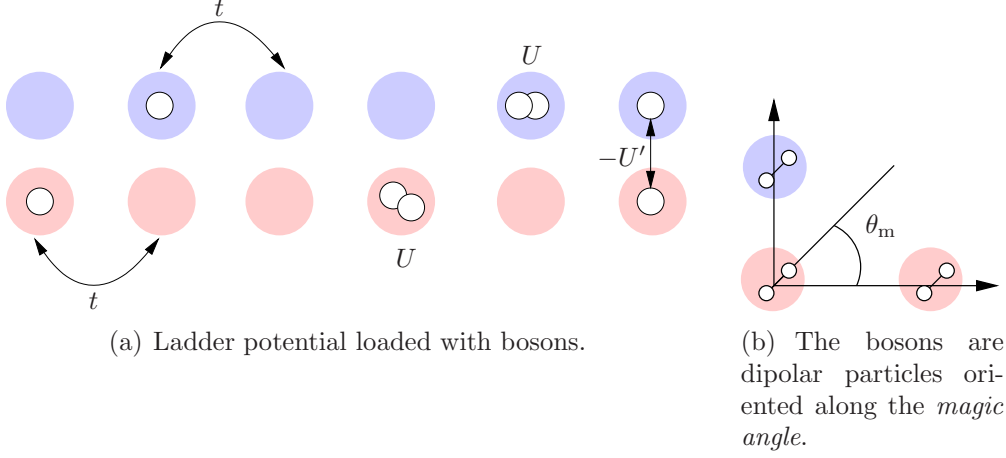


Figure II.3: Scheme of the system under consideration in this chapter. A ladder-like potential loaded with boson dipolar particles. (a) Each wire can be considered independently with the Bose-Hubbard Hamiltonian. (b) When the particles are all oriented along the magic angle only intra-rung interactions are relevant creating an attractive potential.

dipole-dipole interaction between particles in different wires and neighboring rungs. These terms can be negligible by considering the spacing between rungs larger than the separation between the two wires by a factor  $\gamma$ . In that case the spurious diagonal interaction has a factor  $(1 + 2\sqrt{2}\gamma)/(1 + \gamma^2)^{5/2} (\approx 0.03$  for  $\gamma = 3$ ) smaller than that between sites in the same rung. Of course, for other dipole and lattice configurations, the dipole-dipole interaction between sites belonging to the same wire cannot be neglected, and interesting physics can be expected<sup>[67]</sup>.

All these considerations can be summed up into the following Hamiltonian,

$$(II.7) \quad \hat{H} = \sum_{\alpha=1,2} \hat{H}_B^{(\alpha)} - U' \sum_i \hat{n}_i^{(1)} \hat{n}_i^{(2)},$$

with  $U, U' > 0$  and

$$(II.8) \quad \begin{aligned} \hat{H}_B^{(\alpha)} = & -t \sum_{\langle i,j \rangle} \left( \hat{b}_i^{(\alpha)\dagger} \hat{b}_j^{(\alpha)} + \text{h.c.} \right) \\ & + \frac{U}{2} \sum_i \hat{n}_i^{(\alpha)} (\hat{n}_i^{(\alpha)} - 1) - \mu \sum_i \hat{n}_i^{(\alpha)} \end{aligned}$$

where  $\hat{b}_i^{(\alpha)}$ ,  $\hat{b}_i^{(\alpha)\dagger}$ , and  $\hat{n}_i^{(\alpha)}$  are, respectively, the annihilation, creation, and number operators at the site  $i$  on the wire  $\alpha$ . The hopping probability between neighboring sites  $i$  and  $j$  in each wire is described by  $t$ ,  $U$  represents the on-site interactions which are a combination of short-range and dipolar contributions,

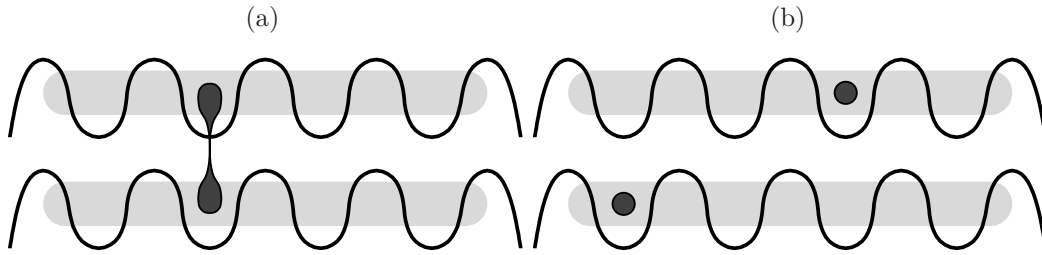


Figure II.4: Schematic diagram of the superfluid phases present in the ground state of the Hamiltonian (II.7). (a) Pair superfluid where the super fluid is made of particles and (b) Two superfluid where each wire has an independent superfluid.

and we consider the same chemical potential  $\mu$  for both wires. Atoms in sites at the same rung interact attractively by the dipole-dipole interaction, which is characterized by a coupling  $-U'$ . The image of the system can be further simplified just by looking at the system as a one-dimensional Bose-Bose mixture with an on-site intra-species repulsive interaction  $U$  and an attractive inter-species interaction  $-U'$ . Under this picture, is even more clear the appearance of the *pair superfluid* (PSF) phase that plays a significant role in the physics of the system<sup>[68]</sup>.

The PSF phase refers to the creation of correlated rung pairs of particles in the ladder when the inter-species interaction is large enough. However, for a larger hopping parameter and a weak inter-species interaction the creation of pairs may be uncorrelated giving place to a new phase where two independent SF are present, one in each specie. We denominate this last phase as the two superfluid (2SF). These two phases are depicted in Fig. II.4.

In the following we will proceed as in the previous chapter. First, we make use of the SCE to obtain the phase boundaries for all the possible filling factors and dimensions. Latter we compare those analytical results with the numerical ones from MPS calculations.

### II.3 Strong coupling analysis

Following the procedure developed in section I.3, we use the SCE in the hopping  $\tilde{t} = t/U \ll U'/U = \tilde{U}'$  in order to calculate the Mott-lobe boundaries. The first step is to get the Mott energy from the perturbation of a Mott state with  $\bar{n}$  particles per site. Afterwards, we put a correlated (same rung) pair of particles on top of the  $MI\bar{n}$  to recreate the PSF and then we apply the perturbation theory again. By equating the two corrected energies we can calculate the interface as the function  $\tilde{\mu}(\tilde{t})$ . We proceed in an analog way for the transition to the 2SF phase but instead of correlated pairs we use totally uncorrelated pairs.



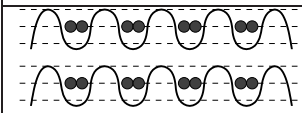
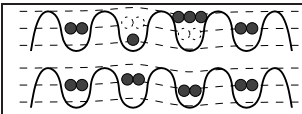
It is important to note that no finite perturbation theory will reproduce faithfully the tip of the Mott insulator as in the case of the BHH. With this method, the correlation functions cannot be calculated either. However, we can do the calculation for all the Mott phases and for high dimensions by considering different values for the number of neighbor sites  $z$ .

### II.3.a The MI $\bar{n}$

The unperturbed Mott insulator is described by the Fock state

$$(II.9) \quad |\phi_{\text{MI}}(\bar{n})\rangle^{(0)} = \prod_{i,\alpha} \frac{1}{\sqrt{\bar{n}!}} \left( b_i^{(\alpha)\dagger} \right)^{\bar{n}} |\emptyset\rangle,$$

where  $|\emptyset\rangle$  is the vacuum,  $i = 1, \dots, L$  and  $\alpha = 1, 2$ . The first-order term does not appear since just like in the case of a single wire, all the odd terms vanish. On the other hand, for the second order we have to consider the following eigenstates and energies using the same notation as in chapter I

State	$\tilde{E}_\nu$	$g_\nu$	$-\tilde{E}_\nu^{(2)}/2z\tilde{t}^2$
	$\tilde{E}_{\text{MI}}^{(0)} = \bar{n}L \left[ (\bar{n} - 1) - \tilde{U}'\bar{n} - 2\tilde{\mu} \right]$		
	$\tilde{E}_{\text{MI}}^{(0)} + 1$	$2zL$	$L\bar{n}(\bar{n} + 1)$

And from it we have the corrected energy up to 2nd order as

$$(II.10) \quad \tilde{E}_{\text{MI}}(\bar{n}) = \bar{n}L \left[ (\bar{n} - 1) - \tilde{U}'\bar{n} - 2\tilde{\mu} - 2z\tilde{t}^2(\bar{n} + 1) \right].$$

As we already discussed, there are two possible phase transitions when starting from the Mott: either to the PSF or to the 2SF. For a small enough hopping we expect that the dipole-dipole interaction term dominates and therefore the transition goes towards the PSF phase. For larger values of  $\tilde{t}$ , the particles are more free to move and the rung composites are not longer stable. In this case, we expect that the transition takes place between the MI and the 2SF. Here, we will calculate the PSF-boundaries and the 2SF-boundaries for each filling factor. The intersection between the two regions will define the actual Mott lobe. This construction is shown in Fig. II.5.

### II.3.b Pair superfluid

*Upper boundary.* Again, we apply the same procedure to the “defect” state

$$(II.11) \quad |\phi_{\text{P}}(\bar{n})\rangle^{(0)} = \frac{1}{\sqrt{L}} \sum_i \frac{\hat{b}_i^{(2)\dagger} \hat{b}_i^{(1)\dagger}}{\bar{n} + 1} |\phi_{\text{MI}}(\bar{n})\rangle^{(0)},$$

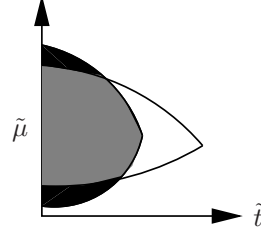


Figure II.5: Definition of the Mott lobe from the intersection (gray) of the PSF lobe calculation (white) and the one from 2SF (black).

that creates a correlated pair of particles. In this case, only second order terms contribute. This comes from the fact that in order to shift the composite, made of the two extra correlated particles, two hopping terms should act. Therefore, first order sends us away of the considered manifold. However, the number of virtual states is higher than in the case of just one chain.

State	$\tilde{E}_\nu$	$g_\nu$	$-\tilde{E}_\nu^{(2)}/2z\tilde{t}^2$
	$\tilde{\Delta}_p^{(0)} = 2\bar{n} - 2\tilde{\mu} - \tilde{U}'(2\bar{n} + 1)$		
	$\tilde{E}_p^{(0)} + 1$	$2z(L - 2)$	$(L - 2)\bar{n}(\bar{n} + 1)$
	$\tilde{E}_p^{(0)} + \tilde{U}'$	$4z$	$\frac{2(\bar{n}+1)^2}{\tilde{U}'}$
	$\tilde{E}_p^{(0)} + 2 - \tilde{U}'$	$2z$	$\frac{\bar{n}(\bar{n}+2)}{2-\tilde{U}'}$

In the table we considered that  $\tilde{\Delta}_p^{(0)} = \tilde{E}_p^{(0)}(\bar{n}) - \tilde{E}_{\text{MI}}^{(0)}(\bar{n})$ . As a result we have the following expression for the energy

$$(II.12) \quad \begin{aligned} \tilde{E}_p(\bar{n}) = & \tilde{E}_{\text{MI}}(\bar{n}) + 2\bar{n} - \tilde{U}'(2\bar{n} + 1) - 2\tilde{\mu} \\ & - 2z\tilde{t}^2 \left[ \frac{2(\bar{n} + 1)^2}{\tilde{U}'} + \frac{\bar{n}(\bar{n} + 2)}{2 - \tilde{U}'} - 2\bar{n}(\bar{n} + 1) \right]. \end{aligned}$$

After equating the Mott and the PSF energies, the upper lobe boundary becomes

$$(II.13) \quad \begin{aligned} \tilde{\mu}_+^{\text{PSF}}(\bar{n}) = & \bar{n} - \frac{\tilde{U}'}{2}(2\bar{n} + 1) \\ & - z\tilde{t}^2 \left[ \frac{2(\bar{n} + 1)^2}{\tilde{U}'} + \frac{\bar{n}(\bar{n} + 2)}{2 - \tilde{U}'} - 2\bar{n}(\bar{n} + 1) \right]. \end{aligned}$$

*Lower boundary.* Once more, we will apply the procedure to the state with a particular “defect”. This time it consists of correlated pair of holes created on top of the Mott state. Therefore, the unperturbed state can be written as

$$(II.14) \quad |\phi_h(\bar{n})\rangle^{(0)} = \frac{1}{\sqrt{L}} \sum_i \frac{\hat{b}_i^{(2)} \hat{b}_i^{(1)}}{\bar{n}} |\phi_{\text{MI}}(\bar{n})\rangle^{(0)}.$$

By the same reasoning as before, no odd terms contribute to the energy. Hence, the first non-zero correction is the second order term that can be build based on the following virtual states and their corresponding contribution:

State	$\tilde{E}_\nu$	$g_\nu$	$-\tilde{E}_\nu^{(2)}/2z\tilde{t}^2$
	$\tilde{\Delta}_h^{(0)} = -2(\bar{n} - 1)$ $-\tilde{U}'(1 - 2\bar{n}) + 2\tilde{\mu}$		
	$\tilde{E}_h^{(0)} + 1$	$2z(L - 2)$	$(L - 2)\bar{n}(\bar{n} + 1)$
	$\tilde{E}_h^{(0)} + \tilde{U}'$	$4z$	$\frac{4\bar{n}^2}{\tilde{U}'}$
	$\tilde{E}_h^{(0)} + 2 - \tilde{U}'$	$2z$	$\frac{(\bar{n}^2 - 1)}{2 - \tilde{U}'}$

After we equate the resulting energy with the one of the Mott given by (II.10) and solve for the chemical potential, we get for the lower boundary the function

$$(II.15) \quad \tilde{\mu}_-^{\text{PSF}}(\bar{n}) = \bar{n} - 1 + \frac{\tilde{U}'}{2}(1 - 2\bar{n}) + z\tilde{t}^2 \left[ \frac{2\bar{n}^2}{\tilde{U}'} + \frac{(\bar{n}^2 - 1)}{2 - \tilde{U}'} - 2\bar{n}(\bar{n} + 1) \right].$$

This solution is particularly interesting since for  $\bar{n} = 1$  and  $U' > U/2$  the slope of the lowest boundary changes from positive to negative. This will affect the shape of the Mott shells when a trap is added. For  $U' > U(29 - \sqrt{73})/24 \approx 0.8253U$  the effect is present in the second lobe although for larger lobes no inversion occurs.

It is important to note that this re-entrant scenario is independent on the dimension of the system, because the coordination number  $z$  factorizes out. In Fig. II.6 one can see the distortion of the Mott lobes for different values of the attractive interaction  $U'$ . Furthermore, another interesting result is that for low enough hopping, the Mott gap boundaries are quadratic and not linear as in the case of no inter-wire interaction. This is a direct result of the vanishing of the first order terms in the perturbation theory.

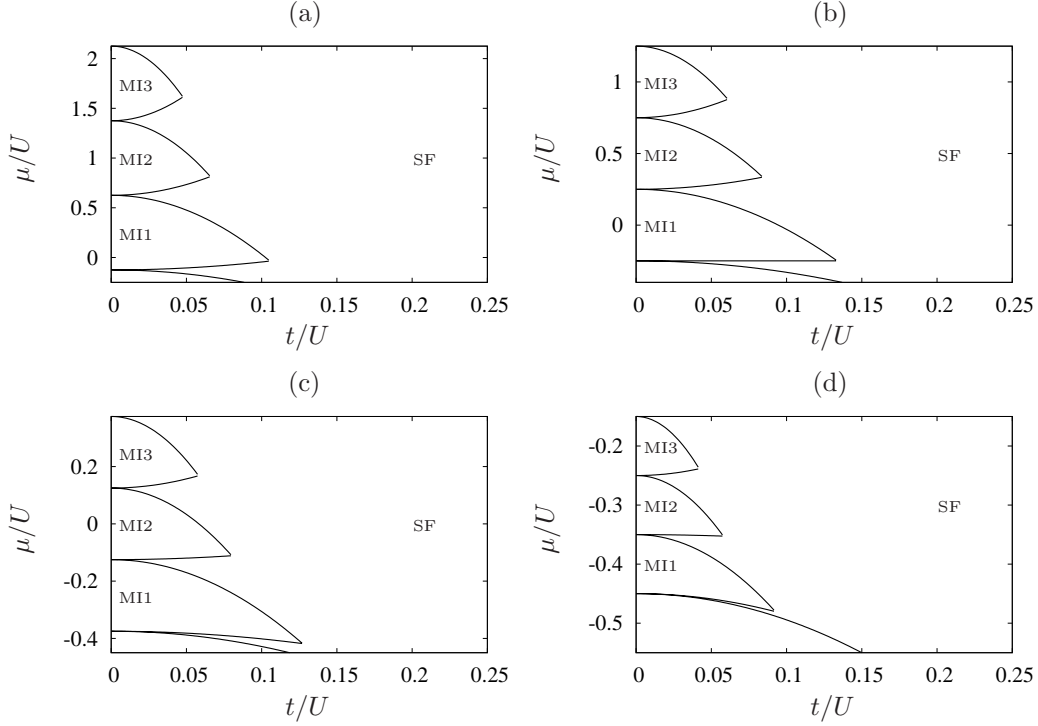


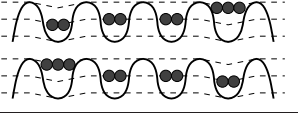
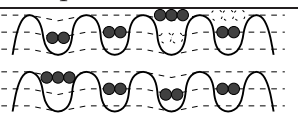
Figure II.6: MI-PSF transition from SCE calculation for  $z = 2$  and (a)  $U' = U/4$ , (b)  $U' = U/2$  where the MI1 lowest boundary is independent of the hopping, (c)  $U' = 3U/4$  where the MI1 lowest boundary has an opposite slope and (d)  $U' = 9U/10$  where the MI2 lobe has a slightly inverted lower boundary.

### II.3.c Two superfluid

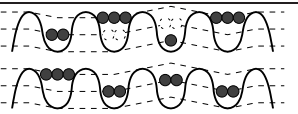


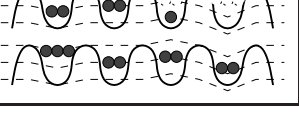
Now we will focus on the calculation of the interface between the Mott insulator and the phase where the creation of particles is not correlated, the two superfluid phase. In this case, we have a contribution from first order perturbation theory because the hopping of one particle (hole) is, of course, not correlated to the position of the other extra particle (hole) on the other chain.

*Upper boundary.* In an analogous way as above, we will add a particle in each wire on top of the Mott phase. The main difference is that the particles do not share the same rung and thus, they do not see each other at all. As before, the process is summarized with the help of similar schemes.

The first order contribution to the energy is provided by the eigenstates:

Initial state	$\tilde{\Delta}_p^{(0)}$
	$2 \left[ \bar{n}(1 - \tilde{U}') - \tilde{\mu} \right]$
Equivalent state	$-\tilde{E}_p^{(1)}/2z\tilde{t}$
	$\bar{n} + 1$

For the second order, we have to consider the following virtual states:

Virtual states	$\tilde{E}_\nu$	$g_\nu$	$-\tilde{E}_\nu^{(2)}/2z\tilde{t}^2$
	$\tilde{E}_p^{(0)} + 1$	$2z(L - 3)$	$(L - 3)\bar{n}(\bar{n} + 1)$
	$\tilde{E}_p^{(0)} + 1 - \tilde{U}'$	$2z$	$\frac{\bar{n}(\bar{n}+1)}{1-\tilde{U}'}$
	$\tilde{E}_p^{(0)} + 1 + \tilde{U}'$	$2z$	$\frac{\bar{n}(\bar{n}+1)}{1+\tilde{U}'}$
	$\tilde{E}_p^{(0)} + 2$	$2z$	$\frac{\bar{n}(\bar{n}+2)}{2}$

After summing all the terms up and equating with the Mott energy for the chemical potential, the upper boundary of the Mott insulator to two superfluid transition is given by

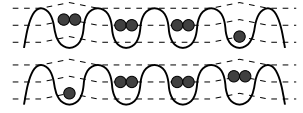
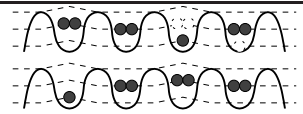
$$(II.16) \quad \tilde{\mu}_+^{2SF}(\bar{n}) = \bar{n}(1 - \tilde{U}') - z\tilde{t}(1 + \bar{n}) + z\bar{n}\tilde{t}^2 \frac{(4 + 5\bar{n})\tilde{U}'^2 - \bar{n}}{2(\tilde{U}'^2 - 1)}.$$

Although this expression seems to be rather complicated, it has a very interesting limit for  $\tilde{U}' \rightarrow 0$ ,

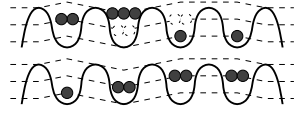
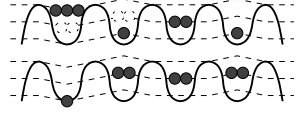


$$(II.17) \quad \lim_{\tilde{U}' \rightarrow 0} \tilde{\mu}_+^{2SF}(\bar{n}) = \bar{n} - z\tilde{t}(1 + \bar{n}) + \frac{1}{2}z\bar{n}^2\tilde{t}^2.$$

Note that this limit coincides with Eq. (I.20) that describes the upper lobe boundary for one chain. This lead us to the intuitive conclusion that when no interaction is present, the superfluid state of the two chains is, of course, completely independent. From this point of view, the idea behind the 2SF becomes more clear.

*Lower boundary.* In an identical procedure, we have the following states for the first order term:

Initial state	$\tilde{\Delta}_p^{(0)}$
	$2 \left[ 1 - \bar{n}(1 - \tilde{U}') + \tilde{\mu} \right]$
Equivalent state	$-\tilde{E}_p^{(1)}/2z\tilde{t}$
	$\bar{n}$

And regarding the virtual states, we consider:

Virtual states	$\tilde{E}_\nu$	$g_\nu$	$-\tilde{E}_\nu^{(2)}/2z\tilde{t}^2$
	$\tilde{E}_p^{(0)} + 1$	$2z(L - 3)$	$(L - 3)\bar{n}(\bar{n} + 1)$
	$\tilde{E}_p^{(0)} + 1 + \tilde{U}'$	$2z$	$\frac{\bar{n}(\bar{n}+1)}{1+\tilde{U}'}$
	$\tilde{E}_p^{(0)} + 1 - \tilde{U}'$	$2z$	$\frac{\bar{n}(\bar{n}+1)}{1-\tilde{U}'}$
	$\tilde{E}_p^{(0)} + 2$	$2z$	$\frac{\bar{n}^2 - 1}{2}$

Thus, finally the lower boundary of the MI to 2SF transition is described by the formula

$$(II.18) \quad \tilde{\mu}_-^{2SF}(\bar{n}) = \bar{n}(1 - \tilde{U}') - 1 + \bar{n}z\tilde{t} - z\tilde{t}^2(1 + \bar{n}) \frac{\bar{n}(5\tilde{U}'^2 - 1) - 1 + \tilde{U}'^2}{2(\tilde{U}'^2 - 1)}.$$

Applying the procedure described in the diagram II.5, one can see that the MI lobes have a notorious change as shown in Fig. II.7 for 2D and 3D systems. From Fig. is clear that for  $\tilde{U}' > 1/2$  the re-entrant scenario is still present since the transition from Mott to pair superfluid holds for small values of  $\tilde{t}$  as discussed above. One important characteristic of the presented lobes is that the tip shape changes and in general the lobe gets shorter. However, we recall that the SCE is far from exact at this region.

## II.4 Correlation functions

In order to distinguish between the ground-state phases present of the Hamiltonian (II.7), we employ the convenient correlation function of Eq. (I.22). An

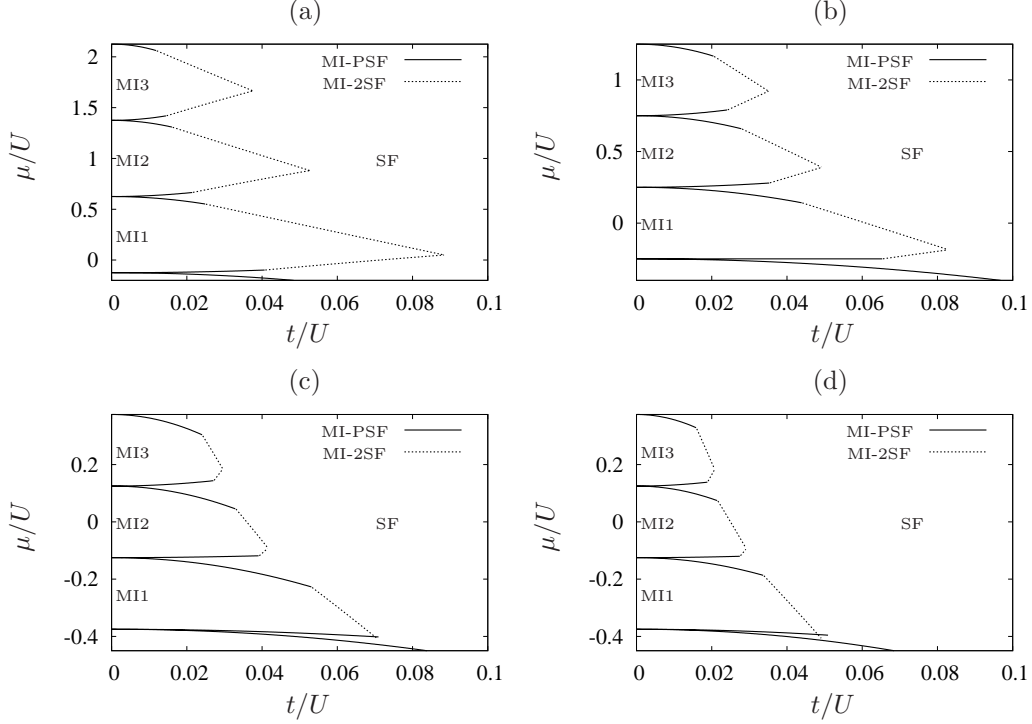


Figure II.7: Phase space for a bi-layer system with inter-layer attractive interaction at the same site from SCE calculation (a)  $U' = U/4$ , (b)  $U' = U/2$  and (c)  $U' = 3U/4$ . (d) Three dimensional system, with  $U' = 3U/4$ . The re-entrant scenario is still present.

analogous function can be defined for each wire of the ladder as

$$(II.19) \quad \mathcal{G}_1^{(\alpha)}(\Delta) = \langle \hat{b}_0^{(\alpha)\dagger} \hat{b}_\Delta^{(\alpha)} \rangle.$$

In the case of  $U' = 0$ , when the two wires are completely independent, it shows an exponential decay for the MI and a polynomial decay for the superfluid when calculated on either wire. This distinction should hold in the presence of DDI. Since, no correlation between the wires is considered in  $\mathcal{G}_1^{(\alpha)}(\Delta)$ , it clearly identifies the 2SF when a polynomial decay is presented.

In order to characterize the pair superfluid we have to study the correlation function decay of the composites made of same-rung correlated particles (holes). We define the composite annihilator operator at the rung  $i$  as

$$(II.20) \quad \hat{B}_i \equiv \hat{b}_i^{(1)} \hat{b}_i^{(2)},$$

and the extended composite correlation function, or equivalently the two particle correlation function, as

$$(II.21) \quad \mathcal{G}_2(\Delta) = \langle \hat{B}_0^\dagger \hat{B}_\Delta \rangle \equiv \langle \hat{b}_0^{(2)\dagger} \hat{b}_0^{(1)\dagger} \hat{b}_\Delta^{(1)} \hat{b}_\Delta^{(2)} \rangle.$$

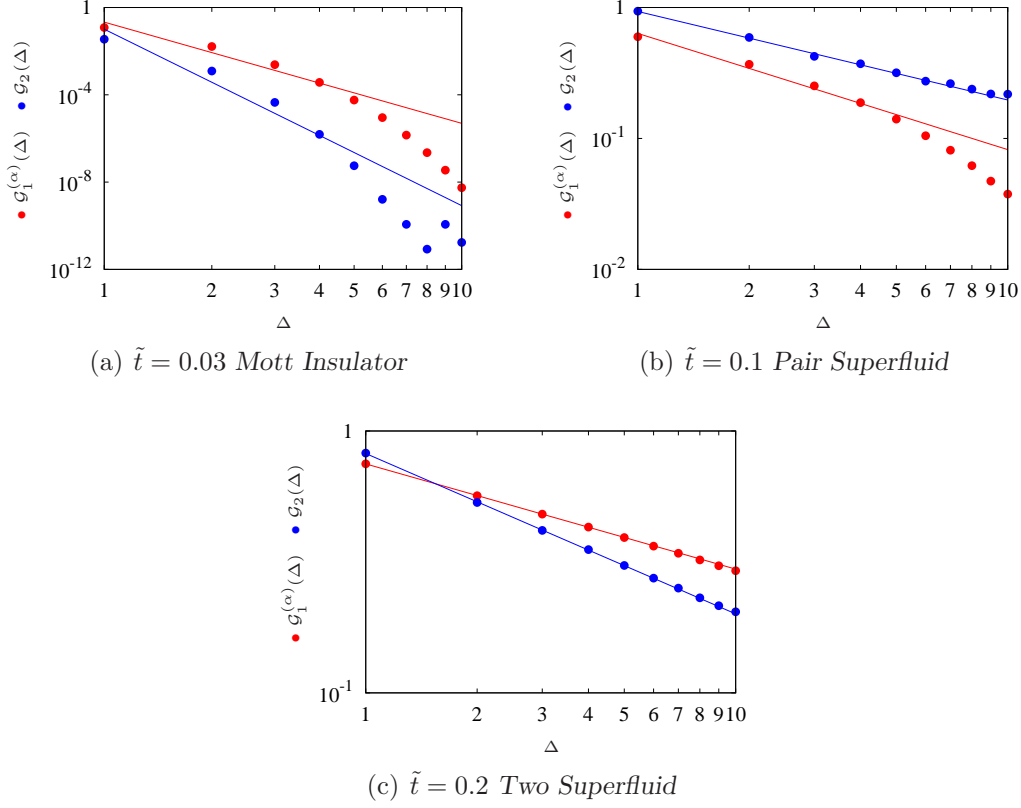


Figure 11.8: The functions  $\mathcal{G}_1^{(\alpha)}(\Delta)$  and  $\mathcal{G}_2(\Delta)$  for a ladder like potential with  $\mu = -0.15U$ ,  $U' = 3U/4$  and several values of  $\tilde{t}$ . The three phases can be directly characterized by the decay of the correlation functions by fitting to a power law decay presented here as a line.

The  $\mathcal{G}_2(\Delta)$  correlation function provides information about the existence of flow of pair-superfluidity.

Our MPS results for  $\mathcal{G}_1^{(\alpha)}(\Delta)$  and  $\mathcal{G}_2(\Delta)$  are displayed in Fig. 11.8 in a log – log scale where the distinction between the phases is more evident. In the following table, a guide of how to read-off the ground state phases from the decay of the different correlation functions is presented:

State	$\mathcal{G}_1^{(\alpha)}(\Delta)$	$\mathcal{G}_2(\Delta)$
<b>Mott</b>	Exponential	Exponential
<b>PSF</b>	Exponential	Polynomial
<b>2SF</b>	Polynomial	Polynomial

*PSF to 2SF transition.* One of the main advantages of the MPS method is that it is also possible to calculate the interface between the two different superfluid phases. As an example, we explored in detail the lowest Mott insulator lobe. The resulting phase space is depicted in Fig. 11.9 where it is also compared with the SCE results.



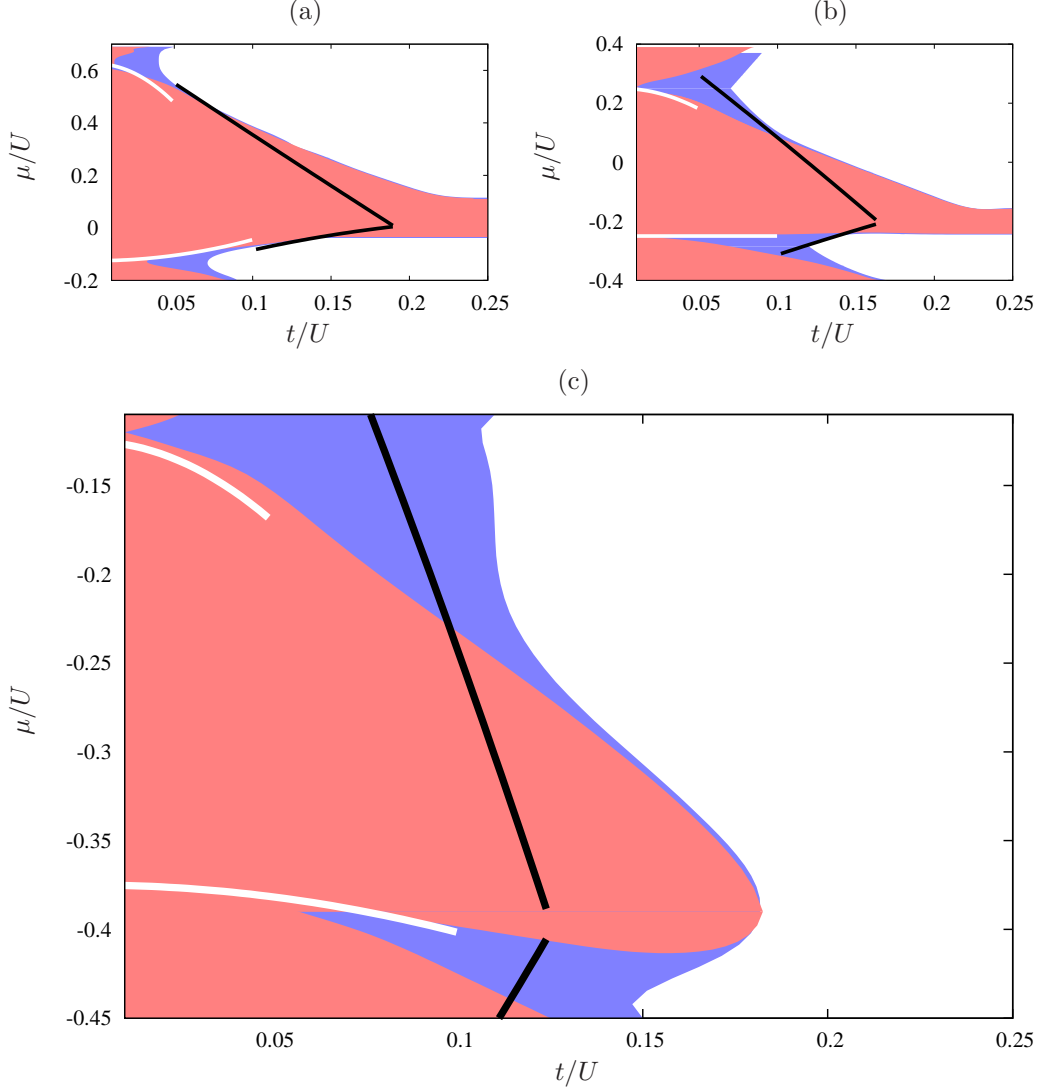


Figure II.9: First Mott-insulator lobe for a ladder potential with attractively interacting rungs for  $L = 18$ ,  $\chi = 20$  and (a)  $U' = U/4$ , (b)  $U' = U/2$  and (c)  $U' = 3U/4$ . The different phases are depicted with white (2SF), blue (PSF) and red (MI). The lines are the theoretical results from SCE where white is the transition MI-PSF and black MI-2SF.

From the figure, it is very clear that the SCE description is excellent for the Mott to PSF phase transition that takes place at very small hopping values and the agreement with the MPS results is notable. In particular, the shape of the lower boundary and its change in slope is very well reproduced matching to the MPS calculations. However, for larger values of  $t$ , there is a clear discrepancy between both results. In order to explain this, several sources of error can be recalled such as the finite size of the MPS calculation and

the open boundary condition that were considered in contrast to the periodic boundary conditions taken for the SCE. On the other hand, from the results given in the previous chapter, we know that at the tip of the Mott-insulator the SCE fails. One can also see that the discrepancy is even higher for larger values of  $|U'|$  although the validity range for the same theory with the PSF increases. The connection between the two boundaries in SCE also fails since we considered the two extremes: first, totally uncorrelated and second, totally correlated pairs. Indeed, there is a parameter regime for which one can find a slight correlation between extra particles at neighboring rungs.

Although the details of the MPS algorithms are presented in detail in chapter VII, we would like to point out here an important issue concerning the numerical MPS calculations, related to the complexity of the correlation functions involved. In general, each one of them has a total number of operations of the order of  $\mathcal{O}(\chi^4 d^2 \Delta) \sim 10^7$ , where  $d - 1$  is the maximal number of particles allowed per site and  $\chi$  is the matrix dimension. This makes the whole calculation of the phase space a costly procedure since each scanning requires about  $10^4$  calculations for each value of  $U'$ . Moreover, those calculations are done after retrieving the ground state from the variational method at each point of the phase space. In conclusion, the MPS results are very reliable at a high computational cost that excludes the possibility of exploring higher values of the filling factor. However, some additional interaction may be added to the system such as an intra-wire nearest neighbor interaction.

## II.5 External harmonic trap

In section I.5 we commented that the presence of a harmonic trap leads to a wedding-cake structure of the phases if the local chemical potential at the center lies on a Mott phase and the extremes on a superfluid. Since the lower boundary of the Mott lobes usually has a positive slope as a function of the hopping, by increasing the hopping the Mott shell shrinks, reflecting the intuitive image that the larger the mobility of the particles, the less insulating the material becomes. However, in the case of the ladder-like potential with rung attractive interaction, the lower boundary of the first Mott may have a negative slope in the hopping and thus, we expect that when a harmonic trap is over imposed we may get the counter-intuitive effect that the Mott shells would expand as the mobility increases.

Figure II.10 shows the MPS calculation of the system when an external trapping potential is added. The chosen values for the trap are such that the center of the ladder has a chemical potential laying in the Mott region and along the wires the system explore lower values of  $\tilde{\mu}$  in a way that the system reaches a filling of zero at the extremes. In this way we impose the system to form a Mott-insulating core surrounded by a superfluid shell<sup>[69]</sup>.

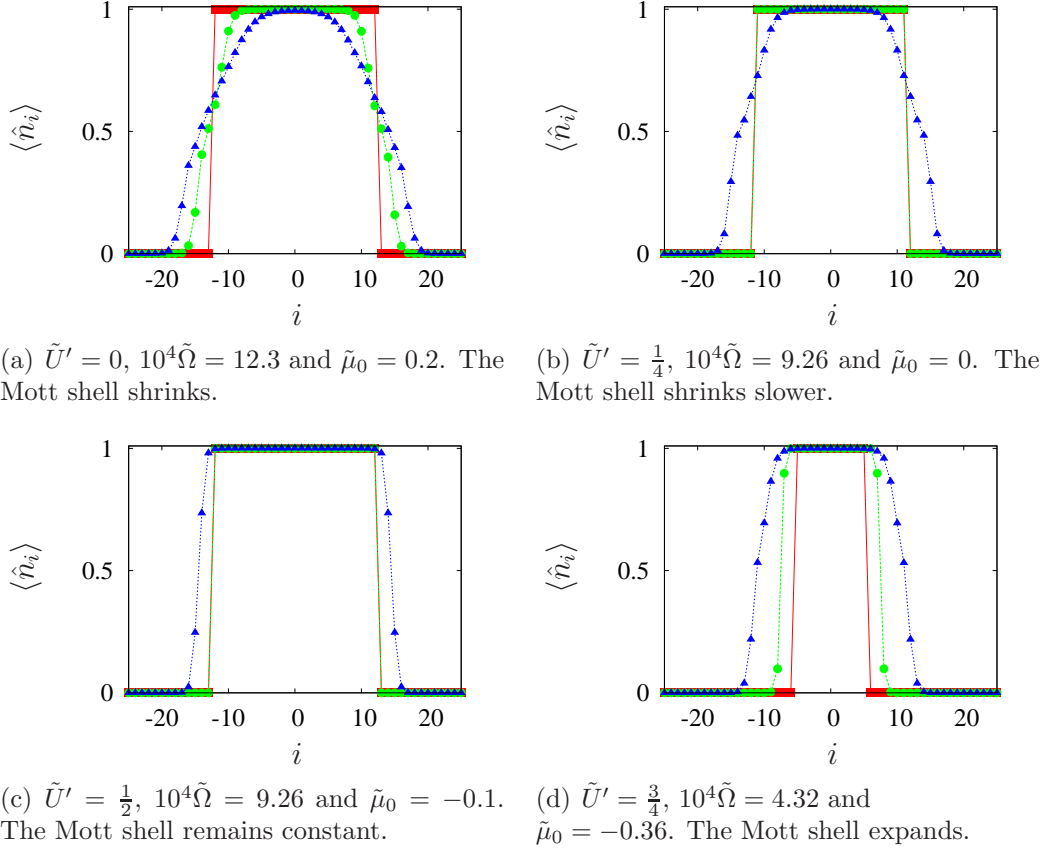


Figure II.10: Mott shells of a ladder-like potential with rung attractive interactions and a trap  $\tilde{\epsilon}_i = \tilde{\mu}_0 - \tilde{\Omega}i^2$  for  $\tilde{t} = 0$  (■),  $\tilde{t} = 0.05$  (●) and  $\tilde{t} = 0.1$  (▲).

The results coincide with our expectations. For  $\tilde{U}' < 1/2$  the Mott shell shrinks at  $\tilde{t}$  increases (panels (a) and (b)). In the critical case of  $\tilde{U}' = 1/2$  the shell is independent of the hopping and thus it remains steady (panel (c)), and finally, for  $\tilde{U}' > 1/2$  the Mott shell gets wider (d). This striking result challenges the intuitive expectations coming from the usual BHH.



## PART B

# DYNAMICS OF SPINOR LATTICE GASES



## Spin 3/2 fermions in 1D optical lattices

When the complexity of a system is increased, novel physics may appear in both dynamical processes and ground state properties. In the previous chapter, we analyze the influence of the dipole-dipole interaction on a system in a ladder-like potential. Another interesting novel feature of cold atoms is provided by their internal structure. Spinor gases of atoms with several internal degrees of freedom, are thus a natural object of research on this field. Thus, in this chapter, we briefly discuss the physics of spinor gases, specially the case of spin-3/2 fermions in one dimensional optical lattices.

In previous chapters we conclude that ultra-cold gases in optical lattices offer an extraordinary controllable environment for the analysis of many-body phenomena. In particular, one of the breaking-ground experiments show the realization of the Mott-Insulator to super-fluid phase transition with Bose gases<sup>[6]</sup>, and even, more recently, the manipulation of two component Fermi systems in order to observe the Mott insulator to metal transition<sup>[70,71]</sup>.

Multicomponent quantum systems are a rich source of physics and thus, in the following chapters, we focus on spinor gases. More specifically, in this one we introduce the topic of spinor gases in optical lattices and develop the effective Hamiltonian of hard-core spin-3/2 fermions in the Mott regime in the presence of a quadratic Zeeman coupling. This Hamiltonian presents a wealth of physics. The next chapter is devoted to the dynamics of repulsively-bound states that can be builded on top of a polarized eigenstate of this system. Chapter V deals with the ground state properties of the effective spin-3/2 Hamiltonian.

### III.1 Spinor gases

Spinor gases, formed by atoms with several available Zeeman sub-states, present an exceedingly rich physics caused by the interplay between internal and external degrees of freedom<sup>[72]</sup>. For instance, inter-atomic interactions

lead to spin-changing processes in which population is transferred coherently between different Zeeman sub-levels. This fascinating effect has attracted a large interest, mostly in the realm of spinor BEC<sup>[73,74]</sup>. The breakthrough of spinor condensates came with the development of dipole traps, since it is possible to confine all the components of a spinor BEC. The spin-1 Na condensate was the first achievement in this respect<sup>[75]</sup>, followed by <sup>87</sup>Rb condensates of spin-1 and spin-2 particles<sup>[76,77]</sup>. Furthermore, spin-3 BEC may be reached with Cr<sup>[78]</sup>. From the theoretical side, spinor condensates have been focus of deep research including ground state properties<sup>[79,80]</sup>, coherent spin mixing<sup>[81–86]</sup>, spinor vortices<sup>[87,88]</sup>, spin textures and domains<sup>[89,90]</sup> and, spin squeezing and entanglement<sup>[91,92]</sup>.

On the other hand, spinor fermions have recently become the focus of a rapidly growing interest, motivated by experiments on BEC-BCS crossover in two-component fermions<sup>[7]</sup> and the availability of multicomponent fermions, including three-component Li gases<sup>[93]</sup>, spin-3/2 fermions such as <sup>135</sup>Ba and <sup>137</sup>Ba<sup>[94]</sup>, and Fermi-degenerate Yb<sup>[95]</sup>. Multicomponent fermions present a wealth of novel phases. Pseudo-spin-1 fermions allow for color superfluidity and trions<sup>[96–100]</sup>, whereas attractive spin-3/2 gases allow for the possibility of quartet formation<sup>[101–105]</sup>.

Furthermore, spinor lattice gases offer novel physics most relevantly on the field of quantum magnetism, including anti-ferromagnetic order in spin-1/2 fermions<sup>[106]</sup>, and even more intriguing phases for higher spins<sup>[96,107,108]</sup>. In particular, rich physics is expected for repulsive spin-3/2 fermions<sup>[109,110]</sup>, which at quarter filling may undergo a MI transition. Contrary to spin-1/2 case, the MI of spin-3/2 presents in one dimension two distinct magnetic phases given by a gapless spin liquid or a gapped dimerized phase, depending on the interatomic interactions. While for spin-1/2 spin-changing collisions are absent and the quadratic Zeeman effect (QZE) is irrelevant, the latter is crucial for higher spins, as shown in spinor condensates<sup>[87,111–113]</sup>. In spite of its experimental relevance, the QZE is mostly ignored in the analysis of the magnetic properties.

### III.1.a Short-range interactions in spinor condensates

As we discussed in previous chapters, in ultra cold gases, due to the extremely low energies considered, the most relevant interactions come from two-body *s*-wave collisions. However, on this analysis we neglected the spin degree of freedom.

Let us consider two identical particles with mass  $M$  and spin  $S$ . Since the total spin of the system during the collision is given by  $\vec{F} = \vec{S}_1 + \vec{S}_2$ , the possible values are thus  $F = 2S, 2S - 1, \dots, 0$  ( $F$  is conserved during the collision). However, depending on the statistical nature of the particles not all  $F$  are allowed. In the fermionic case, the total two-particle wave-function



should be anti-symmetric and since  $s$ -wave collisions are characterized by a symmetric spatial part, the spin part should remain anti-symmetric. The opposite holds for the bosons for which the two-body wave-function should always be symmetric. As a consequence for fermions with half-integer spin and bosons with integer spin, only channels with  $F$  even are possible.

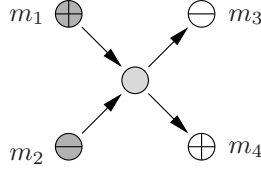


Figure III.1: Graphic scheme of a spin-changing collision that conserves the spin projection.

Furthermore, the isotropic nature of the short-range interactions preserves the pair spin projection along the quantization axis. This can be expressed by

$$(III.1) \quad m_1 + m_2 = m_3 + m_4,$$

as shown in Fig. III.1. The spin projection conservation can be realized in two non-equivalent ways. First, *spin-preserving* processes that take place when the outgoing particles are of the same kind as the incoming ones. This case means  $m_1 = m_4$  and  $m_2 = m_3$  in the figure. However, a more striking event may occur, the *spin-changing collision* (SCC) process, where the population of the different Zeeman sub-levels is redistributed, for instance  $\pm\frac{1}{2} \rightarrow \pm\frac{3}{2}$ . Throughout the following chapters, we will see that this process participates actively in the ground-state properties and dynamics of spinor gases.

Let us now resume the analysis of the  $s$ -wave collision when the spin is considered. In this case, the corresponding pseudo-potential is reduced to

$$(III.2) \quad \hat{V}(\vec{r}_1 - \vec{r}_2) = \delta(\vec{r}_1 - \vec{r}_2) \sum_{F=0}^{2S} g_F \hat{P}_F,$$

where the coupling strength for the  $F$ -channel is defined by

$$(III.3) \quad g_F = \frac{4\pi\hbar^2 a_F}{M},$$

with  $a_F$  the corresponding scattering length and  $\hat{P}_F$  the projection operator onto a two-particle state with total spin- $F$ , given by

$$(III.4) \quad \hat{P}_F = \sum_{m=-F}^F |F, m\rangle\langle F, m|.$$

Since those projectors are defined in the basis of the composed spin, they have to be re-expressed in terms of the incoming spins by means of the Clebsch-Gordan coefficients  $C_{m_1, m_2}^{F, m} = \langle m_1, m_2 | F, m \rangle$ ,

$$(III.5) \quad |F, m\rangle = \sum_{m_1, m_2 = -S}^S C_{m_1, m_2}^{F, m} |m_1, m_2\rangle.$$

Finally, the explicit expression of  $\hat{P}_F$  in terms of the spin operators is

$$(III.6) \quad \hat{P}_F = \mathcal{N} \prod_{m \neq F} \left[ \hat{S}_1 \cdot \hat{S}_2 - \frac{m(m+1)}{2} + S(S+1) \right],$$

where  $\mathcal{N}$  is a normalization constant. Below, we calculate explicitly these operators for particular examples when spin-3/2 fermions are considered. In this chapter, we discuss the derivation of an effective spin Hamiltonian for hard core spin-3/2 fermions in 1D lattices considering the QZE. We employ this Hamiltonian extensively in chapters IV and V.

## III.2 Effective spin Hamiltonian without QZE

We consider spin-3/2 fermions loaded in a deep one-dimensional optical lattice, such that at low filling only the lowest band is relevant. In this regime, the physics is given by the interplay between the nearest neighbor hopping, characterized by  $t$ , the externally controllable QZE parameterized by  $q$  and the  $s$ -wave collisions.

As mentioned above, the fermionic character of the particles requires the total wave function to be anti-symmetric. Therefore, from the Pauli exclusion principle, only two different channels are open for collision, namely, the channels with total spin  $F = 0$  and  $F = 2$ . By using the projectors (III.4), the two channels  $g_0$  and  $g_2$  lead to the following interaction Hamiltonian

$$(III.7) \quad \begin{aligned} \frac{1}{G} \hat{H}_I = & (1+g) \left[ \hat{\psi}_{-\frac{3}{2}}^\dagger \hat{\psi}_{-\frac{1}{2}}^\dagger \hat{\psi}_{-\frac{1}{2}} \hat{\psi}_{-\frac{3}{2}} + \hat{\psi}_{-\frac{3}{2}}^\dagger \hat{\psi}_{\frac{1}{2}}^\dagger \hat{\psi}_{\frac{1}{2}} \hat{\psi}_{-\frac{3}{2}} \right. \\ & \left. + \hat{\psi}_{-\frac{1}{2}}^\dagger \hat{\psi}_{\frac{3}{2}}^\dagger \hat{\psi}_{\frac{3}{2}} \hat{\psi}_{-\frac{1}{2}} + \hat{\psi}_{\frac{1}{2}}^\dagger \hat{\psi}_{\frac{3}{2}}^\dagger \hat{\psi}_{\frac{3}{2}} \hat{\psi}_{\frac{1}{2}} \right] \\ & + \left[ \hat{\psi}_{-\frac{3}{2}}^\dagger \hat{\psi}_{\frac{3}{2}}^\dagger \hat{\psi}_{\frac{3}{2}} \hat{\psi}_{-\frac{3}{2}} + \hat{\psi}_{-\frac{1}{2}}^\dagger \hat{\psi}_{\frac{1}{2}}^\dagger \hat{\psi}_{\frac{1}{2}} \hat{\psi}_{-\frac{1}{2}} \right] \\ & + g \left[ \hat{\psi}_{-\frac{3}{2}}^\dagger \hat{\psi}_{\frac{3}{2}}^\dagger \hat{\psi}_{\frac{1}{2}} \hat{\psi}_{-\frac{1}{2}} + \hat{\psi}_{-\frac{1}{2}}^\dagger \hat{\psi}_{\frac{1}{2}}^\dagger \hat{\psi}_{\frac{3}{2}} \hat{\psi}_{-\frac{3}{2}} \right], \end{aligned}$$

where  $G = (g_2 + g_0)/2$  is the energy unit ( $G \equiv 1$  henceforth) and

$$(III.8) \quad g = \frac{g_2 - g_0}{g_2 + g_0}.$$

Note that the last term in Eq. (III.7) characterizes spin-changing collisions, in which atoms in  $\pm 1/2$  are transferred into  $\pm 3/2$  and vice versa. It is clear that  $g$  is the coupling constant for SCC. All interactions preserve the overall magnetization, and hence, when an external magnetic field is added the linear Zeeman effect has no influence whatsoever on the dynamics.

The effective Hamiltonian of the system with one particle per site can be calculated with the help of the two-sites spin-manifold projectors<sup>[114]</sup>

$$(III.9) \quad \hat{P}_{i,j}(0) = \frac{(\vec{\tilde{S}}_i \cdot \vec{\tilde{S}}_j - \lambda_1)(\vec{\tilde{S}}_i \cdot \vec{\tilde{S}}_j - \lambda_2)(\vec{\tilde{S}}_i \cdot \vec{\tilde{S}}_j - \lambda_3)}{(\lambda_0 - \lambda_1)(\lambda_0 - \lambda_2)(\lambda_0 - \lambda_3)},$$

$$(III.10) \quad \hat{P}_{i,j}(2) = \frac{(\vec{\tilde{S}}_i \cdot \vec{\tilde{S}}_j - \lambda_0)(\vec{\tilde{S}}_i \cdot \vec{\tilde{S}}_j - \lambda_1)(\vec{\tilde{S}}_i \cdot \vec{\tilde{S}}_j - \lambda_3)}{(\lambda_2 - \lambda_0)(\lambda_2 - \lambda_1)(\lambda_2 - \lambda_3)},$$

where  $\lambda_F = \frac{1}{2}[F(F+1) - \frac{15}{2}]$  and  $\vec{\tilde{S}}_i \equiv (\hat{S}_i^x, \hat{S}_i^y, \hat{S}_i^z)$  is the vector of spin matrices defined on the site  $i$ . The final expression for the Hamiltonian reads

$$(III.11) \quad \hat{H}_{\text{eff}} = \sum_{\langle ij \rangle} [\epsilon_0 \hat{P}_{ij}(0) + \epsilon_2 \hat{P}_{ij}(2)].$$

with  $\epsilon_F = -4t^2/g_F$ <sup>[115]</sup>. In nature, typically the values of  $a_0$  and  $a_2$ , and thus  $g_0$  and  $g_2$ , are typically similar. However, they may be varied by means of micro-wave dressing<sup>[116]</sup> or optical Feshbach resonances<sup>[117]</sup>. In the relevant case of  $g_0 = g_2$ , the effective Hamiltonian reduces to

$$(III.12) \quad \hat{H}_{\text{eff}} = -\frac{4t^2}{g_0} \sum_{\langle ij \rangle} [\hat{P}_{ij}(0) + \hat{P}_{ij}(2)],$$

where

$$(III.13) \quad \hat{P}_{ij}(0) + \hat{P}_{ij}(2) = \frac{9}{16}(\vec{\tilde{S}}_i \cdot \vec{\tilde{S}}_j) - \frac{11}{36}(\vec{\tilde{S}}_i \cdot \vec{\tilde{S}}_j)^2 - \frac{1}{9}(\vec{\tilde{S}}_i \cdot \vec{\tilde{S}}_j)^3 + \frac{99}{64},$$

showing explicitly bilinear, biquadratic and bicubic terms. This is a consistent result since for spin- $F$  systems the corresponding Hamiltonian has a polynomial form in  $\vec{\tilde{S}}_i \cdot \vec{\tilde{S}}_j$  with power  $2F$ . This effective spin model also exhibits a uniform SU(4) symmetry and an exact solution has been obtained by the Bethe-ansatz method<sup>[118]</sup>.

### III.3 Effective spin Hamiltonian with QZE

Up to now, we considered no external magnetic field since any linear Zeeman effect can be gauged out. However, the quadratic Zeeman coupling may play






an important role since it imposes a gap between the manifold of spin projections  $m = \pm 1/2$  and  $m = \pm 3/2$ . The effect of the QZE is enhanced by the spin-changing collisions. The total Hamiltonian, with the addition of the hopping term and the chemical potential, is hence

$$(III.14) \quad \hat{H} = -t \sum_{im} \left( \hat{\psi}_{im}^\dagger \hat{\psi}_{i+1m} + \hat{\psi}_{i+1m}^\dagger \hat{\psi}_{im} \right) - \mu \sum_{im} \hat{\psi}_{im}^\dagger \hat{\psi}_{im} + q \sum_{im} m^2 \hat{\psi}_{im}^\dagger \hat{\psi}_{im} + \hat{H}_I,$$





For  $t \ll G$  and a sufficiently large chemical potential, the system enters into the Mott insulator phase with one particle per site. Under these conditions, the charge degrees of freedom are frozen and the spin degrees of freedom are characterized by an effective super-exchange Hamiltonian, that can be calculated by perturbation theory in the hopping.

The diagonalization of the unperturbed Hamiltonian is straightforward as shown below, where gray balls represent spin  $m = \pm 1/2$  particles, white balls  $m = \pm 3/2$  ones and the dashed ball a hole.

For the manifold of one particle (hole) per site the eigenstates and the corresponding eigenenergies are

State	Energy
	0
 , 	$\frac{1}{4}q - \mu$
 , 	$\frac{9}{4}q - \mu$







For two particles per site on the channel  $F = 2$  with spin projection  $m_F \neq 0$ :

State	Energy
 ,  ,  , 	$\frac{5}{2}q + (1 + g) - 2\mu$

The last pair of states to be considered are those with  $m_F = 0$ . In this case, the SCC plays a significant role exchanging population among them, thus we have to diagonalize the small matrix

$$(III.15) \quad \begin{pmatrix} \frac{1}{2}q & g \\ g & \frac{9}{2}q \end{pmatrix},$$

that acts on the states  and . Giving as a result the eigenstates

State	Energy
 = $\cos \theta$  + $\sin \theta$ 	$\lambda_+ - 2\mu$
 = $-\sin \theta$  + $\cos \theta$ 	$\lambda_- - 2\mu$



where






$$(III.16) \quad \tan \theta = \frac{1}{g} \left[ 2q + \sqrt{4q^2 + g^2} \right],$$

$$(III.17) \quad \lambda_{\pm} = 1 + \frac{5}{2}q \pm \sqrt{4q^2 + g^2}.$$

Now, Van-Vleck perturbation theory is used in order to retrieve the effective spin Hamiltonian<sup>[119]</sup>. We will follow the example of a spin changing process in order to calculate the expression

$$(III.18) \quad \langle n | \hat{H}_{\text{eff}}^{(2)} | n' \rangle = \frac{1}{2} \sum_{\nu} \langle n | \hat{H}_t | \nu \rangle \langle \nu | \hat{H}_t | n' \rangle \left[ \frac{1}{E_n - E_{\nu}} + \frac{1}{E_{n'} - E_{\nu}} \right],$$

where  $|n\rangle$  are the two-sites states with exactly one particle on each site and  $|\nu\rangle$  are the intermediate virtual states with pairs of particles on a single site. As an example, we consider the Hamiltonian matrix element that couples the states  and  which contains the SCC.

- Consider the initial state  whose energy is  $\frac{1}{2}q - 2\mu$ .
- The perturbation Hamiltonian, that is the hopping, sends both particles together in the state  with an amplitude  $t$ .
- Here we project into the eigenstates of the unperturbed Hamiltonian, for instance to .
- In order to make the hopping back, we again project to the state .
- The perturbation acts on the state sending one particle to the empty space, so we retrieve the desired target state .

A complete scheme of this procedure is depicted Fig. III.2, with all the possible paths from the initial state to the target state. The final result reads

$$(III.19) \quad c_{\text{sc}} = 2 \sin \theta \cos \theta \left[ \frac{\frac{5}{2}q - \lambda_+}{\left(\frac{1}{2}q - \lambda_+\right)\left(\frac{9}{2}q - \lambda_+\right)} - \frac{\frac{5}{2}q - \lambda_-}{\left(\frac{1}{2}q - \lambda_-\right)\left(\frac{9}{2}q - \lambda_-\right)} \right],$$

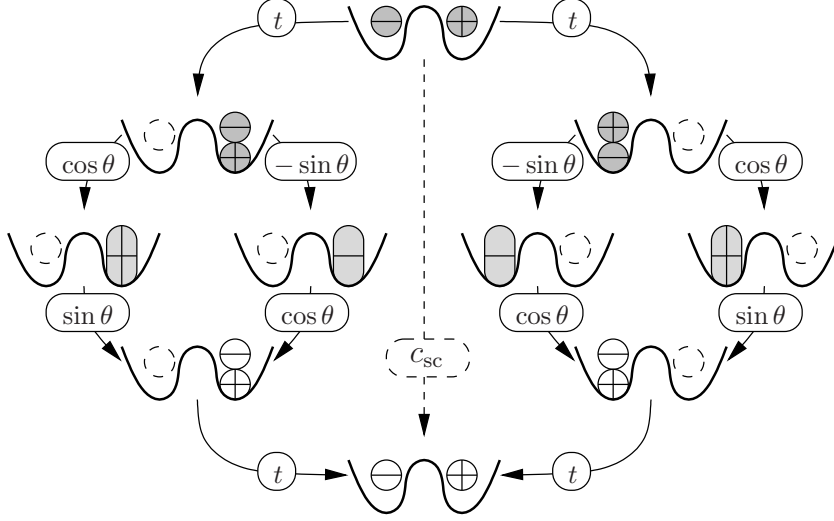


Figure III.2: Tree of the different processes that lead to the super-exchange mechanism of spin changing between the two spin manifolds. Initially two particles with spin  $-1/2$  and  $+1/2$  respectively became a pair  $-3/2 + 3/2$ .

An analog procedure can be done to calculate the remaining coefficients by scanning all the possible sources and target states, giving the values

$$(III.20) \quad c_{3/2} = 2t^2 \left[ \frac{\cos^2 \theta}{\frac{9}{2}q - \lambda_+} + \frac{\sin^2 \theta}{\frac{9}{2}q - \lambda_-} \right],$$

$$(III.21) \quad c_{1/2} = 2t^2 \left[ \frac{\cos^2 \theta}{\frac{1}{2}q - \lambda_-} + \frac{\sin^2 \theta}{\frac{1}{2}q - \lambda_+} \right],$$

$$(III.22) \quad c_2 = -\frac{2t^2}{g+1}.$$

The coefficient  $c_{|m|}$  characterizes the super-exchange between neighbor sites with local magnetizations  $m$  and  $-m$ , excluding SCC, while  $c_2$  does the same for pairs with  $|m_F| = 2$ , or in other words pairs  $m$  and  $m'$  such that  $|m| \neq |m'|$ . Finally,  $c_{sc}$  connects the manifold of  $\pm 3/2$  with  $\pm 1/2$  through a super-exchange with spin-changing collisions.

Note that the coefficients diverge for  $q_c = \pm(g^2 - 1)/4$  when the energy of at least one virtual state coincides with the energy of some real states. In this case, the Mott becomes unstable and the charge modes cannot be neglected. This case is out of the scope of this Thesis and we consider henceforth cases up to the vicinity of the resonances. By combining the coefficients and the states together, the effective Hamiltonian is

$$(III.23) \quad \hat{H}_{\text{eff}} = \sum_i \hat{H}_{i,i+1} + q \sum_{i,m} m^2 \hat{n}_{m,i},$$

where  $\hat{n}_{m,i} = \hat{\psi}_{m,i}^\dagger \hat{\psi}_{m,i}$  is the number particle operator for the  $m$ -component of the spin at the site  $i$ , and

$$\begin{aligned}
 \text{(III.24)} \quad \hat{H}_{i,j} = & c_2 \sum_{|m| \neq |m'|} \left[ \hat{n}_{m,i} \hat{n}_{m',j} - \hat{\psi}_{m,i}^\dagger \hat{\psi}_{m',j}^\dagger \hat{\psi}_{m,j} \hat{\psi}_{m',i} \right] \\
 & + \sum_{|m|=\frac{3}{2}} c_{|m|} \left[ \hat{n}_{m,i} \hat{n}_{-m,j} - \hat{\psi}_{m,i}^\dagger \hat{\psi}_{-m,j}^\dagger \hat{\psi}_{m,j} \hat{\psi}_{-m,i} \right] \\
 & + c_{\text{sc}} \left\{ \left[ \hat{\psi}_{-\frac{1}{2},i}^\dagger \hat{\psi}_{\frac{1}{2},j}^\dagger - \hat{\psi}_{\frac{1}{2},i}^\dagger \hat{\psi}_{-\frac{1}{2},j}^\dagger \right] \left[ \hat{\psi}_{\frac{3}{2},i} \hat{\psi}_{-\frac{3}{2},j} - \hat{\psi}_{-\frac{3}{2},i} \hat{\psi}_{\frac{3}{2},j} \right] + \text{h.c.} \right\}.
 \end{aligned}$$

This resulting Hamiltonian has a complicated expression in terms of the spin operators. However, the matrix representation of it is quite simple and allow numerical calculations in a very direct way. In the next chapters, we make use of this feature in order to characterize both dynamics and ground state properties.





## Repulsively bound exciton-biexciton states in spin-3/2 chains

In this chapter, we show that the interplay between spin-changing collisions and quadratic Zeeman coupling provides a novel mechanism for the formation of repulsively bound composites in high spin fermionic gases. In order to illustrate this idea, spin flips in an initially polarized hard-core 1D Mott insulator of spin 3/2-fermions are considered. The analysis of the conditions for the existence of these bound states and a discussion of their intriguing properties is also presented. It is shown that the effective mass and stability of the composites depend non-trivially on the spin-changing collisions, the quadratic Zeeman effect and the initial exciton localization. At the end of the chapter, the stability of the composites against inelastic collisions is also demonstrated. This fact opens the possibility of novel quantum composite phases.

The great advantage of optical lattices over standard condensed-matter systems, where the interactions with phonons would lead to a large dimer population damping, is that they provide a dissipation free environment to a large extent, allowing for a suitable scenario for the study of the intriguing physics of meta-stable bound states and other transient phenomena far from equilibrium<sup>[48]</sup>.

Due to the natural discreteness that optical lattices offer, novel possibilities of composite formation are allowed with ultracold atoms. For instance, the local on-site dimer formation in lattices with attractive interaction<sup>[120,121]</sup> and fermionic composites in Bose-Fermi mixtures<sup>[122]</sup>. An even more striking effect of the lattice discreteness, is provided by the recent observation of repulsively bound atomic pairs (doublons) at a given lattice site, which are dynamically stable in the absence of dissipation<sup>[70,123]</sup>. Repulsively on-site bound pairs of spin-1/2 fermions are formed since the large interaction energy of the doublon cannot be released by the maximal kinetic energy for two atoms in the lowest band, which in turn is proportional to the hopping energy<sup>[124]</sup>. The dependence of the doublon life time on the interaction strength has been

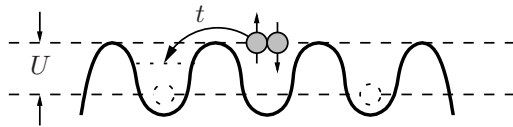


Figure IV.1: Doublon stability in an optical lattice. When the repulsive interaction is large enough in comparison to the hopping,  $U \gg t$ , energy conservation forces the particles to remain together in a single site.

use to to detect antiferromagnetic order and probe the nature of quasi-particle excitations in a fermionic Mott insulator employing optical lattice modulation spectroscopy<sup>[125,126]</sup>. Furthermore, the modulation of the lattice, generates a crossover in the nature of doublon-hole excitations from a Fermi Golden Rule regime to damped Rabi oscillations<sup>[127]</sup>. This kind of excitations has been widely studied and possible applications in cooling techniques and even solar cells have been proposed<sup>[128–130]</sup>.

It is important to note that repulsively bound pairs are stable under collisions with each other for sufficiently large interaction where, by energy arguments, the elastic scattering between pairs is the only open channel. This means that even a relatively dense quantum lattice gas of these objects can be long-lived. However, the dynamics of the collisions and details of the decay depend crucially on lattice depth and the local density of pairs across the lattice<sup>[123]</sup>.

Our main goal in this chapter is to show that a completely different mechanism based on the interplay between spin-changing collisions (SCC) and quadratic Zeeman effect (QZE) may sustain a novel type of composites for repulsive high-spin lattice fermions. We illustrate this physics for the case of hard-core 1D spin-3/2 in a Mott insulator where the particle in each site is initially polarized in the  $z$  component of the spin projection  $m = -3/2$ . We also show that spin flips into  $m = +3/2$  may lead to two types of composites formed by an *exciton*, that is a pair of a particle with  $m = +3/2$  and a hole of  $m = -3/2$ ; and an anti-symmetric *biexciton* which is made of two  $m = -3/2$  holes and two particles with  $m = +1/2$  and  $m = -1/2$ . A simple scheme can be seen in Fig. IV.2.

We characterize the dynamics and stability of exciton and biexciton composites and we found that they exhibit a non-trivial dependence on the spin-changing interactions, the quadratic Zeeman effect and the center of mass momentum. Finally, we show that inelastic-composite-composite interactions may be very inefficient, opening exciting possibilities for many-body composite gases.

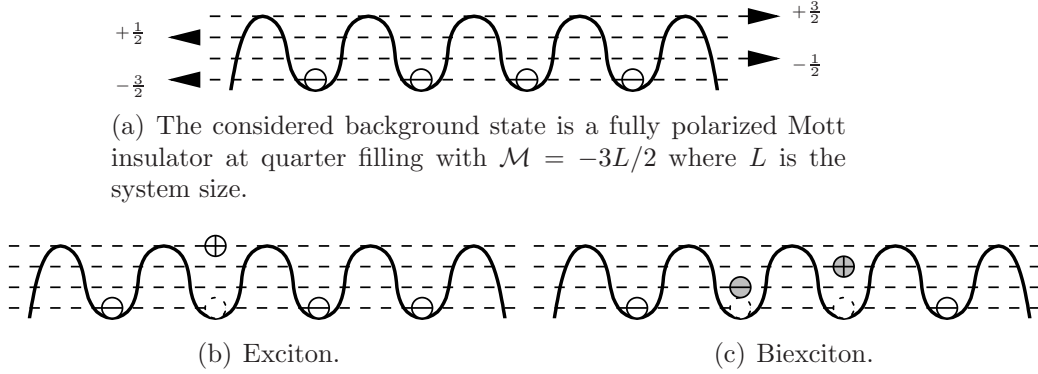


Figure IV.2: Background state (a) and excitations considered in this chapter. An single spin flip into  $m = 3/2$  consist of the annihilation of the state  $m = -3/2$  and the creation of  $m = 3/2$  and hence an exciton (a). When the exciton interacts with the background it can become a biexciton made of two  $m = -3/2$  holes and two particles with  $m = 1/2$  and  $m = -1/2$  respectively (b).

## IV.1 Single-flip excitations

We consider an initial background state,  $|\phi_{\text{BG}}\rangle$ , in which all hard-core fermions are polarized into the state  $m = -3/2$  and we assume that the system is in the Mott-insulator regime and therefore no empty sites are present. The state has a total magnetization  $\mathcal{M} = -3L/2$ , where  $L$  is the number of lattice sites. Note that the state is stable because the collisions preserve  $\mathcal{M}$ . Furthermore, this state is both experimentally and theoretically straightforward to implement where in the latter case it is described by the expression

$$(IV.1) \quad |\phi_{\text{BG}}\rangle = \prod_{i=1}^L \psi_{-\frac{3}{2},i}^\dagger |\emptyset\rangle,$$

which is an eigenstate of the system such that  $\hat{H}_{\text{eff}}|\phi_{\text{BG}}\rangle = E_{\text{BG}}|\phi_{\text{BG}}\rangle$  where  $E_{\text{BG}} \equiv \frac{9}{4}qL$ . The state is sketched in Fig. IV.2(a). On top of this state, we impose excitations of the form

$$(IV.2) \quad |m, j\rangle \equiv \hat{\psi}_{m,j}^\dagger \hat{\psi}_{-\frac{3}{2},j} |\phi_{\text{BG}}\rangle,$$

which have actually an *exciton*-like character. This can be understood from the fact that they are formed by a particle (with  $m \neq -3/2$ ) and a hole (in  $m = -3/2$ ). A clear scheme of the excitons is presented in Fig. IV.2 in panels (b) and (c) respectively.

The simplest exciton-like perturbation consists of the creation of one exciton of either spin  $\pm\frac{1}{2}$  at any place of the chain. Without losing any generality, we consider the  $\frac{1}{2}$ -exciton  $|\frac{1}{2}, j\rangle$ . The underlying Hamiltonian of such perturbation can be obtained straightforward from (III.23), recalling that only the

$c_2$  processes contribute and that the total magnetization is preserved, giving

$$(IV.3) \quad \langle \frac{1}{2}, i | \hat{H}_{\text{eff}} - E_{\text{BG}} | \frac{1}{2}, j \rangle = (2c_2 - 2q)\delta_i^j - c_2 [\delta_i^{j+1} + \delta_i^{j-1}],$$

with  $\delta_i^j$  the Kronecker delta.

In this case, the Hamiltonian can be diagonalized since the  $\frac{1}{2}$ -exciton propagates freely throughout the lattice with an energy  $E_2(k) - 2q$  where

$$(IV.4) \quad E_m(k) = 2c_m(1 - \cos k).$$

with  $k$  the center-of-mass momentum of the  $\frac{1}{2}$ -exciton. We find an analogous case when we consider the exciton  $|\frac{3}{2}, j\rangle$  with  $g \equiv 0$ . Since the spin-changing collisions vanish, the manifolds  $\pm 3/2$  and  $\pm 1/2$  are totally independent. Therefore, we have

$$(IV.5) \quad \langle \frac{3}{2}, i | \hat{H}_{\text{eff}} - E_{\text{BG}} | \frac{3}{2}, j \rangle = 2c_{3/2}\delta_i^j - c_{3/2} [\delta_i^{j+1} + \delta_i^{j-1}],$$

that leads to the dispersion relation  $E_{3/2}(k)$  just by taking  $m = 3/2$  on the Eq. (IV.4).

## IV.2 Exciton-biexciton repulsively bound states

When the spin-changing collisions are included, the creation of the exciton  $|\frac{3}{2}, i\rangle$  on top of the background will show a very different scenario, since one biexciton may be created at expense of the exciton. Such biexciton is described by

$$(IV.6) \quad |m, j : -m, j + 1\rangle \equiv \hat{\psi}_{m,j}^\dagger \hat{\psi}_{-m,j+1}^\dagger \hat{\psi}_{-\frac{3}{2},j+1} \hat{\psi}_{-\frac{3}{2},j} |\phi_{\text{BG}}\rangle.$$

An image of this kind of states is displayed in Fig. IV.2(c). A further superexchange process may split up the recently created biexciton into two separated  $\pm \frac{1}{2}$ -excitons by swapping one of them with the neighboring background spins. Following processes of the same kind will drag the  $\pm \frac{1}{2}$ -excitons further away reducing on each step the probability of recombination. This suggests that the exciton will tend always to dissolve into separated  $\pm \frac{1}{2}$ -excitons. However, contrary to this expectation, repulsively bound states can be formed, where the exciton gets dressed with the biexciton becoming stable and robust.

In order to focus into this phenomenon, let us first have a look into the full effect of the Hamiltonian on the exciton  $|\frac{3}{2}, j\rangle$ :

$$(IV.7) \quad \begin{aligned} \left[ \hat{H}_{\text{eff}} - E_{\text{BG}} \right] | \frac{3}{2}, j \rangle = & -c_{3/2} [ | \frac{3}{2}, j + 1 \rangle + | \frac{3}{2}, j - 1 \rangle ] + 2c_{3/2} | \frac{3}{2}, j \rangle \\ & + c_{\text{sc}} [ | \frac{1}{2}, j : -\frac{1}{2}, j + 1 \rangle - | -\frac{1}{2}, j : \frac{1}{2}, j + 1 \rangle \\ & + | -\frac{1}{2}, j - 1 : \frac{1}{2}, j \rangle - | \frac{1}{2}, j - 1 : -\frac{1}{2}, j \rangle ]. \end{aligned}$$

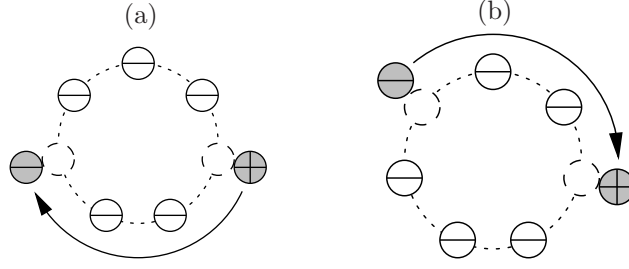


Figure IV.3: Scheme of the states  $|k^\pm, \Delta\rangle$  for  $L$  odd and periodic boundary conditions. When one of the exciton moves from a distance  $(L-1)/2$  to  $(L+1)/2$ , the description of the state changes from  $|k_{(L-1)/2}^+\rangle$  (a) to  $|k_{(L-1)/2}^-\rangle$  (b).

The first two terms are those we already knew from the case with no SCC, and can be solved in the center-of-mass momentum frame work. The second term, interestingly, suggests that only anti-symmetrical combinations of biexcitons are reachable by the exciton. According to this regard, we introduce the Fourier transformed states<sup>[131]</sup>

$$(IV.8) \quad |k, \frac{3}{2}\rangle \equiv \frac{1}{\sqrt{L}} \sum_{j=1}^L e^{ikj} | \frac{3}{2}, j \rangle,$$

$$(IV.9) \quad |k^\pm, \Delta\rangle \equiv \frac{1}{\sqrt{L}} \sum_{j=1}^L e^{ik(j+\Delta/2)} | \pm \frac{1}{2}, j : \mp \frac{1}{2}, j + \Delta \rangle,$$

with the constrain  $0 < \Delta \leq (L-1)/2$  and the number of sites  $L$  odd. They are depicted Fig. IV.3.  $\Delta$  is interpreted as the distance between the two  $\pm \frac{1}{2}$ -excitons. From those states one can also define the symmetric and anti-symmetric counter parts

$$(IV.10) \quad |k^{S,A}, \Delta\rangle = \frac{1}{\sqrt{2}} [ |k^+, \Delta\rangle \pm |k^-, \Delta\rangle ].$$

It is easy to verify that the symmetric states are decoupled by calculating the underlying Hamiltonian that acts on this manifold. Then, we have

$$(IV.11) \quad \begin{aligned} \hat{H}_{\text{eff}}^S(k) = & (2c_2 - 4q) |k^S, 1\rangle \langle k^S, 1| + 4(c_2 - q) \sum_{j>1} |k^S, j\rangle \langle k^S, j| \\ & - 2c_2 \cos \frac{k}{2} \sum_j [ |k^S, j+1\rangle \langle k^S, j| + \text{h.c.} ]; \end{aligned}$$

so the  $\{|k^S, j\rangle\}$  form a closed set and, because of that, we will not consider them any further.

In the remaining manifold, for a given momentum  $k$ , the underlying Hamiltonian for the coupled system of exciton and the anti-symmetric states can

be written in the form

$$\begin{aligned}
\hat{H}_{\text{eff}}^{A, \frac{3}{2}} &= E_1^A |k^A, 1\rangle \langle k^A, 1| + 4(c_2 - q) \sum_{j>1} |k^A, j\rangle \langle k^A, j| \\
\text{(IV.12)} \quad &- 2c_2 \cos \frac{k}{2} \sum_j [|k^A, j+1\rangle \langle k^A, j| + \text{h.c.}] \\
&+ E_{3/2}(k) |k, \frac{3}{2}\rangle \langle k, \frac{3}{2}| + \Omega_{\text{sc}}(k) \left[ i e^{i\frac{k}{2}} |k, \frac{3}{2}\rangle \langle k^A, 1| + \text{h.c.} \right],
\end{aligned}$$

where  $\Omega_{\text{sc}}(k) = 2\sqrt{2}c_{\text{sc}} \sin(k/2)$  and  $E_1^A = 2(c_2 + c_{1/2} - 2q)$ .

From the numerical treatment point of view, the advantage of this reformulation of the problem lays on the significant reduction of the matrix to diagonalize. When all the states are taken into account as in Eq. (III.23), the Hilbert space dimension is  $L^2$  and the full diagonalization of the system would be rather costly, allowing up to a few dozens of sites. However, in order to diagonalize (IV.12), one deals with a tridiagonal  $L \times L$  matrix, making possible to consider a number of sites of the order of hundred or even more.

An example of the typical spectrum is shown in Fig. IV.4. On it, the similarity to the spectrum of self-bound repulsive pairs of spin-1/2 fermions is quite clear<sup>[123]</sup>. The unbounded biexciton solutions form a continuous band (sea) due to their free relative motion with an effective hopping  $\Omega_2(k) = 2c_2 \cos(k/2)$  that leads to the dispersion

$$\text{(IV.13)} \quad E^{\text{B}}(k, k_r) = 4(c_2 - q) + 2\Omega_2(k) \cos k_r,$$

where  $k_r$  is the relative momentum of the pair. In the figure, it is also clear the appearance of up to three bound states, resembling also the case of repulsive spin-1/2 fermions with nearest neighbor interactions<sup>[131]</sup>. Moreover, there is a band of bound pairs above the sea of unbounded biexcitons in both cases (a) and (b). This band has the dispersion relation

$$\text{(IV.14)} \quad E^{\text{S}}(k) = 2c_2(1 - \cos^2(k/2)) - 4q,$$

belonging to the symmetric manifold. As we mentioned above, this band is completely decoupled from the exciton. Henceforth, we will focus on the analysis of the remaining bands where the dressed exciton becomes stable.

### IV.2.a Pairing of excitons and anti-symmetric biexcitons

The remaining pair of bounded states are composed by a linear combination of the exciton  $|k, \frac{3}{2}\rangle$ , the anti-symmetric biexciton  $|k^A, 1\rangle$  and the unbounded biexcitons  $|k^A, \Delta\rangle$  with a probability amplitude that decay exponentially on  $\Delta$  as shown in Fig. IV.5. Therefore, in order to understand the structure of

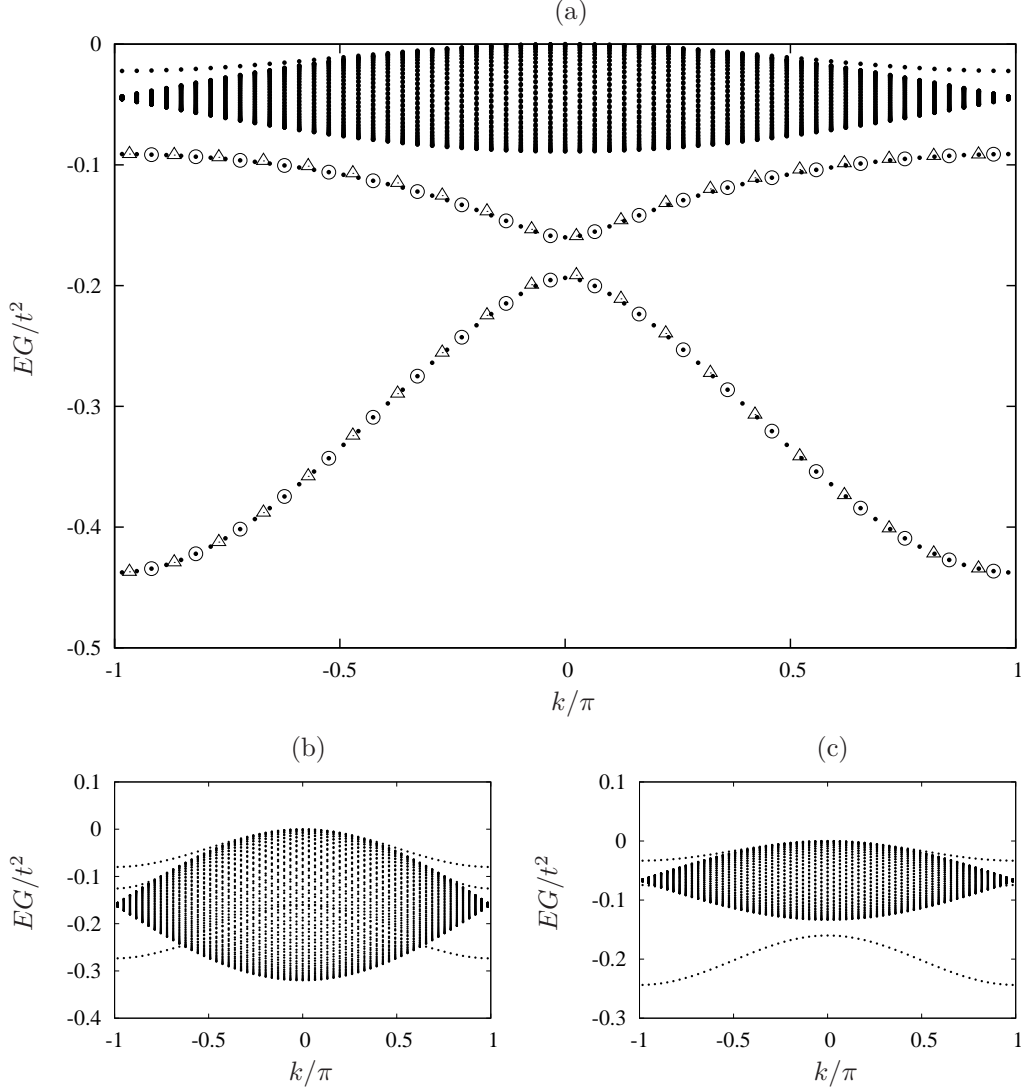


Figure IV.4: Band spectrum for the excitations as a function of the quasi-momentum  $k$ , for  $q = -4G$  and  $L = 121$ . The dots are the results of the exact diagonalization of the Hamiltonian  $\hat{H}_{\text{eff}}^{A, \frac{3}{2}}$  while the open circles are the result of the band analysis using the ansatz (IV.15) in section IV.2.a and with triangles the band structure of the Hamiltonian (IV.24). In (a) the two bands  $E_{\lambda}^{\pm}(k)$  are very well defined for  $g = 0.8G$ , while for  $g = -0.5G$  in (b) and  $g = 0.2G$  in (c), they are immersed in the sea of unbounded biexcitons and thus the analytical description fails.

those states, we introduce an ansatz that fits to the observed behavior:

$$(IV.15) \quad |\phi_k\rangle = \cos \alpha \sum_{\Delta=1}^{(L-1)/2} (-1)^{\Delta-1} e^{-(\Delta-1)/\gamma} |k^A, \Delta\rangle + i \sin \alpha |k, \frac{3}{2}\rangle,$$

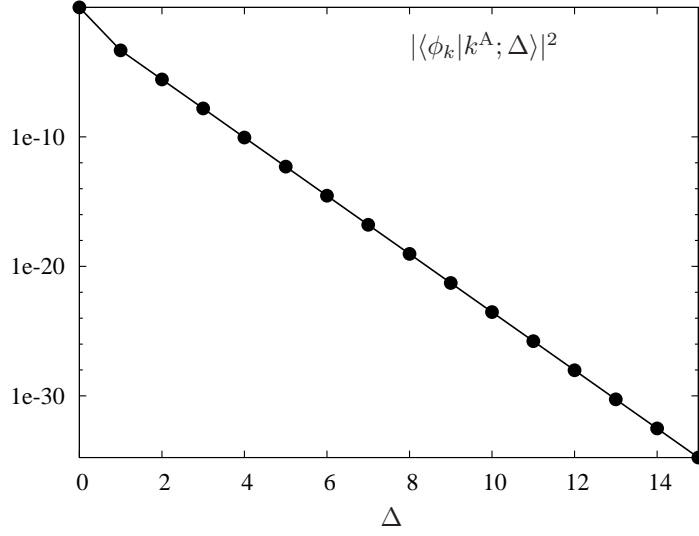


Figure IV.5: Numerically retrieved probability distribution for the dressed exciton with  $q = -10t^2$ ,  $g = 0.5$ ,  $k = \pi/8$  and  $L = 121$  in semi-log scale. The point for  $\Delta = 0$  represents  $|\langle \phi_k | k, \frac{3}{2} \rangle|^2$ . For  $\Delta \geq 1$  a clear exponential decay is presented.

where the exponent gives information about the localization length  $\gamma$ . Now we impose  $|\phi_k\rangle$  to be an eigenstate of the system

$$(IV.16) \quad \hat{H}_{\text{eff}}^{A, \frac{3}{2}} |\phi_k\rangle = E_\gamma(k) |\phi_k\rangle,$$

that becomes the transcendent equation for  $\gamma$

$$(IV.17) \quad 4(c_2 - q) + 2\Omega_2(k) \cosh(1/\gamma) = \frac{1}{2}\Gamma_+(k) \pm \frac{1}{2}\sqrt{\Gamma_-^2(k) + 4\Omega_{\text{sc}}^2(k)},$$

where

$$(IV.18) \quad \Gamma_\pm(k) = E_1^A + \Omega_2(k)e^{1/\gamma} \pm E_{3/2}(k).$$

Each bound state is related to a different solution  $\gamma_\pm$ , and therefore we are able to reproduce the two corresponding bands. In order to do so, we need to know the relation between the energy and the localization length. Considering Eq. (IV.16) for any unbounded biexciton with  $\Delta > 1$  we obtain

$$(IV.19) \quad E_\gamma^\pm(k) = 4(c_2 - q) + 2\Omega_2(k) \cosh(1/\gamma_\pm(k)).$$

The results of the numerical solution of Eq. (IV.17) were used to calculate the band diagram, depicted in Fig. IV.4 with open circles, by plugging them into the dispersion relation (IV.19). An excellent agreement with the exact



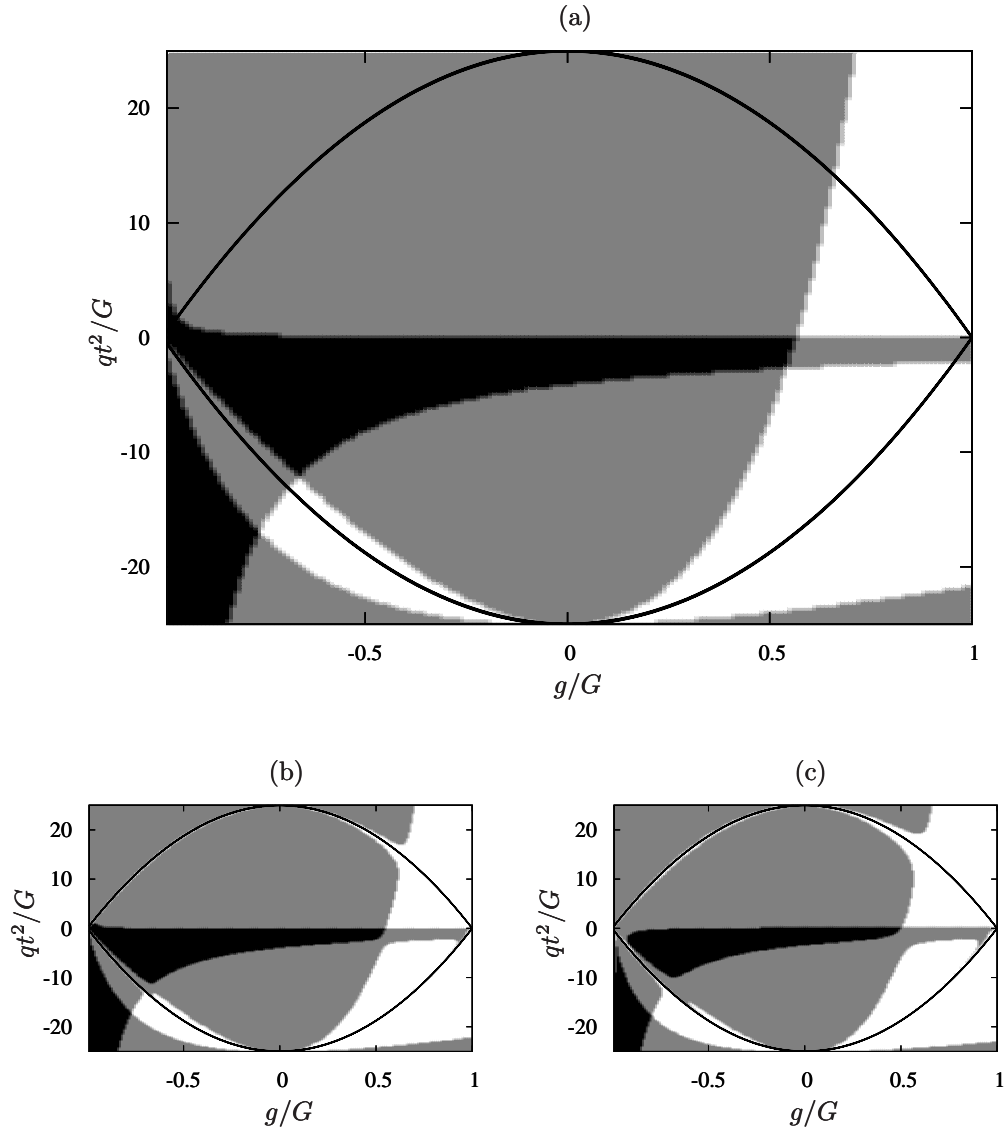


Figure IV.6: Phase diagram of the number of bound states: 0(black), 1(grey) and 2(white), for  $k = 0$  (a),  $k = \pi/2$  (b) and  $k = \pi$  (c). The hopping is the constant  $t = 0.1G$ . The two black parabolas are the resonances where the approximation of one particle per site breaks down.

diagonalization of the Hamiltonian (IV.12) can be seen. This correspondence shows that the ansatz (IV.15) reproduces faithfully the shape of the wave function while the localization length remains finite.

In order to determine when the ansatz fails, we note that for a given momentum  $k$ , the gap  $\Delta_B(k)$  between the closest band to the unbounded biexcitons sea and the sea itself can be calculated from Eq. (IV.13) and (IV.19).

The size of the gap is

$$(IV.20) \quad \Delta_B(k) = 2\Omega_2(k) \left[ 1 - \cosh\left(\frac{1}{\gamma_{\pm}(k)}\right) \right].$$

From this result it is clear that when this gap reduces, the localization length increases, diverging for  $\Delta_B \rightarrow 0$ . In this limit, the biexciton is no longer a bound state. Since  $\gamma_{\pm}(k)$  depends non-trivially on the system parameters (QZE, SCC and exciton momentum) the existence of both the biexciton and the exciton bound states will also show an intricate relation with the system parameters. In Fig. IV.6 a scan of the number of bound states on the parameter space at several values of the momentum is presented.

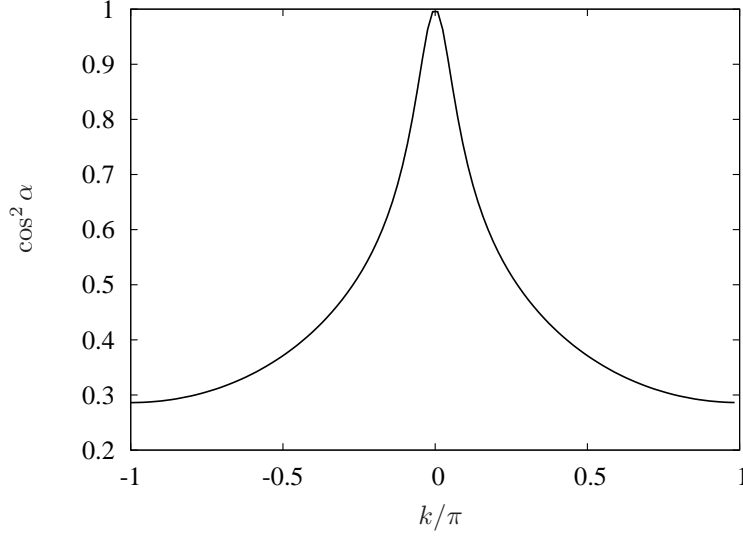


Figure IV.7: Exciton contribution into the exciton dressed state. At  $k = 0$  there is no dressing while for  $k \sim \pm\pi$  it is only of about 30%.

When the localization length is small enough, it is possible to neglect the coupling to the the unbounded biexcitons and to consider only the two bands of bound states. This condition is fulfilled when the matrix element that couples the biexciton with the unbounded sea is much smaller that the gap. This requirement reduces to

$$(IV.21) \quad \left| \frac{c_{1/2}}{c_2} - 1 \right| \gg 1.$$

Then, neglecting the biexciton sea, the underlying Hamiltonian (IV.12) becomes

$$(IV.22) \quad \hat{H}_{\text{eff}}^{A, \frac{3}{2}}(k) = E_{3/2}(k) |k, \frac{3}{2}\rangle \langle k, \frac{3}{2}| + E_1^A |k^A, 1\rangle \langle k^A, 1| \\ + \Omega_{\text{sc}}(k) \left[ i e^{i\frac{k}{2}} |k, \frac{3}{2}\rangle \langle k^A, 1| + \text{h.c.} \right].$$

This Hamiltonian holds for the white regions in Fig. IV.6 where the two bands are isolated. Moreover, with the transformation

$$(IV.23) \quad \begin{pmatrix} |k, \frac{3}{2}\rangle \\ |k^A, 1\rangle \end{pmatrix} = \begin{pmatrix} i \cos \alpha & \sin \alpha e^{i\frac{k}{2}} \\ -\sin \alpha e^{-i\frac{k}{2}} & -i \cos \alpha \end{pmatrix} \begin{pmatrix} |\phi_k^+\rangle \\ |\phi_k^-\rangle \end{pmatrix}$$

the hamiltonian becomes

$$(IV.24) \quad \hat{H}_{\text{eff}}^{A, \frac{3}{2}}(k) = [E_{3/2}(k) \cos^2 \alpha + E_1^A \sin^2 \alpha + 4 \cos \alpha \sin \alpha \sin(k/2)] |\phi_k^+\rangle \langle \phi_k^+| \\ + [E_{3/2}(k) \sin^2 \alpha + E_1^A \cos^2 \alpha - 4 \cos \alpha \sin \alpha \sin(k/2)] |\phi_k^-\rangle \langle \phi_k^-|,$$

with the mixing angle

$$(IV.25) \quad \tan \alpha = \frac{E_1^A - E_{3/2}(k) + \sqrt{[E_1^A - E_{3/2}(k)]^2 + 4\Omega_{\text{sc}}^2(k)}}{\Omega_{\text{sc}}^2(k)}.$$

From the equations above and the Fig. IV.7, where a plot of  $\cos^2 \alpha$  is shown, it is even more clear that the bands correspond to both exciton with a biexciton dressing and vice versa. The band structure of this Hamiltonian is also displayed on Fig. IV.4(a).

### IV.3 Dynamical properties of the bound pairs

The contribution of the exciton to the bound states ( $\sin^2 \alpha^\pm$ ) is important for the understanding of the dynamics after a spin-flip. In order to calculate  $\alpha$  we use the projected Schrödinger equation

$$(IV.26) \quad \langle k, \frac{3}{2} | \hat{H}_{\text{eff}}^{A, \frac{3}{2}} | \phi_k \rangle = iE_\gamma^\pm(k) \sin \alpha,$$

and the dispersion relation (IV.19). After equating for the mixing angle  $\alpha$ , we get

$$(IV.27) \quad \tan \alpha^\pm(k) = \frac{1}{\Omega_{\text{sc}}(k)} [E_\gamma^\pm(k) - \Omega_2(k)e^{-1/\gamma^\pm(k)} - E_1^A].$$

Here we analyze two interesting extreme cases. First, at exactly  $k = 0$ , where the center of mass of the initial perturbation is maximally delocalized, the coefficient that mixes the exciton with the set of biexcitons vanishes, or in other words  $\Omega_{\text{sc}}(k = 0) \equiv 0$ . Then,  $\alpha = \pi/2$  and therefore, one of the bound states is a pure exciton with energy  $E_\gamma^-(0) = E_{3/2}(0)$  while the other one is a linear combination of the biexcitons  $|k^A, \Delta\rangle$  with eigenenergy

$$(IV.28) \quad E_\gamma^+(0) = E_1^A + \frac{2c_2^2}{c_2 + c_{1/2} - 2q}.$$

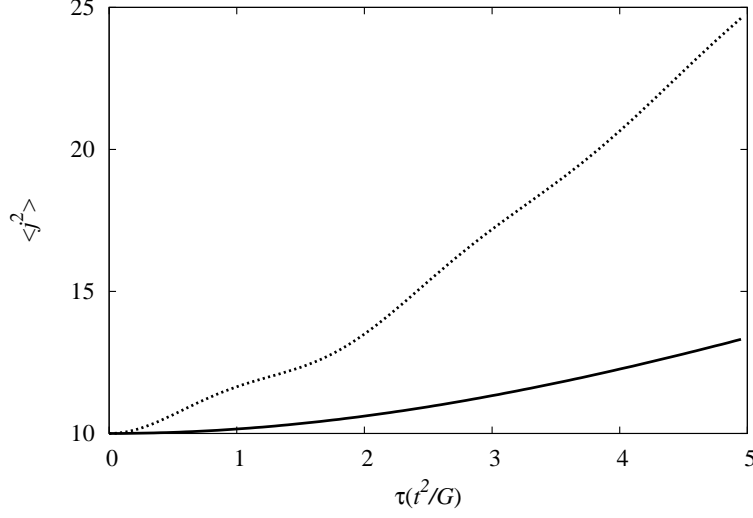


Figure IV.8: Time evolution of the width of the exciton wave packet for  $t = 0.1G$ ,  $g = 0.8G$ ,  $qt^2/G = -4$  and  $L = 100$ . The solid line plots results without spin-changing collisions and the dashed line the case when such interaction is included. The initial state is a square wave-packet of 10 sites wide.

For this particular state, the localization length is given by

$$(IV.29) \quad \gamma_+(0) = \left[ \ln \left( 1 + \frac{c_{1/2} - 2q}{c_2} \right) \right]^{-1}.$$

The second extreme case, when the perturbation is highly localized, has a very distorted dynamics. This can be understood from the fact that the coupling between the exciton and the biexciton and consequently the sea of unbounded biexcitons is rather strong. This leads to the dissolution of the exciton when at least for some momentum interval only one of the two bands has a finite localization length.

### IV.3.a Delocalized spin-flip excitations

When no SCC are allowed, the effective mass of the excitons  $M_{\frac{3}{2}}^{*0}$  at  $k = 0$  can be obtained using the dispersion relation  $E_{3/2}(k)$  from (IV.4) as

$$(IV.30) \quad M_{\frac{3}{2}}^{*0} = \frac{1}{2c_{3/2}}.$$

However, this is not generally the case. Although for a very delocalized spin-flip ( $k \approx 0$ ), the spin-3/2 exciton is in itself one of the bound states, the SCC significantly distorts the effective mass of the exciton:

$$(IV.31) \quad \frac{1}{M_{\frac{3}{2}}^*} \approx \frac{1}{M_{\frac{3}{2}}^{*0}} - \frac{2c_{sc}^2}{c_2 + c_{1/2} - 4q}.$$

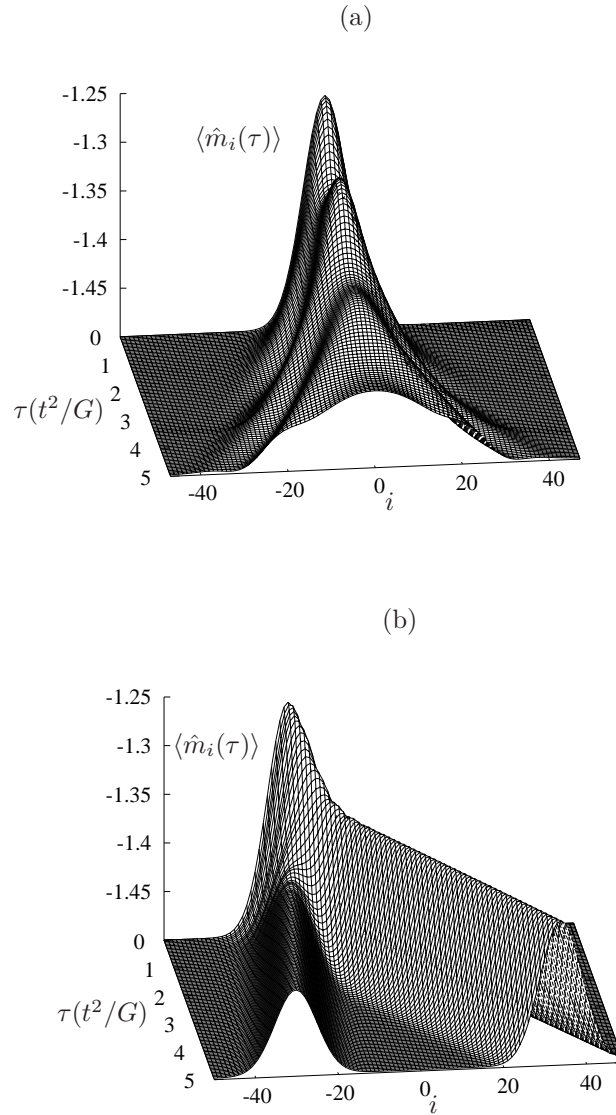


Figure IV.9: Density plot of the spin chain magnetization on time for an initial Gaussian wave packet of one exciton at  $\langle i^2 \rangle = 10$  with  $t = 0.1G$ ,  $qt^2/G = -4$ ,  $g = 0.8G$  and  $L = 100$ . (a) For  $k = 0$  the wave packet gets wider with two components. (b) For  $k = \pi/2$  there are two clearly distinguishable outgoing packets corresponding to the two bound states that the exciton projects into.

Note that the two effective masses differ notoriously since they even may have opposite sign. This fact modifies radically the exciton wave-packet dynamics. A particular example is illustrated in Fig. IV.8, where an initially wide spin-3/2 wave packet diffuses throughout the lattice in very different ways in the presence or absence of SCC.

In the case of a wave packet centered on a given finite momentum  $k_0$ , the mixture between the states  $|k, \frac{3}{2}\rangle$  and  $|k^A, \Delta\rangle$  is higher. Thus, the contributions of both bounded states will be reflected in the dynamics. Since each component has a different group velocity, two out-going wave-packets are expected. This remarkable behavior is depicted in Fig. IV.9(b).

### IV.3.b Localized spin-flip excitations

Up to now, we have analyzed the system when the conditions are such that at least two bands exist for a wide enough range of momentum. In this case, any initial state of excitons will be projected into the dressed states  $|\phi_k^\pm\rangle$  that evolve independently. However, the situation is markedly different if the initial perturbation is strongly localized and thus all the momenta within the Brillouin zone contribute. In the particular case of the two totally isolated bands, still the projection into the bound states holds and two outgoing wave packets can be seen. Moreover, if the initial configuration is such that  $k = 0$  two opposite propagating packets appear as shown in Fig. IV.10(a). However, from Fig. IV.6 is then clear that for a large set of parameters only one or even zero bands exists. This means that the localization length diverges at least for one of the bound states and the population of unbounded biexcitons is significant, dissolving the initial exciton. A clear example of this evolution is shown in Fig. IV.10(b). Although the same initial conditions as in (a) were taken, no clear outgoing wave-packet is visible, on the contrary a strong diffusion occurs.

## IV.4 Multiple spin-flip excitations

Up to this point, we have considered the dynamics after single-flip excitations. Although single spin flips may be created using state-of-the-art techniques for single addressing<sup>[132,133]</sup>, in a typical experiment, however, more than one spin-flip will be induced. As a result, several excitons will be simultaneously created, hence opening the possibility of inelastic exciton-exciton collisions which may open a decay channel for them into unbounded biexciton pairs. The various initial spin-flip excitations result in a complicated many-body non-equilibrium dynamics for the created bound composites. In order to evaluate this multi-exciton dynamics, we have performed time-dependent MPS calculations for 1, 3 and 5 non-localized excitons.

As shown in Fig. IV.11, where the conditions are set for the two bands of the bounded states to be isolated, the population of excitons remains stable even after a time long enough for several collisions to take place. During the

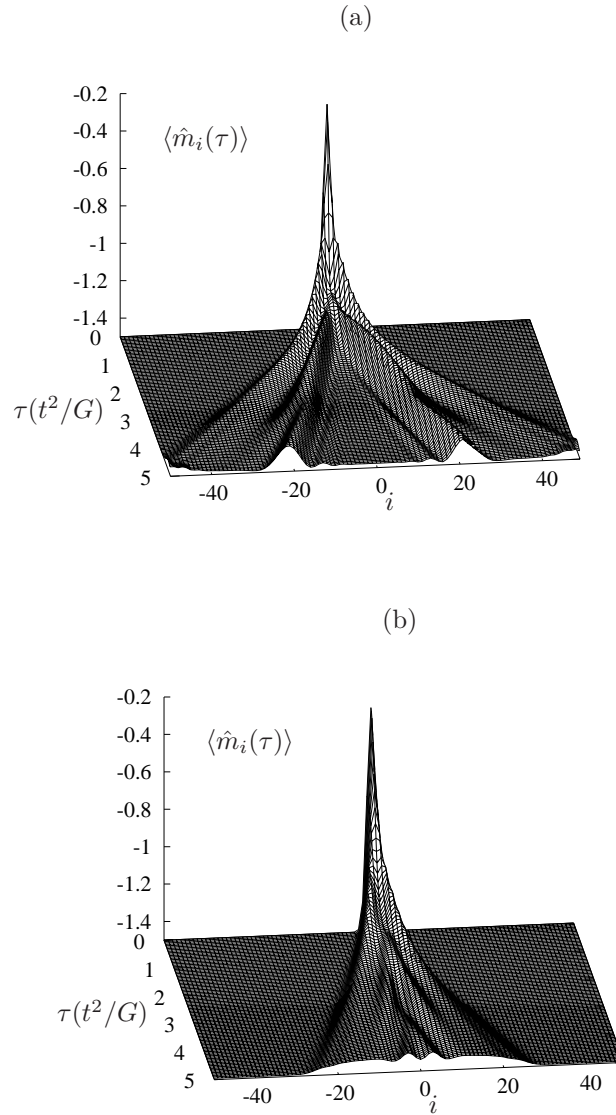


Figure IV.10: Time evolution of the local magnetization when the initial flip is spatially localized. The system parameters are  $qt^2/G = -4$  and  $L = 100$ . (a)  $g = 0.8G$  where the two bands are completely separated and thus defined wave packets can be seen. (b)  $g = -0.5G$  where one of the bands immerses into the biexciton sea. In the latter case, no defined wave packet is seen.

first time unit, there is a small population loss in

$$(IV.32) \quad N_{\frac{3}{2}}(\tau) = \sum_k |\langle k, \frac{3}{2} | k, \frac{3}{2} \rangle_\tau|^2,$$

of about 4% due to the projection into the bound states  $|\phi_k^\pm\rangle$  and 1% into the unbounded sea. Thereafter, no further considerable loss is observed since in

the 4 consequent time units only up to 1% is missing (the relevant time unit is the given by the inverse of the super-exchange coupling  $t^2/G$ ). This shows that inelastic exciton-exciton collisions are very inefficient when the exciton lays on its stable regime, i.e. the white regions of Fig. IV.6. Hence, multiple spin-flip excitations lead to an out-of-equilibrium highly-metastable many body state. The system, thus, may be understood as a basically stable gas of composites, that are actually excitons with a “biexciton dressing”, opening interesting perspectives for quantum composite gases. As an example, note that although the excitons present an effective nearest neighbor attraction with strength  $-2c_{3/2}$ , this interaction becomes irrelevant at low momenta  $k \rightarrow 0$  compared to the infinite on-site repulsion due to Pauli exclusion principle. Therefore, the low momentum properties of the 1D excitons will be as those of a Tonks-Girardeau gas.

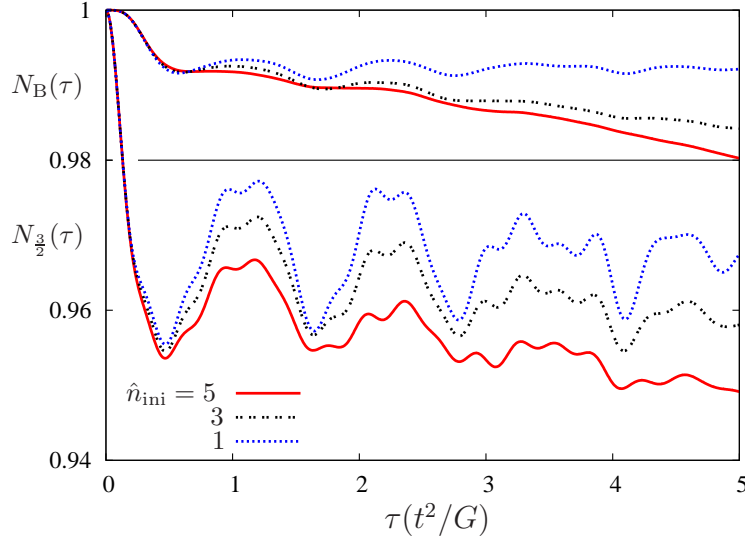


Figure IV.11: Time evolution of the number of excitons. Lower panel  $N_{\frac{3}{2}}(\tau)$  and upper panel  $N_B(\tau) = N_{\frac{3}{2}}(\tau) + \sum_k |\langle k_0^A | k_0^A \rangle_\tau|^2$ , both with  $t = 0.1G$ ,  $g = 0.6$ ,  $qt^2/G = -4$  and  $L = 30$ , for the case of 1 (dotted), 3 (dashed) and 5 (solid) spin flips non-localized on a initial square wave-packet of 10 sites wide.

Apart of the losses of the population, one can see oscillations on top of its average value. This Rabi-like oscillations come from the presence of the two bounded states  $|\phi_k^\pm\rangle$  and their coupling. The amplitude of such oscillation is considerably small since, as discussed in the previous section, when the system is spatially non-localized and  $k = 0$  the main contribution to the bound states comes from the exciton. However, those oscillations are clearly damped due to the presence of different momenta with, of course, different Rabi frequencies. When more oscillations contribute, the damping is accordingly increased. This effect is visible when rising the number of initial spin-flip excitations.



# PART C

## GROUND-STATE PHASES OF SPINOR LATTICE GASES



## Mott phases of hard-core spin-3/2 fermions in 1D optical lattices

In this chapter we concentrate on the influence of the quadratic Zeeman effect on the Mott-insulator phases of hard-core 1D spin-3/2 fermions. A  $SU(2) \otimes SU(2)$  symmetry leads for a large enough QZE to an isotropic pseudospin-1/2 Heisenberg anti-ferromagnet. When the QZE is reduced, the system undergoes a phase transition into a gapped dimerized phase through a Kosterlitz-Thouless transition. In order to determine this phase boundary, we make use of the level spectroscopy method. The infinite system size scaling gives information about the universality class of such phase transition.

### V.1 Spin chains

The analysis of spin chains and in general, spin lattices, constitutes the core of the quantum magnetism theory. The best known Hamiltonian describing a spin lattice is the so-called Heisenberg Hamiltonian

$$(V.1) \quad \hat{H}_H = \sum_{\langle ij \rangle} J_{ij} \vec{S}_i \cdot \vec{S}_j,$$

where the sign of  $J_{ij}$  defines the favorable alignment of the pair of spins at  $i$  and  $j$ . In the case of  $J_{ij} > 0$ , the energy of the system is reduced when the corresponding spins are anti-parallel and the exchange is anti-ferromagnetic. The ferromagnetic case occurs when  $J_{ij} < 0$  and the spins tend to remain parallel. This basic Hamiltonian may be effectively obtained for the case of spin-1/2 fermions within the Mott insulator phase. We would like to note that such Mott insulators of spin-1/2 fermions have recently been achieved in pioneering experiments<sup>[70,71]</sup>.

Super-exchange (i.e. second order) processes lead to an effective Heisenberg model with  $J_{ij} = t^2/U$ , where  $t$  is the hopping rate and  $U$  denotes on-site interactions. As a consequence, the system favors an anti-ferromagnetic Néel

ordering in 3D lattices. The anti-ferromagnetic nature of the coupling results from the fermionic nature of the particles, since two parallel spins cannot lower the energy via virtual hopping because they cannot occupy the same site.

We would like to note that, although, as mentioned above, Mott insulators have been observed in spin-1/2 fermions, current experiments are still over the entropies necessary to observe Néel ordering ( $\sim 0.35k_B$  per particle)<sup>[134]</sup>. The analysis of novel cooling techniques towards these temperatures constitute nowadays a very active research field<sup>[106,134–137]</sup>.

In this chapter we are interested in the magnetic properties of spin-3/2 fermions. As already mentioned in previous chapters, spin-3/2 fermions constitute the lowest spin fermionic system with spin-changing collisions in the hard-core regime. Moreover the QZE, contrary to the case of spin-1/2 systems, cannot be neglected, as has been shown in experiments on spinor BECs<sup>[72,73,76,112,113]</sup>. In spite of that, the effects of QZE on the magnetic properties of spin-3/2 fermions have not been considered in the literature up to now.

## V.2 Phase diagram of spin-3/2 fermions in 1D optical lattices at quarter filling

Before entering into the full detail of the problem we want to focus on, let us establish a framework by considering the general Hamiltonian from Eq. (III.14), that describes a fermionic gas of spin-3/2 particles loaded into a 1D optical lattice. We set  $q = 0$  and impose quarter filling, or in other words, we consider in average one particle per site. Although the system seems to be quite restricted, it still shows a rich physics reflected in the magnetic properties of the ground state when the two parameters,  $g_2$  and  $g_0$ , are scanned. Figure V.1 depicts the corresponding phase diagram<sup>[110,138]</sup>.

The phase diagram is characterized by several phases. For  $g > 0$  and  $g_2 \geq g_0$ , the system is a gapless spin liquid with 3 gapless spin-modes. This phase thus includes the SU(4) line  $g_0 = g_2$  whose exact solution was retrieved by Bethe-ansatz<sup>[118]</sup>. On this line, the manifold of spin $\pm 1/2$  and the one for spin $\pm 3/2$  coexist but are independent. The addition of a QZE is equivalent to two chemical potentials corresponding to each manifold. In this way, the system can be considered as a two band model where only one manifold survives for  $|q| > 2Gt^2 \ln 2$ <sup>[139]</sup>.

For  $g_2 < 0$  and  $|g_2|$  large enough, the attractive interactions will force the four components to cluster all together in a quartet forming a charge density wave. However, for  $g_0 > 0$  the repulsion along the  $F = 0$  channel splits the quartets apart occupying thus two sites, without vanishing the cluster correlation. Thus, the system goes from a quarter Cooper to a Quartet superfluid.

Finally the last region is characterized by the formation of singlet pairs.

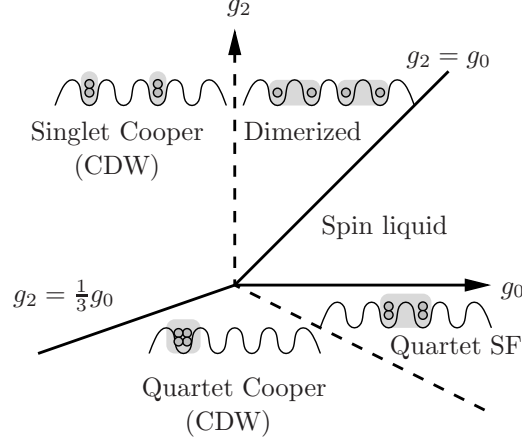


Figure V.1: Ground state phase diagram for a fermionic spin-3/2 gas loaded into a 1D optical lattice at quarter filling. The solid lines separate the three present phases, namely the spin liquid, quarteting and a dimerized phase. The two later present internal domains. When  $g_0 > 0$  the dimers occupy two sites as well as the quartet Cooper.

When  $g_0 < 0$  the involved particles live on a single site and the charge density wave structure is observed. This singlet Cooper pairs are again split into two sites when the  $F = 0$  channel becomes repulsive and the dimerization of spin Peierls order is reached. The latest phase is characterized by a long range order given by

$$(V.2) \quad \lim_{n \rightarrow \infty} \langle \hat{D}_i \hat{D}_{i+n} \rangle = f_0, \quad \text{with} \quad \hat{D}_i = (-1)^i \hat{S}_i (\hat{S}_{i-1} - \hat{S}_{i+1}).$$

where  $f_0$  is a finite value. By increasing  $g_0$  while keeping  $g_2$  constant, we end up again at the spin liquid phase through a Kosterlitz-Thouless-like transition at  $g_2 = g_0$  ( $g = 0$ ).

### V.3 1D Mott fermionic spin-3/2 effective Hamiltonian in the hard-core regime

Our starting point is the Hamiltonian given by the Eq. (III.23) and (III.24), that describes the effective Hamiltonian of spin-3/2 fermion gas loaded into an deep enough optical lattice. We also considered a chemical potential and a small enough hopping such that the system shows a MI phase with just one particle per site. In this case, the charge is fixed and the magnetic structure of the gas depends only on the spin. Thus, we recall the Hamiltonian

$$(V.3) \quad \hat{H}_{\text{eff}} = \sum_i \hat{H}_{i,i+1} + q \sum_{i,m} m^2 \hat{n}_{m,i},$$

where

$$\begin{aligned}
\hat{H}_{i,j} = & c_2 \sum_{|m| \neq |m'|} \left[ \hat{n}_{m,i} \hat{n}_{m',j} - \hat{\psi}_{m,i}^\dagger \hat{\psi}_{m',j}^\dagger \hat{\psi}_{m,j} \hat{\psi}_{m',i} \right] \\
& + \sum_{|m|=\frac{1}{2}}^{\frac{3}{2}} c_{|m|} \left[ \hat{n}_{m,i} \hat{n}_{-m,j} - \hat{\psi}_{m,i}^\dagger \hat{\psi}_{-m,j}^\dagger \hat{\psi}_{m,j} \hat{\psi}_{-m,i} \right] \\
& + c_{\text{sc}} \left\{ \left[ \hat{\psi}_{-\frac{1}{2},i}^\dagger \hat{\psi}_{\frac{1}{2},j}^\dagger - \hat{\psi}_{\frac{1}{2},i}^\dagger \hat{\psi}_{-\frac{1}{2},j}^\dagger \right] \left[ \hat{\psi}_{\frac{3}{2},i} \hat{\psi}_{-\frac{3}{2},j} - \hat{\psi}_{-\frac{3}{2},i} \hat{\psi}_{\frac{3}{2},j} \right] + \text{h.c.} \right\}.
\end{aligned}
\tag{V.4}$$

and

$$c_{3/2} = 2t^2 \left[ \frac{\cos^2 \theta}{\frac{9}{2}q - \lambda_+} + \frac{\sin^2 \theta}{\frac{9}{2}q - \lambda_-} \right], \tag{V.5}$$

$$c_{1/2} = 2t^2 \left[ \frac{\cos^2 \theta}{\frac{1}{2}q - \lambda_-} + \frac{\sin^2 \theta}{\frac{1}{2}q - \lambda_+} \right], \tag{V.6}$$

$$c_2 = -\frac{2t^2}{g+1}, \tag{V.7}$$

$$c_{\text{sc}} = 2 \sin \theta \cos \theta \left[ \frac{\frac{5}{2}q - \lambda_+}{(\frac{1}{2}q - \lambda_+)(\frac{9}{2}q - \lambda_+)} - \frac{\frac{5}{2}q - \lambda_-}{(\frac{1}{2}q - \lambda_-)(\frac{9}{2}q - \lambda_-)} \right]. \tag{V.8}$$

with  $\lambda_{\pm} = 1 + \frac{5}{2}q \pm \sqrt{4q^2 + g^2}$ ,  $\tan \theta = (2q + \sqrt{4q^2 + g^2})/g$ . We consider in detail the case  $g > 0$  where the dimerized (spin-Peierls) phase is localized for small enough  $q$ <sup>[140]</sup>. The nature and the characteristics of the  $g < 0$  phases lie out of the scope of this Thesis (see PhD Thesis of K. Rodríguez<sup>[141]</sup>).

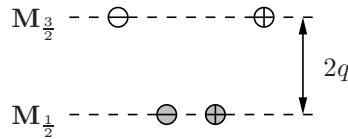


Figure V.2: Scheme of the separation of the two present pseudospin-1/2 manifolds in the spin-3/2 system when the QZE is added.

### Limit of $|q| \rightarrow \infty$ : pseudospin-1/2 IHAFM

In this extreme case, the manifold of  $m = \pm 1/2$ ,  $\mathbf{M}_{\frac{1}{2}}$ , and  $m = \pm 3/2$ ,  $\mathbf{M}_{\frac{3}{2}}$ , are completely separated by an energy difference much larger than the coupling term between them  $c_{\text{sc}}$ , as shown in Fig. V.2. Therefore, an underlying Hamiltonian can be calculated in order to observe the spectral properties of

the system in that limit. Then, the Hamiltonian  $\hat{H}_{i,j}$  on the manifold  $\mathbf{M}_m$  reads,

$$(V.9) \quad \hat{H}_{i,j} = c_m \left[ \hat{n}_{m,i} \hat{n}_{-m,j} - \hat{\psi}_{m,i}^\dagger \hat{\psi}_{-m,j}^\dagger \hat{\psi}_{m,j} \hat{\psi}_{-m,i} \right],$$

whereas the QZE term becomes the constant  $E_q = qLm^2$ . For  $q > 0$  we end up in the manifold  $\mathbf{M}_{\frac{1}{2}}$  and for  $q < 0$ , in  $\mathbf{M}_{\frac{3}{2}}$ . With the help of the pseudospin-1/2 operators

$$(V.10) \quad \check{S}_i^{z[m]} = \hat{n}_{m,i} - \hat{n}_{-m,i},$$

$$(V.11) \quad \check{S}_i^{+[m]} = \hat{\psi}_{m,i}^\dagger \hat{\psi}_{-m,i},$$

$$(V.12) \quad \check{S}_i^{-[m]} = \hat{\psi}_{-m,i}^\dagger \hat{\psi}_{m,i};$$

it is possible to construct a more intuitive expression for the underlying Hamiltonian. So we have,

$$(V.13) \quad \hat{H}_{\text{eff}}^{[m](0)} = -2c_m \sum_i \left[ \check{S}_i^{[m]} \cdot \check{S}_{i+1}^{[m]} - \frac{1}{4} \hat{I}_{i,j} \right] + E_q.$$

where, in this limit the coefficient takes the value

$$(V.14) \quad \lim_{q \rightarrow \pm\infty} -2c_m = 4t^2 > 0,$$

showing that the system projects into a pseudospin-1/2 isotropic Heisenberg anti-ferromagnet.

### Case of $|q| \gg c_{\text{sc}}$ : $J_1 - J_2$ model

Since the SCC takes states out and into the considered manifold  $\mathbf{M}_m$ , Van-Vleck perturbation theory allows us to analyze the behavior of the system for large but finite QZE. Up to second order in  $c_{\text{sc}}$ , we reach the IHAFM Hamiltonian

$$(V.15) \quad \hat{H}_{\text{eff}}^{[\frac{1}{2}](2)} \approx -2 \left( c_{1/2} + \frac{2c_{\text{sc}}}{c_{1/2} - c_{3/2} - 2q} \right) \sum_i \left[ \check{S}_i^{[m]} \cdot \check{S}_{i+1}^{[m]} - \frac{1}{4} \hat{I}_{i,j} \right],$$

where the constant  $E_q$  has been ignored. An analogous situation is given for  $m = 3/2$ .

Due to the anti-ferromagnetic interactions, one expects the ground state to show an anti-parallel ordering in the spins and thus a vanishing total magnetization,  $\mathcal{M}^{[m]} = \sum_i \langle \check{S}_i^{z[m]} \rangle = 0$ . The first excited state on top of this singlet is given by an spin flip, and has hence spin 1. Thus, this state is a degenerated triplet. This is important for the spectroscopy calculation shown below.

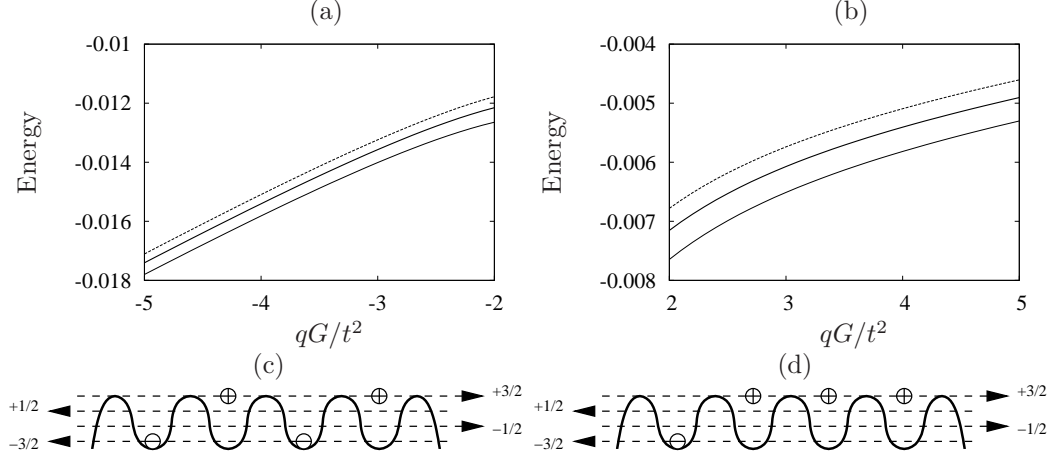


Figure V.3: Energy spectrum of the IHAFM for large (a)  $q < 0$  and (b)  $q > 0$ . The solid thin line is the ground state which is a singlet with  $\mathcal{M}^{[m]} = 0$ , the thick line is the triplet set of first excited states and the dashed line is the second excited state. (b) and (c) are classical cartoons of both the ground and the first excited states when  $\mathbf{M}_{\frac{3}{2}}$  is favored.

In Fig. V.3 the spectrum of the Hamiltonian V.15 is shown for both limiting cases (a) negative and (b) positive QZE. Moreover, an sketch of the ground and first excited states is also presented in panels (c) and (d) respectively, from a classical point of view.

If we go further in perturbation theory, we end up with an anti-ferromagnetic Hamiltonian with next-nearest neighbor exchange:

$$(V.16) \quad \hat{H}_{\text{eff}}^{[m](3)} \approx \sum_i \left[ J_1 \vec{S}_i^{[m]} \cdot \vec{S}_{i+1}^{[m]} + J_2 \vec{S}_i^{[m]} \cdot \vec{S}_{i+2}^{[m]} + q \left( \tilde{S}_i^{z[m]} \right)^2 \right].$$

This model, the frustrated  $J_1 - J_2$  spin-1/2 anti-ferromagnetic chain, presents a KT phase transition at  $J_1(g, q)/J_2(g, q) \approx 4$ <sup>[142]</sup>. This is the first indicator that a phase transition is present on the spin-3/2 system and gives a hint that the universality class of such transition. However, numerical calculations considering all four components must be performed to confirm this conjecture. Note that Eq. (V.16) maintains a rotational symmetry. This isotropy is kept in any order of perturbation theory, being the result of a hidden  $SU(2) \otimes SU(2)$  symmetry, which in turn results from the  $SO(5)$  symmetry of the Hamiltonian



with  $q = 0$ <sup>[110]</sup>. The SU(2)generators for each manifold  $\mathbf{M}_{\frac{3}{2}}$  and  $\mathbf{M}_{\frac{1}{2}}$  are

$$(V.17) \quad \check{S}^z[m] = \frac{1}{2} \sum_i \check{S}_i^{z[m]},$$

$$(V.18) \quad \check{S}^+[m] = \sum_i \check{S}_i^{+[m]},$$

$$(V.19) \quad \check{S}^-[m] = \sum_i \check{S}_i^{-[m]},$$

## V.4 Level spectroscopy.

The Kosterlitz-Thouless phase transition is an infinite order one. This means that it is not possible to discern it from the ground state behavior. However, in a case like the system we are studying, the structure of the spectrum is different at each side of the transition. On the IHAFM, we already analyzed the low energy spectrum getting a sole ground state with zero magnetization and a three-fold degenerate first excited state with  $\mathcal{M} = 0, \pm 1$ .

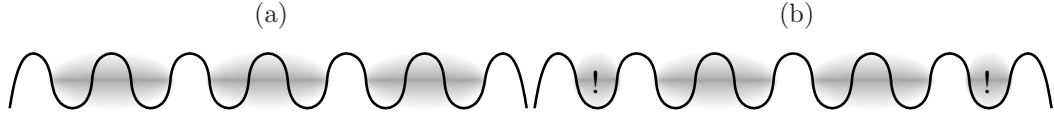


Figure V.4: Cartoon picture of the main structure of the spin Peierls state. Two consecutive spins associate and the spatial symmetry is broken (a). For final systems one of the two possible associations is not longer the ground state (b).

For  $q = 0$ , it is known that the system presents a dimerized (spin Peierls) state<sup>[110]</sup>, as we discussed above. This state breaks the translational symmetry by one site but still has a translation symmetry every 2 sites. Therefore, in the thermodynamic limit, the ground state is two-fold degenerate. Nonetheless, for finite systems this degeneracy is lifted with an exponentially small gap in the system size. Thus, the first excited and the ground state are both singlets with total magnetization  $\mathcal{M} = 0$ . Figure V.4 depicts a classical sketch of the dimerized phase.

We hence know that the first excited state within the dimerized region is a singlet with total magnetization zero, while on the IHAFM we have a triplet with total spin one. Since the Hamiltonian preserves the total magnetization,  $[\hat{H}_{\text{eff}}, \hat{\mathcal{M}}] = 0$ , the levels can only lie on a given subspace and thus a level crossing should be observed, as in Fig. V.5. The point where the level crossing is found provides the phase transition boundary for a given system size  $L$ . Afterwards, a finite-size scaling is used to determine the phase transition line in the thermodynamic limit.

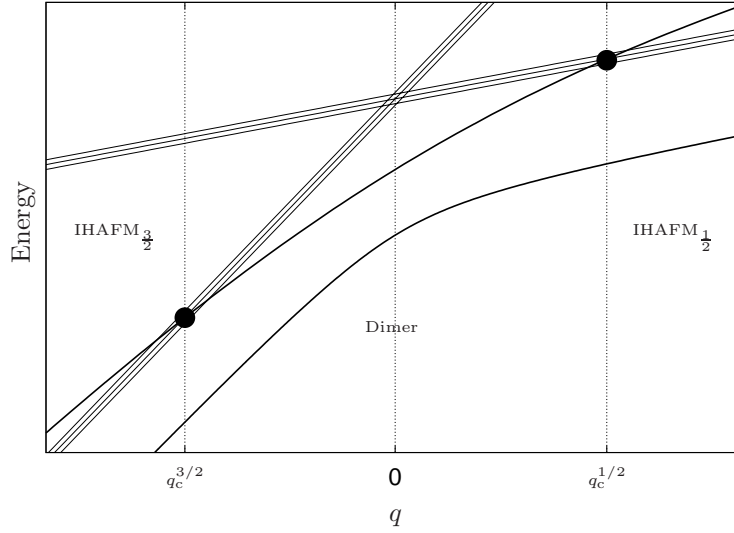


Figure V.5: Expected behavior of the system spectrum for given  $g$  when scanning  $q$ . In the two extremes the first excited state is a triplet while in the neighbor of  $q = 0$  it is a singlet. Since the KT transition has infinite order, the ground energy is smooth and shows no evidence of it.

Numerically speaking, the system under consideration has a huge dimension,  $\dim(\hat{H}_{\text{eff}}) = 4^L$ . However, the Hamiltonian is described by a sparse matrix and thus the Lanczos method is suitable (for details see chapter VII). Furthermore, we can consider only the manifolds of total magnetization  $\mathcal{M} = 0$  and  $\mathcal{M} = 1$ . This reduces the dimension of the numerical system notoriously allowing us to explore larger systems. For instance for  $L = 10$ , the original matrix size is  $4^{10} = 1048576 \approx 10^6$ , but on the manifolds we have dimensions  $\dim(\mathcal{M} = 0) = 116304$  and  $\dim(\mathcal{M} = 1) = 112035$ , which is about 10% of the total. Moreover, since the system has a  $SU(2) \otimes SU(2)$  symmetry the necessary system dimension can be further reduced. In particular, for the example above we have  $\dim(\hat{H}_{\text{eff}}; \mathcal{M} = 0, \tilde{S}^z = 0) = 63504$ . That is about 5% of the initial dimension. More intricate methods for further reduction may be applied, such as momentum conservation. However, they are time consuming and therefore not always optimal.

The numerical results of the level crossing are depicted in Fig. V.6(a) for several system sizes. Since the system behaves symmetrically with respect of  $q$ , we considered here only  $q < 0$  that favors the manifold  $\mathbf{M}_{\frac{3}{2}}$ . In order to calculate the boundary between the phases we scan the spectrum of the system for several values of the SCC parameter  $g$ . The triplet-singlet level crossing spots the phase transition point  $q_c^{3/2}(g)$  for this particular value of  $g$ . However, the numerical results are performed for finite systems with periodic boundary conditions and since we are interested in the thermodynamic limit of the phase boundaries a finite size scaling is needed. The scaling shows not

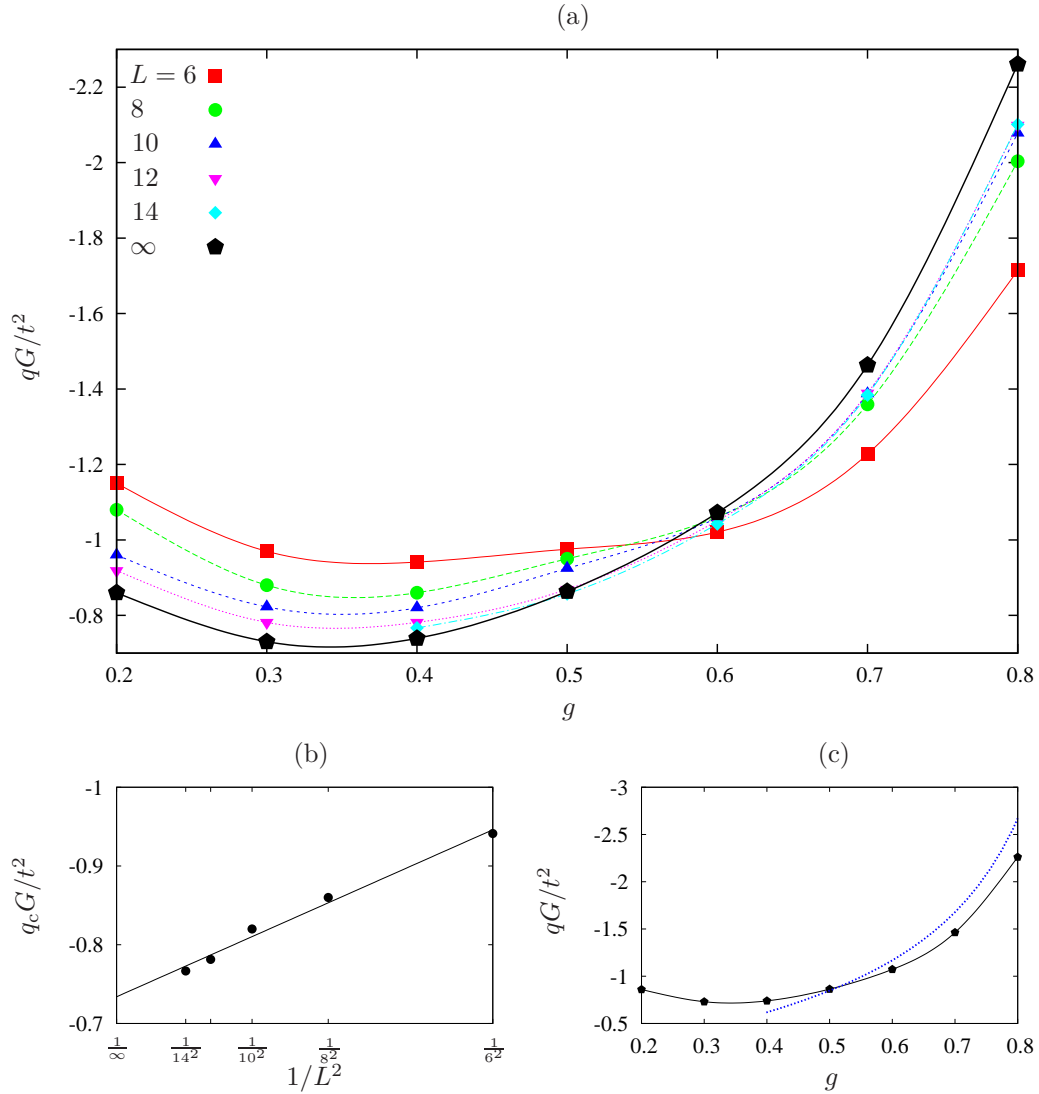


Figure V.6: Phase transition boundary. (a) The boundary for several system sizes. The finite size scaling at  $g = 0.5$  in (b) reveals the expected  $q_c(g)$  in the thermodynamic limit. In (c), comparison between the Lanczos results and the  $J_1 - J_2$  model from Eq. V.16.

only information about the boundary for  $L \rightarrow \infty$  but also the universality class of the phase transition. As shown in the panel (b) of the figure, a fitting of  $1/L^2$  is suitable to describe the boundary tendency when increasing the system size. Hence, this confirms a Kosterlitz-Thouless-like class for the aforementioned phase transition<sup>[143]</sup>.

Finally the panel (c) shows a comparison between the Lanczos procedure and the results from the  $J_1 - J_2$  model with third order perturbation theory described by Eq. (V.16). For the later, the coefficients  $J_1$  and  $J_2$  were numerically computed and we plot the curve corresponding to the coefficients ratio  $J_1/J_2 = 4$ . Those curves present a good agreement for  $g > 0.4$ .

On the other hand, for  $g \ll 1$  the finite size effects are strong and the scaling is non-reliable. This comes from the fact that the gap reduces exponentially for small enough values of the SCC and thus, at some point, it becomes numerically zero closing at the same time the possibility of spectral analysis. In particular for the extreme of  $g = 0$  the physics changes radically. On this line, the system becomes exactly solvable<sup>[118]</sup>, being characterized by a commensurate-incommensurate transition as discussed below.

From the behavior of the system in perturbation theory, a rich physics is expected in more general potential topologies like ladders and square lattices. In the case of ladders, an Ising phase transition from a rung-singlet to a columnar dimer with increasing frustration is expected<sup>[144]</sup>, due to the terms that induce frustration in the diagonal exchange. For square lattices a possible second order phase transition showing deconfined criticality is present when going from the Néel state to a spin disordered state because of the the third neighbor exchanges.

## V.5 Complete phase diagram

As we discussed in section V.2, two phases are present in the Mott regime at quarter filling of fermionic spin-3/2 gases loaded in 1D optical lattices. They are the dimerized phase and the spin liquid phase. For  $q = 0$  a Kosterlitz-Thouless phase transition takes place between them at  $g = 0$ . As shown above, the physics gets richer when the quadratic Zeeman coupling is added<sup>[140,141]</sup>.

With the QZE, the  $g = 0$  point becomes a line, whose physics can be understood by means of a two-band model<sup>[139]</sup>, where atoms with  $m = \pm 1/2$  ( $\pm 3/2$ ) act as fermions at the lowest (second) band, and the QZE difference  $2q$  resembles the band gap. For  $\tilde{q} < \tilde{q}_{cr} \equiv 2 \ln 2 \simeq 1.386$  the magnetic order is suppressed due to “orbital” effects, and the system has three massless spinons. On the contrary for  $\tilde{q} > \tilde{q}_{cr}$  the “orbital” degeneracy is lifted, and the manifolds  $\pm 1/2$  and  $\pm 3/2$  completely decouple in the ground state. When this occurs,  $\tau = N_{\frac{3}{2}} + N_{-\frac{3}{2}} - N_{\frac{1}{2}} - N_{-\frac{1}{2}}$  saturates to 1, and the system reduces, as mentioned above, to a pseudo-spin-1/2 IHAFM with  $J = 4t2/G$ . Therefore at

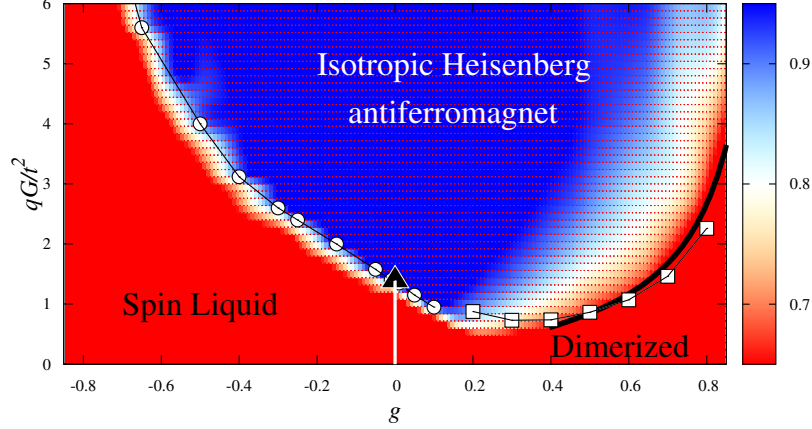


Figure V.7: Phase diagram for spin-3/2 fermions in a 1D optical lattice at quarter filling in the Mott regime and a quadratic Zeeman coupling. The density plot represents the chirality  $\tau$ , the squares plot the singlet-triplet crossing in the excitation spectrum, the circles the jump of the exponent  $\gamma$  to  $-1$  and the white curve the  $J/J_2 = 4$  line resulting from a strong-coupling analysis, and the sole triangle points the critical  $q_{cr}$  expected from two-band theory.

$\tilde{q}_{cr}$  there is PT from a gapless spin-liquid into a gapless AF pseudo-spin-1/2 chain. At the phase transition the exponent  $\gamma$  jumps to  $-1$ <sup>[139]</sup>. This point was calculated numerically using MPS retrieving the value  $\tilde{q} \simeq 1.35$ , in good agreement with the analytical result<sup>[140,141]</sup>. The numerical results are also consistent with  $1 - \tau \sim \sqrt{\tilde{q}_{cr} - \tilde{q}}$  when approaching the phase transition for growing  $q$ . Hence at  $g = 0$  and  $\tilde{q}_{cr}$  there is a commensurate-incommensurate transition between the two gapless phases<sup>[145]</sup>. Moreover,  $g = 0$  and  $\tilde{q}_{cr}$  is a multicritical point for three phases: spin-liquid, pseudo-spin-1/2 IHAFM, and the dimerized phase.

The  $g < 0$  case lies beyond the scope of this Thesis, however, further details can be seen in<sup>[140]</sup> and the PhD Thesis of K. Rodríguez<sup>[141]</sup>. The region  $g < 0$  smoothly connects with  $g = 0$  since perturbations from  $g = 0$  into  $g < 0$  are (marginally) irrelevant in the renormalization group (RG) sense<sup>[110]</sup> and the symmetry dynamically enlarges to  $SU(4)$ . One could hence expect that the  $g < 0$  region behaves similarly to the  $g = 0$  case for growing  $q$ . There is, however, an important distinction, since for  $g \neq 0$   $\tau$  is not a good quantum number, never saturating for finite  $q$ <sup>[146]</sup>. A plausible scenario for  $g \leq 0$  is that the QZE induces a commensurate-incommensurate phase transition, so that chirality-non-conserving processes remain irrelevant all the way, and do not modify the nature of the transition which takes place at  $g = 0$ . MPS calculations confirm this scenario<sup>[140,141]</sup>.



---

 AFM phases of spin-1 boson spin chains
 

---

We study the phase diagram of anti-ferromagnetic repulsively interacting spin-1 bosons in optical lattices at unit filling, showing that an externally induced quadratic Zeeman effect may lead to a rich physics characterized by various phases and phase transitions. Our work provides a quantitative guide for the experimental analysis of various types of field-induced quantum phase transitions in spin-1 lattice bosons. These transitions, which are precluded in spin-1/2 systems, may be realized using an externally modified quadratic Zeeman coupling, similar to recent experiments with spinor condensates in the continuum.

As shown in previous chapters, one of the features of the spin-3/2 system is the high symmetry it presents. In particular, when the QZE is considered, the splitting of the two manifolds  $\mathbf{M}_{\frac{1}{2}}$  and  $\mathbf{M}_{\frac{3}{2}}$  leads to a  $SU(2) \otimes SU(2)$  symmetry. This way, the system shows a behavior that depends only on the magnitude of the QZE  $|q|$ . Also, this symmetry was further exploited numerically for the reduction of the effective Hilbert space dimension.

A completely different situation is presented when spin-1 systems are considered. In this case the local magnetization takes the values  $m = \pm 1, 0$  and the corresponding manifolds  $\mathbf{M}_1$  and  $\mathbf{M}_0$  have distinct properties. Considering only  $\mathbf{M}_1$ , it resembles the case of pseudo-spin-1/2 bosons, whereas  $\mathbf{M}_0$  would be a spin-less boson system. This fact breaks the symmetry on the QZE and therefore a different behavior for  $q > 0$  and  $q < 0$  is expected. Therefore, three phases and two phase transitions are field-induced for anti-ferromagnetic interactions. As we show below, they are a Kosterlitz-Thouless transition from a  $XY$ -Nematic phase to a dimerized phase and an Ising transition from the dimerized phase to a Large- $D$  phase.

## VI.1 Effective Hamiltonian in absence of QZE

Our starting point is the case of  $q \equiv 0$ . Spin-1 gases are the simplest spinor system beyond the two-component ones. Depending on the inter-particle interaction, which is given itself by the  $s$ -wave scattering lengths  $a_{0,2}$ , the system presents either a ferromagnetic ( $a_0 > a_2$ ) or an anti-ferromagnetic ( $a_0 < a_2$ ) ground state. Experimentally, it is possible to reproduce both cases. For example, for the first,  $^{87}\text{Rb}$  in  $F = 1$  is ferromagnetic<sup>[147]</sup> while  $^{23}\text{Na}$  is anti-ferromagnetic (AFM)<sup>[90]</sup>. In the following we focus on the AFM case.

On the other hand, several studies have been done when the gas is loaded in an optical lattice. For instance, for the AFM a wealth of quantum phases have been predicted<sup>[148,149]</sup>. In particular for the relevant case of one-dimensional systems, which is our main focus, an important result is that the quantum fluctuations lead to a spontaneously dimerized ground state<sup>[150–157]</sup>. It is known that the specific case when  $a_0 = a_2$  has a highly degenerate ground state and an enlarged  $\text{SU}(3)$  symmetry<sup>[158]</sup>. Most of the spin-1 species have scattering lengths in the vicinity of this point, where small external perturbations may produce considerable effects by reducing the system symmetry and thus favoring specific phases.

The starting point of the analysis is the Hamiltonian that describes a spinful gas in an optical lattice when the charge degree of freedom is frozen. In particular, we focus on 1D lattices and  $S = 1$ . Thus we have

$$\begin{aligned}
 \hat{H}_S &= \sum_{n=1}^2 \sum_{\langle ij \rangle} J_{ij}(n) \left( \vec{\hat{S}}_i \cdot \vec{\hat{S}}_j \right)^n \\
 \text{(VI.1)} \quad &= J \sum_{i=1}^L \left[ \cos \theta \left( \vec{\hat{S}}_i \cdot \vec{\hat{S}}_{i+1} \right) + \sin \theta \left( \vec{\hat{S}}_i \cdot \vec{\hat{S}}_{i+1} \right)^2 \right],
 \end{aligned}$$

where  $J \equiv J(g_0, g_2)$  and  $\theta \equiv \theta(g_0, g_2)$  are elaborated functions of the interaction strengths as we will show below<sup>[159,160]</sup>. Thus, the properties of the ground state as well as the excitations are determined by  $\theta$  since  $J$  acts like an energy scale. The phase diagram is shown in Fig. VI.1.

The diagram is divided into the anti-ferromagnetic and the ferromagnetic domains. The latter is the case when  $\frac{\pi}{2} < \theta < \frac{5\pi}{4} \equiv -\frac{3\pi}{4}$  and in the figure it is dashed. The exactly solvable highly symmetric  $\text{SU}(3)$  point  $\theta = -\frac{3\pi}{4}$  marks the beginning of the anti-ferromagnetic region<sup>[159]</sup>. The repulsive interaction interval expands from it till another exactly solvable point at  $\theta = -\pi/2$ , the Klumper-Barber-Batchelor (KBB) point<sup>[161,162]</sup>. This is our region of interest when the QZE is added and thus it is shaded in the figure. We just consider these regions because they are easily accessible using spin-1 bosons in optical lattices. We note, however that more elaborate ideas, although quite involved experimentally, may allow for the observations of all gapped phases in Fig. VI.1<sup>[159]</sup>.



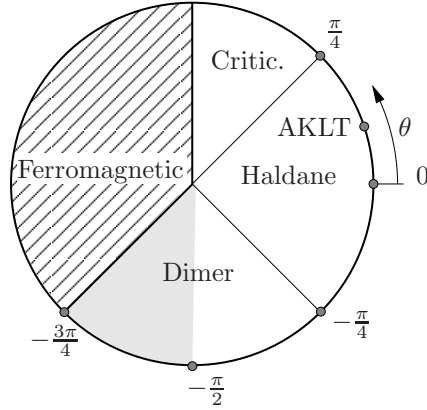


Figure VI.1: Spin-1 MI ground-state phase diagram with no external fields. The exactly solvable points are:  $\theta = \pi/4$  the Uimin-Lai-Sutherland point,  $\tan \theta = 1/3$  the Affleck-Kennedy-Lieb-Tasaki (AKLT) point,  $\theta = -\pi/4$  the Takhtajan-Babujan point,  $\theta = -\pi/2$  the Klumper-Barber-Batchelor point and  $\theta = -3\pi/4$  the highly symmetric SU(3) point.

The dimer phase continues up to the Takhtajan-Babujan critical point<sup>[163,164]</sup>,  $\theta = -\pi/4$ , where a second-order phase transition takes place into the Haldane region. Within this region two important points should be highlighted. First the Heisenberg point at  $\theta = 0$  and the Affleck-Kennedy-Lieb-Tasaki (AKLT) point which is described with an exact valence bound wave function<sup>[165]</sup>. Finally, at the Uimin-Lai-Sutherland critical point<sup>[118]</sup>,  $\theta = \pi/4$ , a phase transition occurs into a gapless phase.

As for the spin-3/2 case, the interactions preserve magnetization,  $\mathcal{M}$ , and hence the linear Zeeman effect may be gauged out, note however that the specific phase diagram depends on  $\mathcal{M}$ <sup>[166]</sup>. Contrary to that, the QZE plays a crucial role in spinor gases, but its effects have been barely explored. The only contribution, including this coupling, has been done with a mean-field treatment in 3D. It shows that for a finite magnetization, the coupling leads to a nematic-ferromagnetic (or partially magnetic) transition<sup>[167]</sup>.

## VI.2 System with QZE

Let us now focus on the specifics of the problem we want to work in. We consider a repulsively interacting ultracold spin-1 bosons in a 1D optical lattice prepared in a balanced mixture of zero total magnetization,  $\mathcal{M} = 0$ . Analogously, the interactions are characterized by the coupling constants  $g_{0,2}$  defined as in Eq. (III.3). At integer filling, the system is in the MI regime when the interaction constants fulfill  $g_{0,2} \ll t$ . Using, as in the previous chapter, the Van-Vleck effective theory up to second order, the effective Hamiltonian

of the system is given by the normalized bilinear-biquadratic spin expression

$$(VI.2) \quad \hat{H}_{\text{eff}} = \sum_i \left[ \cos \theta \left( \vec{\hat{S}}_i \cdot \vec{\hat{S}}_{i+1} \right) + \sin \theta \left( \vec{\hat{S}}_i \cdot \vec{\hat{S}}_{i+1} \right)^2 - D \left( \hat{S}_i^z \right)^2 \right];$$

where

$$(VI.3) \quad \tan \theta = \frac{g_0 + 2g_2}{3g_0},$$

$$(VI.4) \quad D = q \frac{3g_0g_2}{2t^2 \sqrt{2(5g_0^2 + 2g_0g_2 + 2g_2^2)}}.$$

The AFM regime with repulsive interactions belongs to the interval  $-\frac{3}{4}\pi < \theta < -\frac{1}{2}\pi$ , where the dominant correlations are of spin-nematic (quadrupolar) type<sup>[156,168]</sup>.

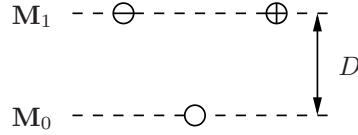


Figure VI.2: Scheme of the separation of the two manifolds in the spin-1 system when the QZE is added.

For large enough values of  $|D|$  two manifolds split, namely the  $\mathbf{M}_1$  with a pseudospin-1/2 character and  $\mathbf{M}_0$  with a spinless-like character. An scheme of the splitting is presented in Fig. VI.2. Depending on the sign of the QZE parameter either of them is favored.

### VI.2.a *XY-Nematic to dimerized phase transition*

Let us consider the case of  $D > 0$ . Here, the  $m = \pm 1$  components are favored and the ground state would lay on the corresponding manifold  $\mathbf{M}_1$ . The ground state on this manifold is clearly different from the dimerized one and thus a phase transition is expected between them.

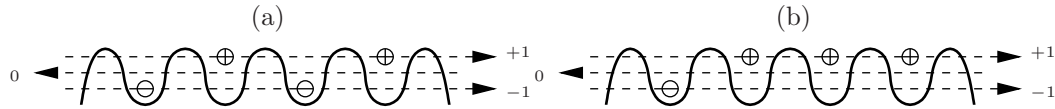


Figure VI.3: (a) Cartoon of the ground state in the *XY-Nematic* and (b) the first excited state with clear total magnetization  $\mathcal{M} = 2$ .

Following the level crossing procedure used in the previous chapter, we first have to establish the individual low energy excitations present on each phase.

In the thermodynamic limit the dimerized phase has a two-fold degenerate ground state. When the system is reduced to a finite size, this degeneracy is lifted and a gap opens. Therefore, the ground and the first excited states have a vanishing total magnetization. On the other hand for large  $D > 0$ , the anti-ferromagnetic interaction on the manifold  $\mathbf{M}_1$  will structure the system in such way that the ground state has total magnetization zero as well, but the first excited state would have a magnetization of  $\mathcal{M} = \pm 2$  as depicted in Fig. VI.3. The point where this two phases coexist  $D_c^+$  lays on the dimer upper phase boundary for a given system size  $L$ .

The most efficient way to calculate numerically the level crossing, is to calculate the low energy spectrum of the system for several sizes with the Lanczos method. After that, the thermodynamic limit boundary can be estimated with the proper finite size scaling. The main challenge for the method is the huge Hilbert space dimension involved in the calculation. However, we can restrict ourselves to the different magnetization manifolds since  $[\hat{H}_{\text{eff}}, \hat{\mathcal{M}}] \equiv 0$ . Under this constrain, we reduce the matrix size from  $3^L$  to

$$(VI.5) \quad \dim(\mathcal{M} = 0) = \sum_{n=0}^{L/2} \frac{L!}{(L-2n)!n!n!},$$

when considering the zero magnetization manifold. As an example, let us take  $L = 14$ . That implies a Hilbert dimension of  $\dim(\hat{H}_{\text{eff}}) = 4^{14} = 268435456 \approx 2.7 \times 10^8$ . However, we only require a vector with dimension  $\dim(\mathcal{M} = 0) = 616227$  to fully describe the ground state, which means that only 0.3% is indeed necessary. Furthermore, for the  $XY$ -Nematic phase, only the manifold of  $\mathcal{M} = 2$  is relevant which is even smaller with dimension

$$(VI.6) \quad \dim(\mathcal{M} = 2) = \sum_{n=0}^{L/2} \frac{L!}{(L-2n-2)!n!(n+2)!},$$

that for the case of  $L = 14$  takes the value  $\dim(\mathcal{M} = 2) = 502593$ .

The results of the numerical calculation for the level crossing are plotted in Fig. VI.4, where a scan on the  $\theta$  interval was performed. In this way, the curve  $D_c^+(\theta; L)$  is retrieved for each computationally accessible system size. Then, it is possible to evaluate the infinite system limit for each value of  $\theta$  by fitting the behavior of the crossing point. An excellent agreement with an inverse quadratic behavior of  $L$  is observed. This highlights the universality class of the phase transition setting it as one of the Kosterlitz-Thouless type.

One of the features of the phase transition line  $D_c^+(\theta)$  is that it closes when  $\theta \rightarrow \theta_{\text{SU}(3)} = -\frac{3}{4}\pi$ . In the vicinity of this point, the gap between the ground and first excited state in the dimer region is numerically speaking zero, and therefore the level crossing cannot be discerned. However, the exponential reduction of this gap and the universality class of the phase transition can be

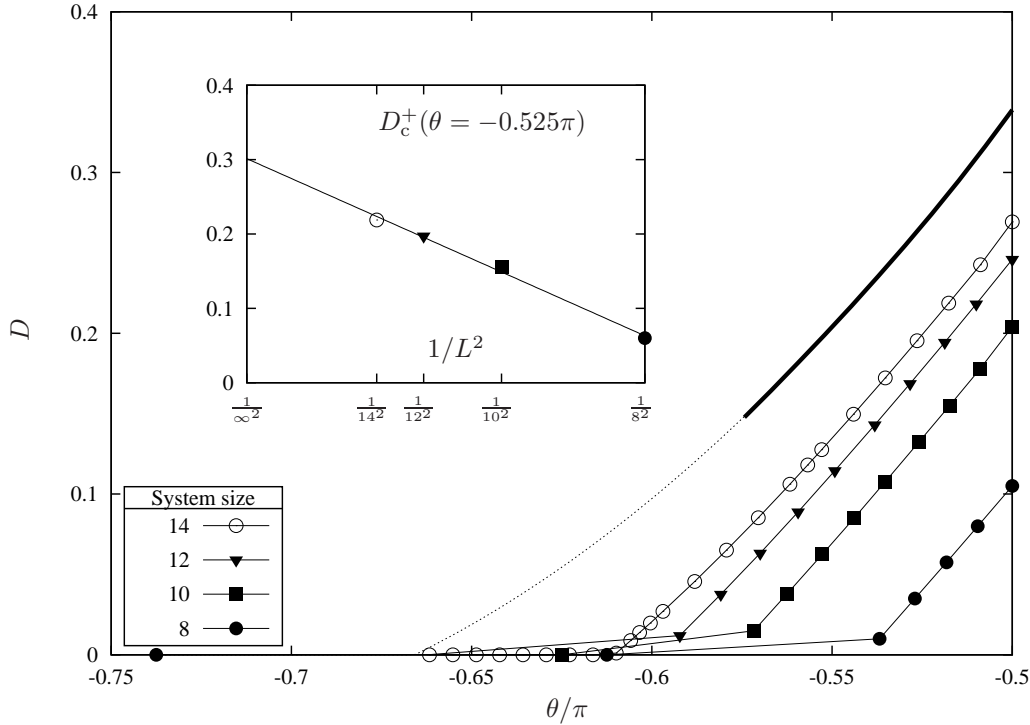


Figure VI.4: Numerical results of the level crossing by Lanczos diagonalization for several system sizes. The expected boundary in the thermodynamic limit is given by the function  $D_c^+(\theta)$  shown as a thick line. The inner panel shows the excellent fitting of the finite size scaling in  $1/L^2$  for a particular value of  $\theta$ .

predicted by means of a low-energy effective field theory around the highly symmetric point  $\theta_{\text{SU}(3)}$ <sup>[169]</sup>. The numerical results are thus consistent with that picture showing the robustness of the treatment.

## VI.2.b Large- $D$ to dimerized phase transition

In strong contrast to the spin-3/2 case, for spin-1 chains with QZE, the symmetry on the sign of it is broken. When  $D < 0$ , *only* one component is favored, as can be seen in Fig. VI.2. This changes the physics of the underlying system. We already know that for  $D = 0$  the ground state presents a dimerized phase. On the other extreme, for large enough  $|D| \gg 1$  but  $D < 0$ , the system undergoes a transition towards a state with absolutely no  $m = \pm 1$  components so-called the *large- $D$*  phase or *polar phase*.

The ground state goes smoothly from a state composed only by  $m = 0$  towards the dimer as  $|D|$  decreases, following a path on the manifold of total zero magnetization. In spite of that, from Fig. VI.5, it is clear that there is a change in the magnetization of the first excited state at different phases. Since it changes from  $\mathcal{M} = 0$  in the dimer region to  $\mathcal{M} = 1$  in the large- $D$ ,

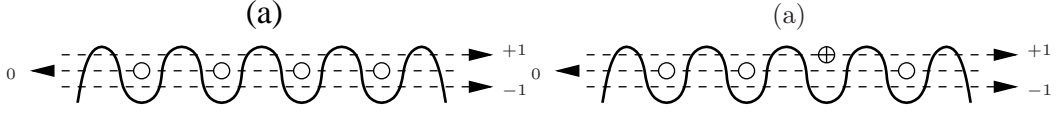


Figure VI.5: (a) Cartoon of the ground state in the large- $D$ . (b) the first excited state with clear total magnetization  $\mathcal{M} = 1$ .

they must cross each other at the phase boundary. Because of that, the level crossing spectroscopy is again useful in the localization of the phase transition line  $D_c^-(\theta)$ .

Again, the main advantage of the phases belonging to different manifolds with constant magnetization is that, we can restrict ourselves to the underlying Hamiltonians.

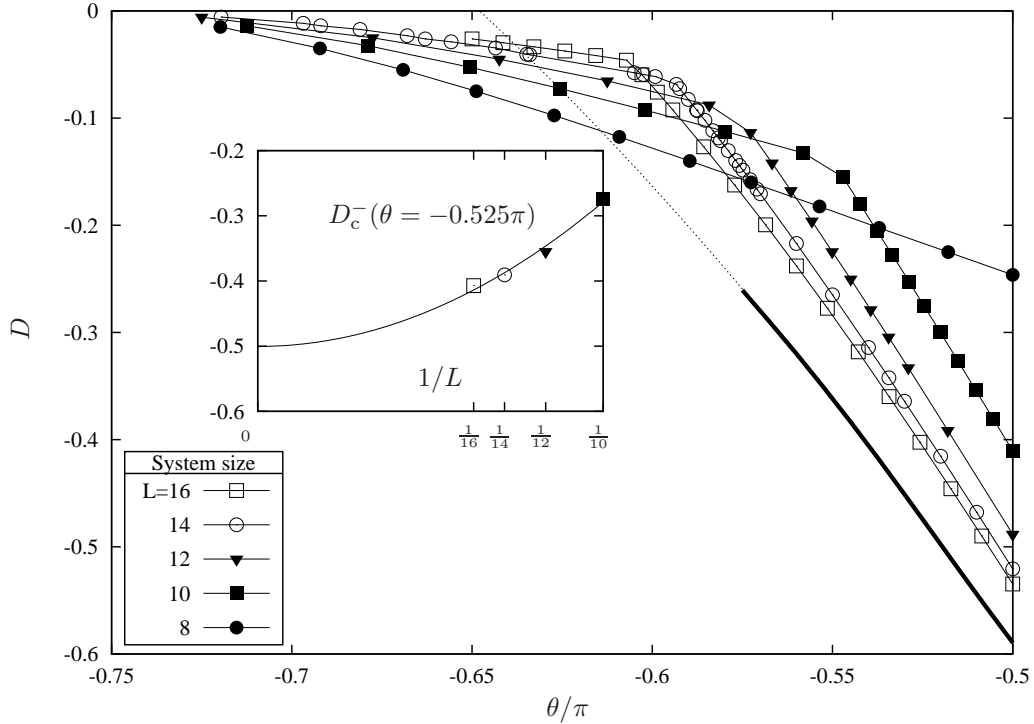


Figure VI.6: Numerical results of the level crossing for several system sizes. The boundary in the thermodynamic limit is given  $D_c^-(\theta)$  shown as a thick line. The inner panel is the finite size scaling in  $1/L$  for a given  $\theta$ .

The numerical procedure is analogous to the already analyzed cases of spin-3/2 and spin-1 for  $D > 0$ . The important value is the dimension of the manifold

$$(VI.7) \quad \dim(\mathcal{M} = 1) = \sum_{n=0}^{(L+1)/2} \frac{L!}{(L-2n-1)!n!(n+1)!}$$

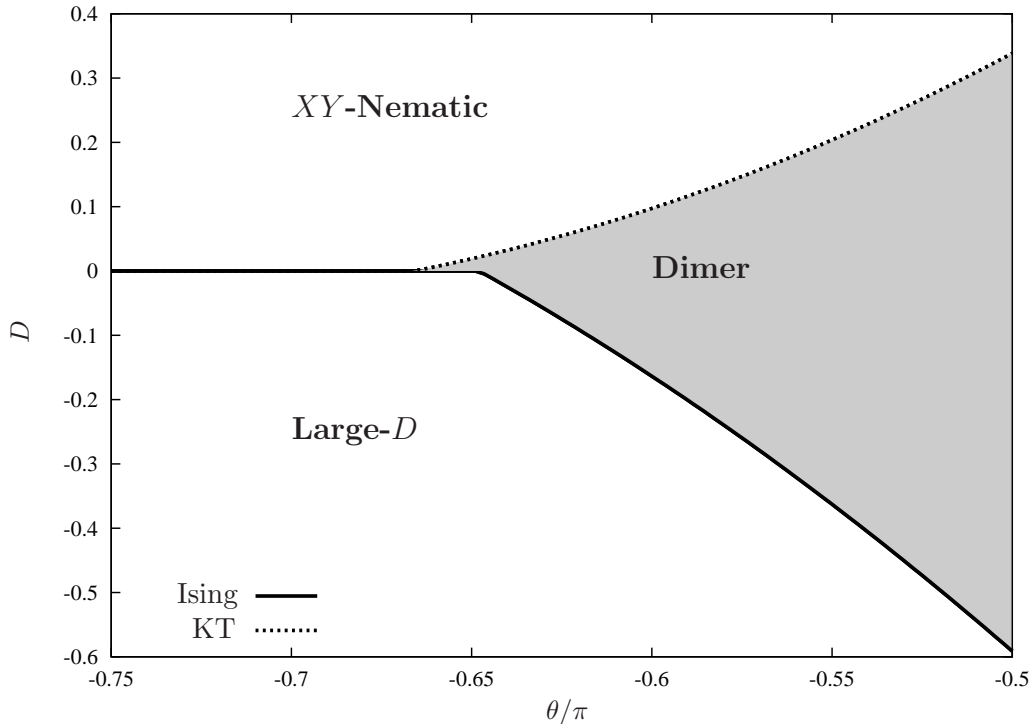


Figure VI.7: Mott phases of anti-ferromagnetic interacting spin-1 bosons at unit filling with the corresponding phase transitions.

which for  $L = 14$  takes the value  $\dim(\mathcal{M} = 1) = 585690$ . However, several difficulties were found as can be seen in Fig. VI.6. First, for  $L \geq 10$ , the boundary presents two sections where the right one grows and the left one shrinks and therefore is expected to vanish, numerically speaking, at the thermodynamic limit. This also agrees with the low energy field theory that predicts an exponentially small dimer region in the vicinity of  $\theta_{\text{SU}(3)}$  for  $D < 0$ <sup>[169]</sup>. The right section would form, in the thermodynamic limit, the actual dimer phase domain. However, as a second difficulty, for  $L < 10$  this region vanishes, contradicting the analytical predictions.

These difficulties encouraged us to go up to  $L = 16$  sites. It is important to note that for this particular system size, the manifolds are much bigger being  $\dim(\mathcal{M} = 0) \approx 5.2 \times 10^6$  and  $\dim(\mathcal{M} = 1) \approx 4.3 \times 10^6$ . This requires much more computational effort than the previous ones since the matrix dimension grows one order of magnitude and the diagonalization procedure goes like  $\mathcal{O}(\text{dim}^2)$ . This translates into an effort hundred times harder.

A third difficulty was found when the finite system scaling was being done. In this respect, fitting to a function only going as either  $1/L$  (Ising) or  $1/L^2$  (KT) failed. Therefore, a linear combination of them was done with the results displayed on the inner panel of Fig. VI.6. As a consequence of this, the

universality class of the phase transition cannot be entirely defined and thus other procedure has to be performed such as the determination of the central charge at  $D = 0$ <sup>[169,170]</sup>. The result is that this phase transition belongs to the Ising universality class.

Finally, Fig. VI.7 shows the expected thermodynamic limit transition lines and the different domains that they separate. This map can be used as a guideline for the experimental exploration of the aforementioned phases.





PART D  
NUMERICS



## Numerical Methods

The high complexity of the quantum many body systems often requires though numerical calculations. In the most of the cases, the complexity is such that super computers are required. However, novel ideas in the field of computational physics and quantum computing had brought to light powerful algorithms able to solve those problems with a notoriously reduced computational effort. Of course, the main feature of the algorithms is the creative way of exploit the physical symmetries and relevant quantities, in order to reduce not only the effective dimension of the problem but the complexity involved. Throughout this thesis, we have made use of mainly two methods, the MPS toolbox and the Lanczos algorithm. In this final chapter we describe these methods in detail, as well as their implementation which constituted a large part of this PhD work.

### VII.1 Representation and Speed-up

#### VII.1.a Scheme

Along this chapter, a lot of formulas and equations are related to very complicated matrix-like products. The use of indexes can be very tedious and confusing. Besides, the point can be lost within such complicated expressions. In order to show a complete and clear development of the different topics, is quite convenient to represent the tensors and all the related operations in a schematic form. The basics of the tensor representation can be described as

- Any object with several entries is called *tensor* and is represented by a box.
- The rank of a tensor  $\mathbf{T}$  is given by the number of outgoing lines it has. For instance a matrix is a 2-rank tensor and therefore it can be represented by

$$\boxed{\mathbf{T}}$$

- Any line that connects two objects represents a sum over a dummy index. For instance, let  $\mathbf{C} = \mathbf{A}\mathbf{B}$  be a matrix-matrix multiplication. In terms of the matrix elements this expression reads

$$C_{ij} = \sum_k A_{ik} B_{kj};$$

but in terms of boxes it is

$$\boxed{\mathbf{C}} = \boxed{\mathbf{A}} \boxed{\mathbf{B}}.$$

- In a tensorial equation the number of free lines denotes the rank of the outgoing tensor, as is shown above.
- States are represented by kets (bras). To clarify this, let us have a look to a ket  $|\phi\rangle$  that describes the state of a given system. In a particular basis  $\{|n\rangle\}$ ,  $|\phi\rangle$  can be written as a linear combination of the basis elements

$$|\phi\rangle = \sum_n c_n |n\rangle.$$

The coefficients can be packed into an object  $\vec{c}$ , that has several entries and can thus be represented by a box. So we finally have,

$$|\phi\rangle = \boxed{c} |n\rangle.$$

In order to get practice with the notation, we will represent the calculation of an expected value by using the box scheme. The first object we need is the bra associated with  $|\phi\rangle$ ,

$$\langle\phi| = \boxed{c^*} \langle n'|.$$

Now we can consider the operator  $\hat{O}$ .

$$\langle\phi|\hat{O}|\phi\rangle = \sum_{n'} \sum_n c_{n'}^* O_{n'n} c_n,$$

$$\begin{aligned} \langle \phi | \hat{O} | \phi \rangle &= \boxed{c^*} \text{---} \langle n' | \hat{O} | n \rangle \text{---} \boxed{c} \\ &= \boxed{c^*} \text{---} \boxed{\hat{O}} \text{---} \boxed{c}, \end{aligned}$$

where  $O_{n'n} = \langle n' | \hat{O} | n \rangle$ . It is important to notice that the right hand side has no free lines, therefore it represents a tensor with rank zero, that is just a number, as expected from the left hand side. A clear example of this can be made by calculating the trace of a matrix:

$$\text{Tr}(\mathbf{T}) = \boxed{\boxed{\mathbf{T}}},$$

where  $\mathbf{T}$  is at both sides of the equation we have a scalar number.

### VII.1.b Product Optimization

When two matrices are multiplied not only their rank will contribute to the complexity of the calculation but their dimensions. For example, let  $\mathbf{A}$  be a 2-rank tensor, so it is a matrix with dimension  $d_1 \times d_2$ , and  $\mathbf{B}$  another matrix with dimension  $d_2 \times d_3$ . Then, the product of this two matrices, represented by the matrix  $\mathbf{C}$ , has a dimension  $d_1 \times d_3$ . Therefore, we have to compute  $d_1 \times d_3$  matrix elements and for each one of them we have to make a sum with  $d_2$  elements. This shows that the number of operations we have to do in order to perform the product  $\mathbf{C} = \mathbf{A}\mathbf{B}$  goes like  $\mathcal{O}(d_1 d_2 d_3)$ .

As we will see below, the calculation of several expected values can lead to very complicated expressions and products in the MPS formalism. As an example, we will have a look into the calculation of the following matrix product that resembles the calculation of a MPS norm or a expected value. So using sum notation over duplicated indexes the expression is given by

$$(VII.1) \quad C = A_{\beta\beta'}^{\alpha} A_{\beta\beta'''}^{\alpha*} B_{\beta'\beta''}^{\alpha'} B_{\beta'''\beta''}^{\alpha'*}$$

$$= \begin{array}{c} \boxed{\mathbf{A}} \text{---} \boxed{\mathbf{B}} \\ | \quad | \\ \boxed{\mathbf{A}^*} \text{---} \boxed{\mathbf{B}^*} \end{array},$$

where thin lines have dimension  $d$  ( $\alpha$ 's) and thick ones  $\chi \gg d$  ( $\beta$ 's). This calculation can be done basically in two ways:

1. Starting with the matrices depicted on the same column we have a number of operations of the order of  $\mathcal{O}(\chi^3 d)$  and the remaining calculation will take about  $\mathcal{O}(\chi^2)$ .

2. Multiplying the matrices in the same row. This takes  $\mathcal{O}(\chi^3 d^2)$ . Then make the remaining product in  $\mathcal{O}(\chi^2 d^2)$  operations.

The total complexity for the second option is then the largest of the two internal products by a factor of  $d$ . From this short analysis is easy to conclude that the first method is more efficient for the calculation of  $\mathbf{C}$ . The same analysis is applied to several other calculations in order to speed-up the performance of the algorithm.

## VII.2 Matrix Product States

In 1992 S. White proposed a new numerical method able to approximate as much as desired the ground state of one-dimensional lattice Hamiltonians such as the Bose-Hubbard model. This method was based on renormalization techniques applied to an optimized way to express the density matrix of a block within the system under consideration and therefore the method received the name *density matrix renormalization group* or DMRG<sup>[171]</sup>. In time, this method would be further developed for both ground state properties<sup>[172,173]</sup> and dynamical problems<sup>[174]</sup> based on the matrix product state ansatz<sup>[175]</sup>. In the following, we review the main ideas behind the MPS ansatz.

### VII.2.a The Ansatz

Let us consider a multipartite one dimensional quantum system made of a chain of  $L$  sites each one with an internal dimension  $d$ , and an arbitrary state  $|\phi\rangle$  that describes the full system. The total Hilbert space can thus be written as  $\mathcal{H} = \bigotimes_{s=1}^L \mathcal{H}^s$  with a total dimension  $d^L$ , where  $\mathcal{H}^s$  is the Hilbert space of the site  $s$ . Furthermore, the state  $|\phi\rangle$  cannot be expressed as a direct product of states belonging to the different sites.

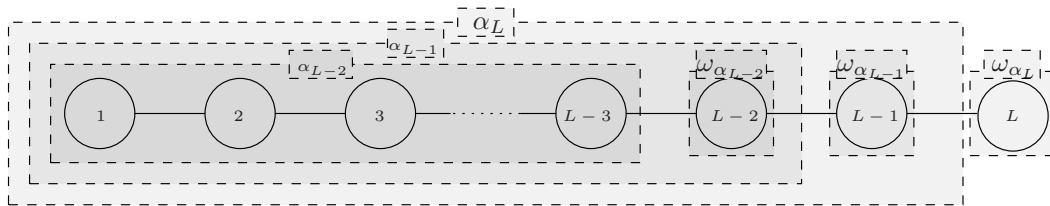


Figure VII.1: System under consideration and a small succession of splittings.

However, since for a bipartite system, whose Hilbert space can be written as the tensor product  $\mathcal{H} = \mathcal{H}^\alpha \otimes \mathcal{H}^\omega$ , it is possible to express any state by the Schmidt decomposition<sup>[176]</sup>

$$(VII.2) \quad |\phi\rangle = \sum_i \lambda_i |\alpha_i\rangle |\omega_i\rangle.$$

We can rewrite  $|\phi\rangle$  by a sequence of splitting and decomposition as depicted in Fig. VII.1. In each step, we separate the last site of the current sub-chain  $|\alpha_{s+1}\rangle$  getting

$$(VII.3) \quad |\alpha_{s+1}\rangle = \sum_{\alpha_s} \lambda_{\alpha_s} |\alpha_s\rangle |\omega_{\alpha_s}(\alpha_{s+1})\rangle.$$

The two set of states  $\{|\alpha_s\rangle\}$  and  $\{|\omega_{\alpha_s}(\alpha_{s+1})\rangle\}$  are bases of the corresponding sub-spaces, and the  $\lambda_{\alpha_s}$  are non-negative numbers that hold the relation

$$(VII.4) \quad \sum_{\alpha_s} \lambda_{\alpha_s}^2 = 1,$$

since the coefficients  $\lambda_{\alpha_s}^2$  are the eigenvalues of the reduced density matrix corresponding to either sub-system. Thus,

$$(VII.5) \quad \sum_{\alpha_s} \lambda_{\alpha_s}^2 \ln(\lambda_{\alpha_s}^2) = S_s,$$

is the *entanglement entropy* between them.

The basis  $\{|\omega_{\alpha_s}(\alpha_{s+1})\rangle\}$  may not be the most convenient set to express the state of the site  $s$ . Therefore, we transform such state into a known local basis  $\{|n_s\rangle\}$  through

$$(VII.6) \quad |\omega_{\alpha_s}(\alpha_{s+1})\rangle = \sum_{n_s=1}^d \Gamma_{\alpha_s \alpha_{s+1}}^{n_s} |n_s\rangle.$$

Under this transformation,  $|\alpha_{s+1}\rangle$  becomes

$$(VII.7) \quad \begin{aligned} |\alpha_{s+1}\rangle &= \sum_{\alpha_s n_s} \lambda_{\alpha_s} \Gamma_{\alpha_s \alpha_{s+1}}^{n_s} |\alpha_s\rangle |n_s\rangle \\ &= \sum_{\alpha_s n_s} A_{\alpha_s \alpha_{s+1}}^{n_s} |\alpha_s\rangle |n_s\rangle, \end{aligned}$$

where  $A_{\alpha_s \alpha_{s+1}}^{n_s} \equiv \lambda_{\alpha_s} \Gamma_{\alpha_s \alpha_{s+1}}^{n_s}$  are in general complex coefficients. From the expression above, it is clear that after packing together the results of the successive splitting and decomposing, the total state  $|\phi\rangle$  can be written as

$$(VII.8) \quad |\phi\rangle = \sum_{\alpha_1 \cdots \alpha_L} \sum_{n_1 \cdots n_L} A_{\alpha_2}^{n_1} \cdots A_{\alpha_s \alpha_{s+1}}^{n_s} \cdots A_{\alpha_L}^{n_L} |n_1\rangle \cdots |n_s\rangle \cdots |n_L\rangle.$$

This expression is exact since no approximation has been done. From the numerical point of view, however, this is still not convenient because still the total number of coefficients is exponentially big. In order to make

the expression computable, we introduce a first approximation by imposing a truncation  $\chi$  in the range of the indexes  $\alpha_s$ . This is justified by the fact that

$$(VII.9) \quad \lambda_{\alpha_s} \sim e^{-\kappa\alpha_s},$$

where  $\kappa > 0$ <sup>[174]</sup>. This means that the truncation process discards the states with less weight, and therefore the representation of the state can be as faithful as desired.

It is important to note that at the middle of the chain  $\alpha_{L/2} = 1, \dots, d^{L/2}$  without imposing any cut-off. In the particular case of hard-core bosons in a chain with  $L = 20$  sites this quantity takes the value  $2^{10} = 1024$ , so the total number of entries for the matrix  $A_{\alpha_{L/2}\alpha_{L/2+1}}^{n_{L/2}}$  is  $2(2^{10})^2 \approx 2 \times 10^6$ . In the following we will assume a uniform cut-off for all the matrices and from this we have that the total number of entries used to represent a given state is  $Ld\chi^2$ . It is very important to note that the number of elements grows linearly with the length of the chain, and hence the manipulation is *only* polynomially complex.

In order to simplify the expressions further, we will introduce the double index sum notation and schematic diagrams to represent matrices as introduced in VII.1. Thus, the box  $\mathbf{A}^s$  represents the matrix  $A_{\alpha_s\alpha_{s+1}}^{n_s}$  at the site  $s$  and every line that connects two boxes represents a summation over the indexes with thick lines being summations over the  $\alpha$ 's and thin lines over  $n$ 's. So the state  $|\phi\rangle$  looks like

$$|\phi\rangle = \boxed{\mathbf{A}^1} \cdots \boxed{\mathbf{A}^s} \cdots \boxed{\mathbf{A}^L}$$

$\underbrace{\hspace{1.5cm}}_{|n_1\rangle} \quad \underbrace{\hspace{1.5cm}}_{|n_s\rangle} \quad \underbrace{\hspace{1.5cm}}_{|n_L\rangle}$

The MPS representation for a given state is not unique since several sets of matrices can have the same final product, then, one can choose a convenient way to express a given state in order to compute expected values or any other quantity with the least effort.

## VII.2.b Basic Examples of MPS

As we already discussed, the MPS ansatz is a suitable technique to approximately represent not too entangled states of a one-dimensional array of  $L$  sites with only a *polynomially* big number of elements. Here, a set of particular examples are shown with the purpose of giving a closer idea of the computational calculations actually done throughout this Thesis. First, the MPS representation of a Fock state will be shown and later, we will consider a two-site system with a spin singlet.



### General Structure of the MPS Tensor

Before starting with the examples of the MPS tensor, it is important to clarify the way the MPS ansatz is manipulated. The general structure can be then depicted by a matrix whose columns enumerate the  $L$  sites and the rows enumerate the  $d$  local states. This is

$$(VII.10) \quad \mathbf{A} = \begin{array}{c} \text{local} \\ \text{basis} \\ \downarrow \end{array} \begin{array}{c} \text{sites} \rightarrow \\ \left( \begin{array}{ccccc} \mathbf{A}^{(1)1} & \dots & \mathbf{A}^{(1)s} & \dots & \mathbf{A}^{(1)L} \\ \vdots & \ddots & \vdots & \ddots & \vdots \\ \mathbf{A}^{(d)1} & \dots & \mathbf{A}^{(d)s} & \dots & \mathbf{A}^{(d)L} \end{array} \right), \end{array}$$

where the sub-matrices  $\mathbf{A}^{n_s}$  have dimension  $\chi \times \chi$ . The internal structure of each sub-matrix is

$$(VII.11) \quad \mathbf{A}^{n_s} = \begin{array}{c} \alpha_s \\ \downarrow \end{array} \begin{array}{c} \alpha_{s+1} \rightarrow \\ \left( \begin{array}{ccc} A_{11}^{n_s} & \dots & A_{1\chi}^{n_s} \\ \vdots & \ddots & \vdots \\ A_{\chi 1}^{n_s} & \dots & A_{\chi\chi}^{n_s} \end{array} \right).$$

This particular choice for organizing the elements of the MPS is very convenient for the further manipulation in the calculation of expected values and correlation functions. Now, let us continue with the examples.

### Fock States

In the frame work of cold atoms, bosons loaded in one-dimensional optical lattices fulfill the requirements for a system to be described by an MPS. The local basis is given by the Fock states that count the number of particles at the site  $s$ . A particular example for  $L = 3$  is

$$(VII.12) \quad |\phi\rangle = |0_1\rangle \otimes |2_2\rangle \otimes |1_3\rangle,$$

where the sub-index labels the site and the ket  $|n_s\rangle$  is the Fock state for  $n_s$  particles. Therefore  $|\phi\rangle$  represents a system with no particle in its first site, two in the second and one in the third. For simplicity, it is assumed that the maximal number of particles allowed in a single site is 2. This is physically the case if there is a strong-enough on-site interaction. But the mechanism that generates such system is not the focus of the current discussion.

The construction of an MPS state is based on the Schmidt decomposition of states, starting by splitting the last site and so on. However, for the case of a Fock state this is already done since the state is separable and at each site we are using the local basis. The exact size of the matrices with no cut-off is  $\chi = 1$  since there is no entanglement between the parts, and therefore we can

describe the system just by a set of numbers instead of matrices. In order to see that, consider the general MPS representation for the state

$$(VII.13) \quad |0_1\rangle|2_2\rangle|1_3\rangle = A_1^{n_1} A_{11}^{n_2} A_1^{n_3} |n_1\rangle|n_2\rangle|n_3\rangle.$$

By equating both states it is possible to read off the matrix elements of the MPS

$$A_{11}^{0_1} = A_{11}^{2_1} = A_{11}^{1_3} = 1,$$

otherwise they are zero. From the matrix elements, we can reconstruct the whole Matrix Product State as a 2-rank tensor as follows

$$(VII.14) \quad \mathbf{A}(\phi) = \begin{array}{c} s = \\ n_0 \\ n_1 \\ n_2 \end{array} \begin{array}{c} 1 \quad 2 \quad 3 \\ \left( \begin{array}{ccc} 1 & 0 & 0 \\ 0 & 0 & 1 \\ 0 & 1 & 0 \end{array} \right) \end{array}.$$

Let us consider the inverse procedure in which we know the MPS representation of a given state  $|\phi\rangle$  and we want to retrieve it in the corresponding Fock basis. By taking the matrix  $A(\phi)$  one can see that the number of sites is  $L = 3$  and each site has 3 internal states. Therefore, the general state for this kind of system can be written as

$$(VII.15) \quad |\phi\rangle = \sum_{\vec{n}} c_{\vec{n}} |\vec{n}\rangle,$$

where  $\vec{n} = (n_1, n_2, n_3)$ . The name of the ansatz comes from the fact that the coefficient related to a given Fock element  $\vec{n}$  is the product of the tensor elements corresponding to it. In other words for  $\vec{n} = (0_1, 0_2, 0_3)$  one has to consider

$$(VII.16) \quad \begin{array}{c} s = \\ n_0 \\ n_1 \\ n_2 \end{array} \begin{array}{c} 1 \quad 2 \quad 3 \\ \left( \begin{array}{ccc} \mathbf{1} & \mathbf{0} & \mathbf{0} \\ 0 & 0 & 1 \\ 0 & 1 & 0 \end{array} \right) \end{array},$$

that gives  $c_{(0_1, 0_2, 0_3)} = 1 \times 0 \times 0 = 0$ . Then it is clear that the only non vanishing product is

$$(VII.17) \quad \begin{array}{c} s = \\ n_0 \\ n_1 \\ n_2 \end{array} \begin{array}{c} 1 \quad 2 \quad 3 \\ \left( \begin{array}{ccc} \mathbf{1} & \mathbf{0} & \mathbf{0} \\ 0 & 0 & \mathbf{1} \\ 0 & \mathbf{1} & 0 \end{array} \right) \end{array},$$

that corresponds to the coefficient  $\vec{n} = (0_1, 2_1, 1_3)$  and therefore the state is exactly the state we expected  $|\phi\rangle = |0_1 2_1 1_3\rangle$ .

It is important to notice that since the coefficient  $c_{\vec{n}}$  depends only on the product of the corresponding elements, several tensors can be constructed in order to reproduce a given state. For instance, the matrix

$$(VII.18) \quad \tilde{\mathbf{A}}(\phi) = \begin{matrix} s = & 1 & 2 & 3 \\ n_0 & \left( \frac{1}{2} & 0 & 0 \right) \\ n_1 & \left( 0 & 0 & 3 \right) \\ n_2 & \left( 0 & \frac{2}{3} & 0 \right) \end{matrix},$$

will produce the very same result. This implies that an optimization can be done in order to compute with the least effort any required calculation. As we will see below, this optimization is performed using the properties of the singular value decomposition and unitary matrices.

In a more general case, entanglement between two sites has to be considered and the cut-off is consequently larger,  $\chi > 1$ . As a very straightforward example we will consider a spin singlet.

### Spin singlet

Entanglement plays a significant role in the description of states via MPS, since the Schmidt decomposition has larger number of components as the entanglement between the two sub-systems increases. In this section, a singlet of two spins 1/2 is considered where each spin is located on a different site. This restrict ourselves to the parameters  $d = 2$  and  $L = 2$ . Then, the starting points are the state  $|\phi\rangle$  and its MPS representation

$$(VII.19) \quad \begin{aligned} |\phi\rangle &= \frac{1}{\sqrt{2}}(|\uparrow_1\downarrow_2\rangle - |\downarrow_1\uparrow_2\rangle) \\ &= A_{\alpha}^{n_1} A_{\alpha}^{n_2} |n_1 n_2\rangle, \quad n_i = \{\uparrow_i, \downarrow_i\}. \end{aligned}$$

As we can see, the state  $|\phi\rangle$  has already the form of a decomposed state where the bases of the sub-systems are the corresponding eigenstates of the spin projection along  $z$ . From it, we can see that  $\chi = 2$  and therefore  $\alpha = 1, 2$ . A possible set of tensor elements is given by

$$(VII.20) \quad A_1^{\uparrow_1} A_1^{\downarrow_2} = -A_2^{\downarrow_1} A_2^{\uparrow_2} = \frac{1}{\sqrt{2}},$$

and all others vanish. To test this statement, let us build the state that the tensor

$$(VII.21) \quad \mathbf{A} = \left( \begin{array}{cc} \left( \frac{1}{\sqrt{2}} & 0 \right) & \left( \begin{array}{c} 0 \\ 1 \end{array} \right) \\ \left( 0 & -\frac{1}{\sqrt{2}} \right) & \left( \begin{array}{c} 1 \\ 0 \end{array} \right) \end{array} \right)$$

represents, where the first row represents  $|\uparrow\rangle$  and the second  $|\downarrow\rangle$ , by calculating the coefficients on the two-spin basis as follows

$$\begin{aligned}
c_{\uparrow_1\uparrow_2} &= \begin{pmatrix} \frac{1}{\sqrt{2}} & 0 \end{pmatrix} \cdot \begin{pmatrix} 0 \\ 1 \end{pmatrix} = 0 \\
c_{\uparrow_1\downarrow_2} &= \begin{pmatrix} \frac{1}{\sqrt{2}} & 0 \end{pmatrix} \cdot \begin{pmatrix} 1 \\ 0 \end{pmatrix} = \frac{1}{\sqrt{2}} \\
c_{\downarrow_1\uparrow_2} &= \begin{pmatrix} 0 & -\frac{1}{\sqrt{2}} \end{pmatrix} \cdot \begin{pmatrix} 0 \\ 1 \end{pmatrix} = -\frac{1}{\sqrt{2}} \\
c_{\downarrow_1\downarrow_2} &= \begin{pmatrix} 0 & -\frac{1}{\sqrt{2}} \end{pmatrix} \cdot \begin{pmatrix} 1 \\ 0 \end{pmatrix} = 0.
\end{aligned}
\tag{VII.22}$$

By summing up these results with the corresponding two-site basis elements, we retrieve the initial spin singlet. Once more, it is important to note that the MPS tensor is not unique.

An interesting feature of the MPS is that it allows a direct calculation of expected values. As an example in this case, let us compute the total magnetization of the system which is the sum over the magnetization on each site. This is expressed by

$$\mathcal{M} = \sum_{i=1}^2 \langle \hat{S}_i^z \rangle,
\tag{VII.23}$$

where  $\hat{S}_i^z$  is defined as

$$\hat{S}_i^z = \frac{1}{2} (|\uparrow_i\rangle\langle\uparrow_i| - |\downarrow_i\rangle\langle\downarrow_i|).
\tag{VII.24}$$

Since  $\{|\uparrow_i\rangle, |\downarrow_i\rangle\}$  is the local base, the magnetization is represented by the diagonal matrix

$$\mathbf{S}_i^z = \frac{1}{2} \begin{pmatrix} 1 & 0 \\ 0 & -1 \end{pmatrix}.
\tag{VII.25}$$

Let us focus on the expected value of such operator on the singlet state  $|\phi\rangle$  in its MPS representation. Thus, initially considering  $i = 1$  we have

$$\begin{aligned}
\langle \phi | \hat{S}_1^z | \phi \rangle &= A_{\alpha_2}^{n_1^*} A_{\alpha_2}^{n_2^*} \langle n_1' n_2' | \hat{S}_1^z A_{\alpha_2}^{n_1} A_{\alpha_2}^{n_2} | n_1 n_2 \rangle \\
&= \left( A_{\alpha_2}^{n_1^*} A_{\alpha_2}^{n_1} \langle n_1' | \hat{S}_1^z | n_1 \rangle \right) \left( A_{\alpha_2}^{n_2^*} A_{\alpha_2}^{n_2} \langle n_2' | n_2 \rangle \right) \\
&= [E^1(\hat{m}_1)]_{\alpha_2 \alpha_2'} [E^2(\hat{I}_2)]_{\alpha_2 \alpha_2'} \\
&= \text{Tr} \left[ \mathbf{E}^1(\hat{S}_1^z) \mathbf{E}^2(\hat{I}_2) \right]
\end{aligned}
\tag{VII.26}$$

where in general  $E^i(\hat{O}_i)$  is the *transfer matrix* of the operator  $\hat{O}_i$  at the site  $i$  [177]. A detailed explanation of it will be presented in the following sections. In this example, the calculation of this matrix is quite straightforward giving

$$\begin{aligned}
\mathbf{E}^1(\hat{S}_1^z) &= \begin{pmatrix} \frac{1}{\sqrt{2}} & 0 \\ 0 & -\frac{1}{\sqrt{2}} \end{pmatrix} \frac{1}{2} \begin{pmatrix} 1 & 0 \\ 0 & -1 \end{pmatrix} \begin{pmatrix} \frac{1}{\sqrt{2}} & 0 \\ 0 & -\frac{1}{\sqrt{2}} \end{pmatrix} \\
&= \begin{pmatrix} \frac{1}{4} & 0 \\ 0 & -\frac{1}{4} \end{pmatrix}, \\
\mathbf{E}^2(\hat{I}_2) &= \begin{pmatrix} 0 & 1 \\ 1 & 0 \end{pmatrix} \begin{pmatrix} 1 & 0 \\ 0 & 1 \end{pmatrix} \begin{pmatrix} 0 & 1 \\ 1 & 0 \end{pmatrix} \\
&= \begin{pmatrix} 1 & 0 \\ 0 & 1 \end{pmatrix},
\end{aligned}
\tag{VII.27}$$

and therefore

$$\begin{aligned}
\langle \phi | \hat{S}_1^z | \phi \rangle &= \text{Tr} \left[ \begin{pmatrix} \frac{1}{4} & 0 \\ 0 & -\frac{1}{4} \end{pmatrix} \begin{pmatrix} 1 & 0 \\ 0 & 1 \end{pmatrix} \right] \\
&= 0.
\end{aligned}
\tag{VII.28}$$

An analogous calculation will show that  $\langle \phi | \hat{S}_2^z | \phi \rangle = 0$  and thus the total magnetization also vanishes as expected.

We have analyzed the way a expected value is calculated within the MPS framework. And although the results are quite direct, it is clear that for larger and more complex systems the expressions involved are tedious and long. Because of that, henceforth the box notation is much more useful to point out the important quantities and procedure leaving behind the indexes and the sum notation.

### VII.2.c Orthogonalization of the states

Let  $|\phi\rangle$  be a state that describes a system with  $L$  sites each one with internal dimension  $d$ . It can be written in the form of a MPS as

$$|\phi\rangle = A_{\alpha_2}^{n_1} \cdots A_{\alpha_s \alpha_{s+1}}^{n_s} \cdots A_{\alpha_L}^{n_L} |n_1\rangle \cdots |n_s\rangle \cdots |n_L\rangle.
\tag{VII.29}$$

In order to calculate any local observable on a given site  $s$  such as  $\langle \phi | \hat{O}^s | \phi \rangle$ , it is necessary the computation of the *transfer matrices*  $\mathbf{E}^s(\hat{I})$  defined by

$$\mathbf{E}^s(\hat{I}) = \begin{array}{c} \begin{array}{ccc} \alpha_s & \boxed{\mathbf{A}^s} & \alpha_{s+1} \\ \hline & & \end{array} \\ \begin{array}{ccc} \alpha'_s & \boxed{\mathbf{A}^{s*}} & \alpha'_{s+1} \\ \hline & & \end{array} \\ \begin{array}{ccc} \text{---} \langle n'_s | \hat{I} | n_s \rangle \text{---} & & \end{array} \end{array}$$

$$(VII.30) \quad = A_{\alpha'_s \alpha'_{s+1}}^{n'_s \star} A_{\alpha_s \alpha_{s+1}}^{n_s} \langle n'_s | \hat{I} | n_s \rangle.$$

In a closer look to the structure of the transfer matrices, one realizes that they are the product of the matrix  $\mathbf{A}^s$  with its self-Hermitian conjugate,

$$(VII.31) \quad \begin{aligned} E_{\alpha'_s \alpha'_{s+1}}^{\alpha_s \alpha_{s+1}}(\hat{I}) &= A_{\alpha'_s \alpha'_{s+1}}^{n'_s \star} A_{\alpha_s \alpha_{s+1}}^{n_s} \langle n'_s | \hat{I} | n_s \rangle \\ &= A_{\alpha'_s \alpha'_{s+1}}^{n_s \star} A_{\alpha_s \alpha_{s+1}}^{n_s} \\ E_{\gamma'_s}^{\gamma_s}(\hat{I}) &= A_{\gamma'_s n_s}^{\star} A_{n_s \gamma_s} \\ \mathbf{E}^s(\hat{I}) &= \mathbf{A}^{s\dagger} \mathbf{A}^s. \end{aligned}$$

where we introduced the index  $\gamma_s \equiv (\alpha_s, \alpha_{s+1})$ , rearranged the indexes and performed the sum over  $n'_s$ .

Up to now, we did not assume any particular structure for the matrix  $\mathbf{A}^s$  although we already saw that the MPS representation is not unique and we can select the most convenient one. Moreover, the last equation tells us that if  $\mathbf{A}^s$  is an unitary matrix the corresponding transfer matrix  $\mathbf{E}^s(\hat{I})$  is in itself an identity matrix. This is a huge advantage since it always appears in products and therefore can be ignored saving  $\mathcal{O}(\chi^4 d)$  operations. This encourages us to develop a procedure to keep most  $\mathbf{A}^s$  matrices unitary. A standard way to do so is through the *Singular Value Decomposition* (SVD) as follows<sup>[178]</sup>

- Let us consider first the matrix related with the site  $s = 1$  and its *Singular Value Decomposition* (SVD)

$$(VII.32) \quad A_{\alpha_2}^{n_1} = \sum_{\beta_2} U_{\beta_2}^{n_1} d_{\beta_2} V_{\beta_2 \alpha_2},$$

by definition, the matrices  $\mathbf{U}^1$  and  $\mathbf{V}^2$  are unitary. So we will replace the matrix  $A_{\alpha_2}^{n_1}$  with the elements of  $U_{b_2}^{n_1}$ . In this way, the matrix associated with  $s = 1$  is already orthogonal. However, we have to keep the state unaffected. Therefore we cluster together the matrices  $\mathbf{d}^2$  and  $\mathbf{V}^2$  to the matrix to the right, namely  $\mathbf{A}^2$ .

- This is simple to see when we consider not only the first but the second matrix, so we have

$$(VII.33) \quad \begin{aligned} \sum_{\alpha_2} A_{\alpha_2}^{n_1} A_{\alpha_2 \alpha_3}^{n_2} &= \sum_{\alpha_2} \sum_{\beta_2} U_{\beta_2}^{n_1} (d_{\beta_2} V_{\beta_2 \alpha_2} A_{\alpha_2 \alpha_3}^{n_2}) \\ &= \sum_{\beta_2} U_{\beta_2}^{n_1} \tilde{A}_{\beta_2 \alpha_3}^{n_2}. \end{aligned}$$

- From this point on, the procedure should change a bit since the matrices have three indexes instead of two. To solve this problem, we will combine

the indexes  $n_s$  and  $\beta_s$  as just one index  $\nu_s$  before performing the SVD. In particular, for  $s = 2$  we have

$$\begin{aligned}
 \tilde{A}_{\beta_2\alpha_3}^{n_2} &= \tilde{A}_{\nu_2\alpha_3} \\
 &= \sum_{\beta_3} U_{\nu_2\beta_3} d_{\beta_3} V_{\beta_3\alpha_3} \\
 &= \sum_{\beta_3} U_{\beta_2\beta_3}^{n_2} d_{\beta_3} V_{\beta_3\alpha_3}.
 \end{aligned}
 \tag{VII.34}$$

Once more, we take the unitary matrix  $\mathbf{U}^2$  as the matrix describing the site  $s = 2$  and the rest should be multiplied to the matrix  $\mathbf{A}^3$  to form the updated matrix  $\tilde{\mathbf{A}}^3$ . It is important to note that the unitarity of  $\mathbf{U}^2$  is expressed as

$$\mathbf{I} = \mathbf{U}^{2\dagger} \mathbf{U}^2,
 \tag{VII.35}$$

or, explicitly

$$\begin{aligned}
 \delta_{\beta'_3}^{\beta_3} &= \sum_{\nu} U_{\nu_2\beta'_3}^* U_{\nu_2\beta_3} \\
 &= \sum_{\beta_2} \sum_{n_2} U_{\beta_2\beta'_3}^{n_2*} U_{\beta_2\beta_3}^{n_2}.
 \end{aligned}
 \tag{VII.36}$$

- We proceed in the same way moving the non-unitary matrices to the right on each step. However, we cannot go beyond  $s = L - 1$ . This guarantees us that when computing the norm of the state, only the last site contributes reducing the complexity of the calculation by  $L$  which in several cases may be of the order of 50.

A more clear way to display the previous procedure on the state  $|\phi\rangle$  is given by

$$\begin{aligned}
 |\phi\rangle &= \begin{array}{c} \mathbf{A}^1 \\ \lfloor n_1 \rfloor \end{array} - \begin{array}{c} \mathbf{A}^2 \\ \lfloor n_2 \rfloor \end{array} - \begin{array}{c} \mathbf{A}^3 \\ \lfloor n_3 \rfloor \end{array} - \dots - \begin{array}{c} \mathbf{A}^s \\ \lfloor n_s \rfloor \end{array} - \dots - \begin{array}{c} \mathbf{A}^L \\ \lfloor n_L \rfloor \end{array} \\
 &= \begin{array}{c} \mathbf{U}^1 \\ \lfloor n_1 \rfloor \end{array} - \begin{array}{c} \tilde{\mathbf{A}}^2 \\ \lfloor n_2 \rfloor \end{array} - \begin{array}{c} \mathbf{A}^3 \\ \lfloor n_3 \rfloor \end{array} - \dots - \begin{array}{c} \mathbf{A}^s \\ \lfloor n_s \rfloor \end{array} - \dots - \begin{array}{c} \mathbf{A}^L \\ \lfloor n_L \rfloor \end{array} \\
 &= \begin{array}{c} \mathbf{U}^1 \\ \lfloor n_1 \rfloor \end{array} - \begin{array}{c} \mathbf{U}^2 \\ \lfloor n_2 \rfloor \end{array} - \begin{array}{c} \tilde{\mathbf{A}}^3 \\ \lfloor n_3 \rfloor \end{array} - \dots - \begin{array}{c} \mathbf{A}^s \\ \lfloor n_s \rfloor \end{array} - \dots - \begin{array}{c} \mathbf{A}^L \\ \lfloor n_L \rfloor \end{array},
 \end{aligned}$$

where on each step we perform a SVD and the product with the matrix at the right. Although this procedure is very useful, often it is necessary to compute

expected values of operators at a middle point on the chain. Therefore, it would be convenient to implement a similar procedure starting from the right and moving to the left.

When performing the SVD to the left, the indexes have to be treated in a different way. In order to visualize this let us consider the last matrix

$$(VII.37) \quad A_{\alpha_L}^{n_L} = \sum_{\beta_L} U_{\alpha_L \beta_L} d_{\beta_L} V_{\beta_L}^{n_L},$$

once more, the very last matrix  $\mathbf{V}^L$  is unitary. By following an analog procedure as above, we should compact all the information contained in the matrices  $\mathbf{U}^L$  and  $\mathbf{d}^L$  together with  $\mathbf{A}^{L-1}$ . Then, let us consider the last two matrices

$$(VII.38) \quad \begin{aligned} \sum_{\alpha_L} A_{\alpha_{L-1} \alpha_L}^{n_{L-1}} A_{\alpha_L}^{n_L} &= \sum_{\alpha_L} \sum_{\beta_L} \left( A_{\alpha_{L-1} \alpha_L}^{n_{L-1}} U_{\alpha_L \beta_L} d_{\beta_L} \right) V_{\beta_L}^{n_L} \\ &= \sum_{\beta_L} \tilde{A}_{\alpha_{L-1} \beta_L}^{n_{L-1}} V_{\beta_L}^{n_L}. \end{aligned}$$

With this procedure we can keep changing the matrices recursively to unitary ones starting from both extremes. At the end, we will have only a non-unitary matrix with the whole information of the system. So the final expression reads,

$$(VII.39) \quad \begin{aligned} |\phi\rangle &= \boxed{\mathbf{U}^1} \cdots \boxed{\mathbf{U}^{s-1}} \boxed{\mathbf{A}^s} \boxed{\mathbf{V}^{s+1}} \cdots \boxed{\mathbf{V}^L} \\ &\quad \underbrace{\hspace{1.5cm}}_{|n_1\rangle} \quad \underbrace{\hspace{1.5cm}}_{|n_{s-1}\rangle} \quad \underbrace{\hspace{1.5cm}}_{|n_s\rangle} \quad \underbrace{\hspace{1.5cm}}_{|n_{s+1}\rangle} \quad \underbrace{\hspace{1.5cm}}_{|n_L\rangle} \\ &= U_{\alpha_2}^{n_1} \cdots U_{\alpha_{s-1} \alpha_s}^{n_{s-1}} A_{\alpha_s \alpha_{s+1}}^{n_s} V_{\alpha_{s+1} \alpha_{s+2}}^{n_{s+1}} \cdots V_{\alpha_L}^{n_L} |n_1\rangle \cdots |n_L\rangle. \end{aligned}$$

Now we want to manipulate the matrices  $\mathbf{U}^s$  altogether. To do so, we will show by induction that the vector

$$(VII.40) \quad |\alpha_s\rangle = \sum_{\alpha_1 \cdots \alpha_{s-1}} \sum_{n_1 \cdots n_{s-1}} U_{\alpha_2}^{n_1} \cdots U_{\alpha_{s-1} \alpha_s}^{n_{s-1}} |n_1\rangle \cdots |n_{s-1}\rangle,$$

is orthonormalized. This will simplify significantly any observable calculation later on. By now, let focus in the following inner product of the left matrices

$$\begin{aligned} \langle \alpha'_s | \alpha_s \rangle &= \begin{array}{c} \boxed{\mathbf{U}^1} \cdots \boxed{\mathbf{U}^k} \cdots \boxed{\mathbf{U}^{s-1}} \\ \vdots \\ \boxed{\mathbf{U}^{1*}} \cdots \boxed{\mathbf{U}^{k*}} \cdots \boxed{\mathbf{U}^{s-1*}} \end{array} \\ &= \left[ \mathbf{E}^1(\hat{I}) \cdots \mathbf{E}^k(\hat{I}) \cdots \mathbf{E}^{s-1}(\hat{I}) \right]_{\alpha'_s}^{\alpha_s}, \end{aligned}$$



where in this particular case

$$(VII.41) \quad \begin{aligned} \left[ \mathbf{E}^k(\hat{I}) \right]_{\alpha'_k \alpha'_{k+1}}^{\alpha_k \alpha_{k+1}} &= U_{\alpha'_k \alpha'_{k+1}}^{n'_k \star} U_{\alpha_k \alpha_{k+1}}^{n_k} \langle n'_k | n_k \rangle \\ &= U_{\alpha'_k \alpha'_{k+1}}^{n_k \star} U_{\alpha_k \alpha_{k+1}}^{n_k}. \end{aligned}$$

For the induction procedure we are going to assume that

$$(VII.42) \quad \left[ \mathbf{E}^1(\hat{I}) \cdots \mathbf{E}^{k-1}(\hat{I}) \right]_{\alpha'_k}^{\alpha_k} = \delta_{\alpha'_k}^{\alpha_k},$$

so we have that

$$(VII.43) \quad \begin{aligned} \left[ \mathbf{E}^1(\hat{I}) \cdots \mathbf{E}^k(\hat{I}) \right]_{\alpha'_k \alpha'_{k+1}}^{\alpha_k \alpha_{k+1}} &= \left[ \mathbf{E}^1(\hat{I}) \cdots \mathbf{E}^{k-1}(\hat{I}) \right]_{\alpha'_k}^{\alpha_k} \left[ \mathbf{E}^k(\hat{I}) \right]_{\alpha'_k \alpha'_{k+1}}^{\alpha_k \alpha_{k+1}} \\ &= U_{\alpha'_k \alpha'_{k+1}}^{n_k \star} U_{\alpha_k \alpha_{k+1}}^{n_k} \delta_{\alpha'_k}^{\alpha_k} \\ &= U_{\alpha_k \alpha'_{k+1}}^{n_k \star} U_{\alpha_k \alpha_{k+1}}^{n_k}. \end{aligned}$$

This final result is exactly the result of the unitarity defined by Eq. (VII.36) after changing the name of the dummy variables  $\beta_s$  to  $\alpha_s$ . Therefore, we have

$$(VII.44) \quad \left[ \mathbf{E}^1(\hat{I}) \cdots \mathbf{E}^k(\hat{I}) \right]_{\alpha'_{k+1}}^{\alpha_{k+1}} = \delta_{\alpha'_{k+1}}^{\alpha_{k+1}}.$$

The final part of the demonstration is that the assumption is correct for the first site. However, this is granted by Eq. (VII.32).

The result showed in Eq. (VII.44) is valid for any  $k < s$ , where  $s$  is the site where the information is kept. The most important result of this calculation is then

$$(VII.45) \quad \langle \alpha'_s | \alpha_s \rangle = \delta_{\alpha'_s}^{\alpha_s}.$$

An analog procedure shows that the right part also can be described by a state

$$(VII.46) \quad |\omega_{\alpha_{s+1}}\rangle = \sum_{\alpha_{s+2} \cdots \alpha_L} \sum_{n_{s+1} \cdots n_L} V_{\alpha_{s+1} \alpha_{s+2}}^{n_{s+1}} \cdots V_{\alpha_{L-1} \alpha_L}^{n_{L-1}} V_{\alpha_L}^{n_L},$$

with the property

$$(VII.47) \quad \langle \omega'_{\alpha_{s+1}} | \omega_{\alpha_{s+1}} \rangle = \delta_{\alpha'_{s+1}}^{\alpha_{s+1}}.$$

This ensures us that a very compact form of writing the state is given by the expression

$$(VII.48) \quad |\phi\rangle = \sum_{n_s \alpha_s \alpha_{s+1}} A_{\alpha_s \alpha_{s+1}}^{n_s} |\alpha_s\rangle |n_s\rangle |\omega_{\alpha_{s+1}}\rangle,$$

where all the information is kept in the non-unitary matrix  $\mathbf{A}^s$ . The real power of this way of expressing the MPS comes when expected values or correlation functions are calculated, since much less computational effort has to be employed. Thus, let us analyze how to compute single site-expected values.

### VII.2.d Expected values

The MPS is a representation of the state of the system and therefore, it contains all the information regarding the observables. In order to extract such information from it, it is important to develop further the analysis of this representation. To introduce us to this calculation, we consider here the expected value of the identity operator that lead us directly to the calculation of the norm of a given orthonormalized MPS state.

$$\begin{aligned}
 \langle \phi | \phi \rangle &= A_{\alpha_s \alpha_{s+1}}^{n_s} A_{\alpha'_s \alpha'_{s+1}}^{n'_s \star} \langle \alpha_s | \alpha'_s \rangle \langle n_s | s'_s \rangle \langle \omega_{\alpha_{s+1}} | \omega'_{\alpha_{s+1}} \rangle \\
 (VII.49) \quad &= A_{\alpha_s \alpha_{s+1}}^{n_s} A_{\alpha_s \alpha_{s+1}}^{n_s \star} \\
 &= \text{Tr} \left[ \mathbf{E}^s(\hat{I}) \right].
 \end{aligned}$$

This expression has a complexity  $\mathcal{O}(\chi^2 d)$  which is much smaller than the initial expectation of  $\mathcal{O}(\chi^4 d L)$ . For any local observable, we have only to replace  $\hat{I}^s$  by  $\hat{O}^s$  and thus the complexity rises to  $\mathcal{O}(\chi^2 d(d+1))$  which is still low enough. Nonetheless, for two-sites or more, operators the complexity increases significantly since the intermediate transfer have to be taken into account. In order to study this problem, we consider here a more complex observable.

One kind of observables that becomes very important in the case of one-dimensional quantum systems is the set of correlations. In particular, first order correlation functions such as the density-density correlation or the matrix elements of the one-particle density matrix are clear examples of this (see chapters I and II). A general way to express them is

$$(VII.50) \quad \mathcal{G}_\Delta(\hat{O}_1^s, \hat{O}_2^{s+\Delta}) = \langle \phi | \hat{O}_1^s \hat{O}_2^{s+\Delta} | \phi \rangle,$$

where the operators  $\hat{O}_1^s$  and  $\hat{O}_2^{s+\Delta}$  are independent operators that act on the sites  $s$  and  $s + \Delta$  respectively and  $|\phi\rangle$  is a state that can be written in the form of a orthogonalized MPS that collects the information at the site  $k < s$ . By making use of the orthogonal matrices, the correlation function can be written as

$$\begin{aligned}
 \mathcal{G}_\Delta(\hat{O}_1^s, \hat{O}_2^{s+\Delta}) &= \begin{array}{c} \left[ \begin{array}{cccc} \mathbf{A}^k & \mathbf{A}^s & \mathbf{A}^i & \mathbf{A}^{s+\Delta} \\ \hat{I}^k & \hat{O}^s & \hat{I}^i & \hat{I}^{s+\Delta} \\ \mathbf{A}^{k\star} & \mathbf{A}^{s\star} & \mathbf{A}^{i\star} & \mathbf{A}^{s+\Delta\star} \end{array} \right] \end{array} \\
 (VII.51) \quad &= \text{Tr} \left[ \left( \prod_{i=k}^{s-1} \mathbf{E}^i(\hat{I}) \right) \mathbf{E}^s(\hat{O}^s) \left( \prod_{j=s+1}^{s+\Delta-1} \mathbf{E}^j(\hat{I}) \right) \mathbf{E}^{s+\Delta}(\hat{O}^{s+\Delta}) \right].
 \end{aligned}$$

Where all the transfer matrices related to the sites outside the interval  $[k, s+\Delta]$  are equal to the identity. This simple example shows both the power and the complexity of the MPS. On one side, it is possible to compute correlation functions which are not always retrieved in other approaches. On the other side, this calculation requires a computational effort that goes like  $\mathcal{O}(\chi^4 d(s + \Delta - k))$  which is quite high but still polynomial.

Although the initial procedure seems to be quite complex, it is possible to adapt other algorithms, such as the time evolution or the variational method for ground state calculations, to keep the matrices orthonormalized and thus keep the complexity of the system under control.

### VII.2.e Time evolution

One of the methods to perform time evolution calculations on a MPS is an algorithm called *Time Evolving Block Decimation*<sup>[175]</sup>. The main idea behind it is to make use of the fact that many one-dimensional lattice Hamiltonians can be written as the sum over two-site operators. Thus, if a small enough time step is considered then the time evolution operator can be decomposed into the product of smaller evolution operators. This algorithm works as follows:

1. The time evolution of the system is given by the Schrödinger equation

$$(VII.52) \quad i\hbar \frac{\partial}{\partial t} |\phi(t)\rangle = \hat{H} |\phi(t)\rangle,$$

whose formal solution is

$$(VII.53) \quad |\phi(t)\rangle = e^{-\frac{i}{\hbar} \hat{H} t} |\phi(0)\rangle,$$

where the initial state of the system is described by the initial condition  $|\phi(0)\rangle$ .

2. The system is composed by an array of  $L$  sites with up to nearest-neighbor interaction and hopping. That suggests the splitting of the Hamiltonian into two parts  $\hat{H}^{\text{even}}$  and  $\hat{H}^{\text{odd}}$  where

$$(VII.54) \quad \hat{H}^{\text{parity}} = \sum_{i:\text{parity}} \hat{H}_{i,i+1}$$

3. For a small enough time step ( $\delta t \rightarrow 0$ ), it is possible to employ the Suzuki-Trotter approximation for the time-evolution operator

$$(VII.55) \quad e^{-\frac{i}{\hbar} \hat{H} \delta t} \approx e^{-\frac{i}{\hbar} \hat{H}^{\text{even}} \delta t} e^{-\frac{i}{\hbar} \hat{H}^{\text{odd}} \delta t}.$$

$$\hat{H}_{\text{odd}} = \hat{H}_{12} + \hat{H}_{34} + \dots$$

$$\hat{H}_{\text{even}} = \hat{H}_{23} + \hat{H}_{45} + \dots$$

Furthermore, since each term in  $\hat{H}^{\text{parity}}$  commutes with each other it is possible to express

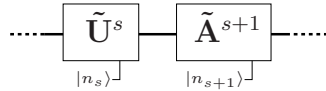
$$(VII.56) \quad e^{-\frac{i}{\hbar}\hat{H}^{\text{parity}}\delta t} = \prod_{i:\text{parity}} e^{-\frac{i}{\hbar}\hat{H}_{i,i+1}\delta t}.$$

From this expression, it follows that in order to perform the total time step  $\delta t$  it is only necessary to consider how to apply the two-sites evolution operator into the state represented by a MPS and repeat the procedure sweeping over all the even site-pairs and afterwards for the odd ones.



(a) Two-site time evolution operator acting on the MPS.

(b) The result of the matrix product in the last step leads to a non-MPS.



(c) A SVD is performed in order to project the state into an MPS. The updated state may have a bigger dimension due to entanglement during the time evolution.

Figure VII.2: Schematic Time Evolving Bloch Decimation algorithm on an Matrix Product State. The Suzuki-Trotter decomposition allows the time evolution operator to act only on a pair of sites.

4. Then, in one step of the sweeping, the two-sites time evolution operation acts on the orthogonalized MPS  $|\phi(t)\rangle$  as follows. First, let  $s$  be the site with no unitary matrix, that means that to the left and to the right of

it the matrices are orthonormalized,  $\mathbf{U}^i$  for  $i < s$  and  $\mathbf{V}^i$  for  $i > s$  as shown in Eq. (VII.48). The evolution operator is applied on  $s$  and its nearest neighbor, for instance the right one  $s + 1$ . That is

$$\begin{aligned}
|\phi(t + \delta t_s)\rangle &= e^{-\frac{i}{\hbar} \hat{H}_{s,s+1} \delta t} |\phi(t + dt_{s-2})\rangle \\
\text{(VII.57)} \quad &= e^{-\frac{i}{\hbar} \hat{H}_{s,s+1} \delta t} A_{\alpha_s \alpha_{s+1}}^{n_s} V_{\alpha_{s+1} \alpha_{s+2}}^{n_{s+1}} |\alpha_s\rangle |n_s n_{s+1}\rangle |\omega_{s+2}\rangle \\
&= \Theta_{\alpha_s \alpha_{s+2}}^{n_s n_{s+1}} |\alpha_s\rangle |n_s n_{s+1}\rangle |\omega_{s+2}\rangle.
\end{aligned}$$

5. In order to recover the ansatz, it is necessary to recalculate the updated matrices  $\tilde{\mathbf{U}}^s$  and  $\tilde{\mathbf{A}}^{s+1}$ , so we let the matrix at the site  $s$  orthogonalized whereas the one at  $s + 1$  is not. This can be done by performing a singular value decomposition of the system. It will split the matrix  $\Theta^{s,s+1}$  into two parts and we can select one of them to be unitary and by this, keeping the total MPS orthogonal. For example, if the swap is going to the right the matrix chosen to be unitary is the one to the left, in this case  $\tilde{\mathbf{U}}^s$ .

$$\begin{aligned}
\Theta_{\alpha_s \alpha_{s+2}}^{n_s n_{s+1}} &= \sum_{\tilde{\alpha}_{s+1}=1}^{\chi'} \tilde{U}_{\alpha_s \tilde{\alpha}_{s+1}}^{n_s} \left( d_{\tilde{\alpha}_{s+1}} V_{\tilde{\alpha}_{s+1} \alpha_{s+2}}^{n_{s+1}} \right) \\
\text{(VII.58)} \quad &= \sum_{\tilde{\alpha}_{s+1}=1}^{\chi'} \tilde{U}_{\alpha_s \tilde{\alpha}_{s+1}}^{n_s} \tilde{A}_{\tilde{\alpha}_{s+1} \alpha_{s+2}}^{n_{s+1}}.
\end{aligned}$$

6. Note that in general  $\chi' \neq \chi$  and hence the size of the MPS matrices can increase. The optimal matrix dimension can be calculated by

$$\text{(VII.59)} \quad \sum_i^{\chi_{\text{op}}} d_i = 1 - \epsilon,$$

where  $\epsilon \ll 1$  is the threshold of the desired precision.

7. Once the matrices are resized according to the optimal  $\chi_{\text{op}}$ , the result is plugged back in the evolving MPS, giving

$$\text{(VII.60)} \quad |\phi(t + \delta t_s)\rangle = \tilde{U}_{\alpha_s \tilde{\alpha}_{s+1}}^{n_s} \tilde{A}_{\tilde{\alpha}_{s+1} \alpha_{s+2}}^{n_{s+1}} |\alpha_s\rangle |n_s n_{s+1}\rangle |\omega_{s+2}\rangle.$$

8. In order to keep the state orthogonalized and ready for the next two-sites evolution operator, it is necessary to pass the information to the site  $s + 2$ . Recalling that the operation is performed over all the even and later on the odd sites. Thus, a new singular value decomposition between the sites  $s + 1$  and  $s + 2$  is

$$\begin{aligned}
\text{(VII.61)} \quad |\phi(t + \delta t_s)\rangle &= \tilde{A}_{\tilde{\alpha}_{s+1} \alpha_{s+2}}^{n_{s+1}} V_{\alpha_{s+2} \alpha_{s+3}}^{n_{s+2}} |\tilde{\alpha}_{s+1}\rangle |n_{s+1} n_{s+2}\rangle |\omega_{s+2}\rangle \\
&= \tilde{U}_{\tilde{\alpha}_{s+1} \alpha_{s+2}}^{n_{s+1}} A_{\alpha_{s+2} \alpha_{s+3}}^{n_{s+2}} |\tilde{\alpha}_{s+1}\rangle |n_{s+1} n_{s+2}\rangle |\omega_{s+2}\rangle,
\end{aligned}$$

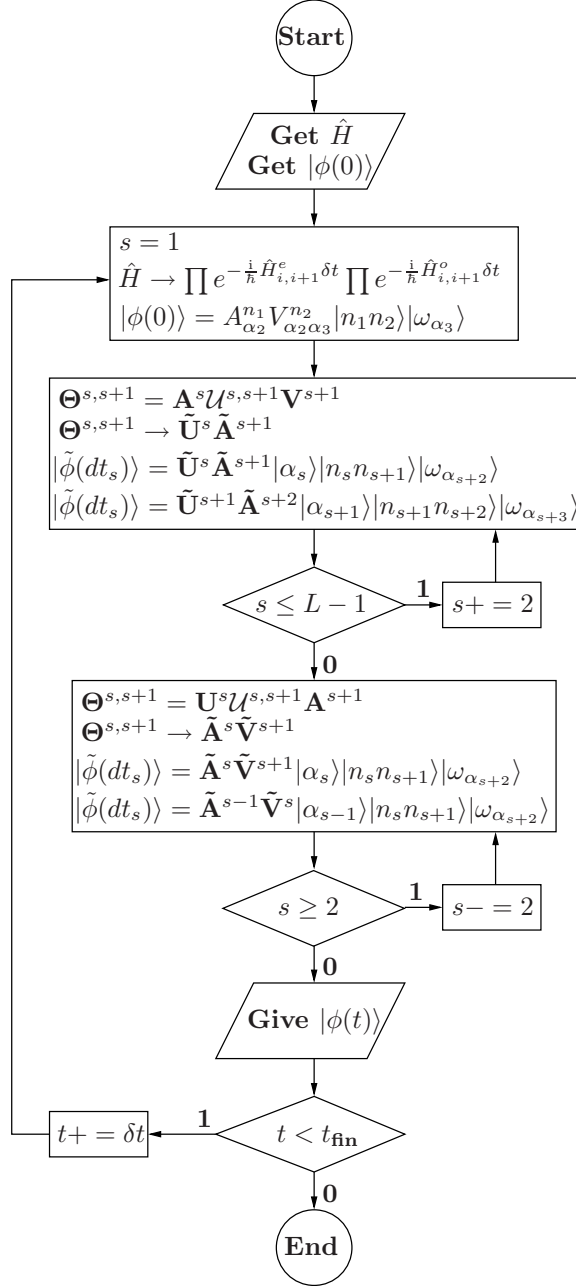


Figure VII.3: Flowchat of the TEBD algorithm.

where the state  $|\tilde{\alpha}_{s+1}\rangle = \tilde{U}_{\alpha_s \tilde{\alpha}_{s+1}}^{n_s} |\alpha_s\rangle |n_s\rangle$  holds

$$(VII.62) \quad \langle \tilde{\alpha}_{s+1} | \tilde{\alpha}'_{s+1} \rangle = \delta_{\tilde{\alpha}_{s+1}}^{\tilde{\alpha}'_{s+1}}.$$

9. The algorithm repeats the procedure from step (4) sweeping all the even and then odd sites.

### VII.2.f Ground state

The ground-state calculation is a variational method that takes the tensor elements of  $\mathbf{A}^s$  as variational parameters<sup>[172,177]</sup>. Consider that the energy of the system can be expressed as a function of the tensor related to the site  $s$  and that the state  $|\phi\rangle$  has been orthogonalized with the information concentrated at the same place. This assumption is expressed as

$$(VII.63) \quad E(\mathbf{A}^{\dagger s}) = \frac{\langle \phi(\mathbf{A}^{\dagger s}) | \hat{H} | \phi(\mathbf{A}^s) \rangle}{\langle \phi(\mathbf{A}^{\dagger s}) | \phi(\mathbf{A}^s) \rangle},$$

where the MPS state is

$$(VII.64) \quad |\phi(\mathbf{A}^s)\rangle = A_{\alpha_s \alpha_{s+1}}^{n_s} |\alpha_s\rangle |n_s\rangle |\omega_{\alpha_{s+1}}\rangle.$$

The denominator is quite straightforward and from Eq. (VII.49) gives

$$(VII.65) \quad \langle \phi(\mathbf{A}^{\dagger s}) | \phi(\mathbf{A}^s) \rangle = \vec{A}^{\dagger s} \cdot \vec{A}^s,$$

where the *vector*  $\vec{A}^s$  indicates that all the elements of the tensor  $\mathbf{A}^s$  have been piled up in a column and hence it has only one index  $\gamma \equiv \gamma(n_s \alpha_s \alpha_{s+1})$ . This way of writing the expected values is called *quadratic form*<sup>[178]</sup>.

The calculation of the quadratic form of the numerator is slightly more complicated and thus is shown below. However, the final result reads,

$$(VII.66) \quad \langle \phi(\mathbf{A}^{\dagger s}) | \hat{H} | \phi(\mathbf{A}^s) \rangle = \vec{A}^{\dagger s} \mathbf{H} \vec{A}^s,$$

where  $\mathbf{H}$  is a matrix with dimension  $\chi^2 d$  that fully represents the Hamiltonian. The ground state calculation with the variational method requires to minimize the energy, this condition leads to

$$(VII.67) \quad \begin{aligned} \frac{\partial E}{\partial \vec{A}^{\dagger s}} &= \frac{\partial}{\partial \vec{A}^{\dagger s}} \left[ \frac{\vec{A}^{\dagger s} \mathbf{H} \vec{A}^s}{\vec{A}^{\dagger s} \cdot \vec{A}^s} \right] \\ &= \frac{\left( \vec{A}^{\dagger s} \cdot \vec{A}^s \right) \mathbf{H} \vec{A}^s - \left( \vec{A}^{\dagger s} \mathbf{H} \vec{A}^s \right) \vec{A}^s}{\left( \vec{A}^{\dagger s} \cdot \vec{A}^s \right)^2} \\ &= \frac{\mathbf{H} \vec{A}^s - E \vec{A}^s}{\vec{A}^{\dagger s} \cdot \vec{A}^s} \\ &= 0 \end{aligned}$$

In other words, since we assume that  $\vec{A}^{\dagger s} \cdot \vec{A}^s \neq 0$ , being actually the unity for an orthonormalized state, the eigensystem

$$(VII.68) \quad \mathbf{H} \vec{A}^s = E \vec{A}^s,$$

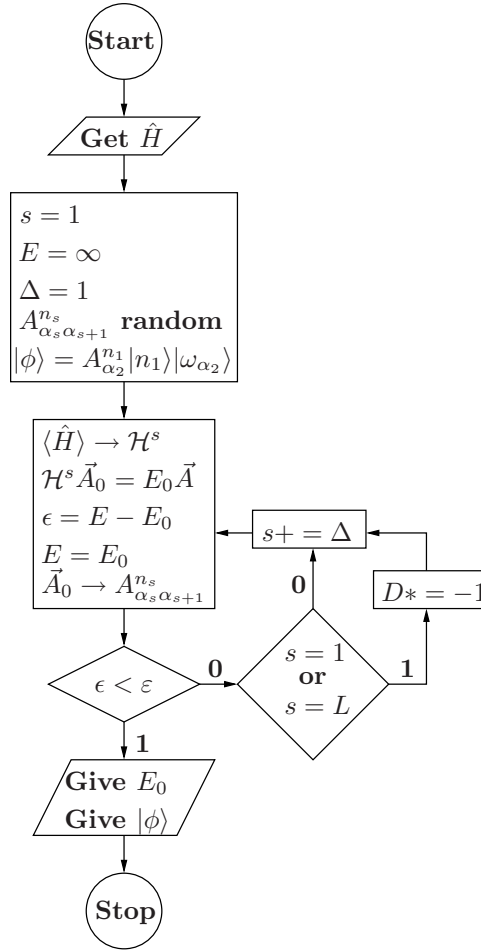


Figure VII.4: Flowchart of the variational method applied to the MPS ansatz for a given precision  $\epsilon$  and a Hamiltonian  $\hat{H}$ .

has to be solved in order to minimize the system energy. The eigenvector  $\vec{A}_0^s$  with the lowest eigenvalue  $E_0$  will provide the tensor elements for an updated version of the matrix  $\tilde{\mathbf{A}}^s$ . Then, the routine proceeds to orthogonalize the system by putting the information on the site  $s+1$  for instance, and calculates the new updates elements  $\tilde{\mathbf{A}}^{s+1}$ .

The algorithm is thus

1. Orthogonalize the system putting the information into the site  $s = 1$ .
2. Calculate the effective Hamiltonian for the site  $\mathbf{H}$  and solve the eigenproblem.
3. Take the eigenvector associated to the lowest eigenvalue in order to update the matrix  $\mathbf{A}^s$ .



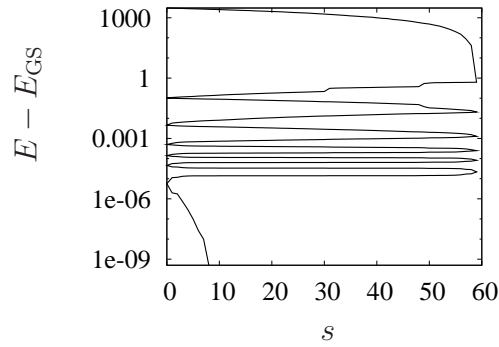


Figure VII.5: Energy convergence. The MPS variational procedure described in section VII.2.f shows an exponential convergence of the energy depicted in the plot where  $E$  is the variational energy and  $E_{\text{GS}}$  is the final value.

4. Orthogonalize the system moving the information to the next site, it can be either at the left or at the right depending on the swapping direction.
5. If the change in the energy  $E_0$  is below a given numerical threshold then stop, otherwise go to step 2.

This variational method offers the opportunity to calculate the ground state properties of Hamiltonians for which the Hilbert space is exponentially big with only a polynomially big ansatz. Furthermore, the convergence is exponentially fast as shown in the Fig. VII.5, making it a powerful tool for one-dimensional lattice Hamiltonians.

### Calculation of the Hamiltonian quadratic form

The quadratic form of the Hamiltonian depends on the system under consideration. As an example we consider the one-dimensional Bose-Hubbard Hamiltonian (1.4). Thus we have

$$\begin{aligned}
 \hat{H} &= \sum_i \left[ -t \left( \hat{b}_i^\dagger \hat{b}_{i+1} + \hat{b}_{i+1}^\dagger \hat{b}_i \right) + \frac{U}{2} \hat{n}_i (\hat{n}_i - 1) - \mu \hat{n}_i \right] \\
 &= \hat{H}_l + \hat{H}_{1s} + \hat{H}_s + \hat{H}_{sr} + \hat{H}_r,
 \end{aligned}
 \tag{VII.69}$$

with the definitions

$$\begin{aligned}
\hat{H}_l &= \sum_{i < s} \left[ \frac{U}{2} \hat{n}_i (\hat{n}_i - 1) + -\mu \hat{n}_i \right] - t \sum_{i < s-1} \left[ \hat{b}_i^\dagger \hat{b}_{i+1} + \text{h.c.} \right], \\
\hat{H}_{ls} &= -t \left( \hat{b}_{s-1}^\dagger \hat{b}_s + \text{h.c.} \right), \\
\hat{H}_s &= \frac{U}{2} \hat{n}_s (\hat{n}_s - 1) + (\epsilon_s - \mu) \hat{n}_s, \\
\hat{H}_{sr} &= -t \left( \hat{b}_{s+1}^\dagger \hat{b}_s + \text{h.c.} \right), \\
\hat{H}_r &= \sum_{i > s} \left[ \frac{U}{2} \hat{n}_i (\hat{n}_i - 1) + -\mu \hat{n}_i \right] - t \sum_{i > s} \left[ \hat{b}_i^\dagger \hat{b}_{i+1} + \text{h.c.} \right]
\end{aligned}
\tag{VII.70}$$

where the site  $s$  has been isolated and the system divided into three parts, the left (l) the right (r) and the site. Each local Hamiltonian has the corresponding subindex, and the interaction between the parts is indicated with double index, for instance  $ls$ , when considering the left part and the site. The quadratic form of the Hamiltonian comes from the expected value

$$\begin{aligned}
\langle \phi(\mathbf{A}^{\dagger s}) | \hat{H} | \phi(\mathbf{A}^s) \rangle &= A_{\alpha_s \alpha_{s+1}}^{n_s} A_{\alpha'_s \alpha'_{s+1}}^{n'_s \star} \langle \alpha'_s | \langle n'_s | \langle \omega'_{\alpha_{s+1}} | \hat{H} | \alpha_s \rangle | n_s \rangle | \omega_{\alpha_{s+1}} \rangle \\
&= A_{\alpha_s \alpha_{s+1}}^{n_s} A_{\alpha'_s \alpha'_{s+1}}^{n'_s \star} [\mathbf{H}]_{\alpha_s \alpha_{s+1} n_s}^{\alpha'_s \alpha'_{s+1} n'_s}
\end{aligned}
\tag{VII.71}$$

where using Eq. (VII.46) and (VII.40) we have

$$\begin{aligned}
[\mathbf{H}]_{\alpha_s \alpha_{s+1} n_s}^{\alpha'_s \alpha'_{s+1} n'_s} &= \langle \alpha'_s | \hat{H}_l | \alpha_s \rangle \delta_{n_s}^{n'_s} \delta_{\omega_{\alpha_{s+1}}}^{\omega_{\alpha'_{s+1}}} \\
&\quad + \text{Tr}_{\alpha_{s-1}} \left( \mathbf{E}^{s-1}(\hat{I}) \right) \langle n'_{s-1} n'_s | \hat{H}_{ls} | n_{s-1} n_s \rangle \delta_{\omega_{\alpha_{s+1}}}^{\omega_{\alpha'_{s+1}}} \\
&\quad + \langle n'_s | \hat{H}_s | n_s \rangle \delta_{\alpha_s}^{\alpha'_s} \delta_{\omega_{\alpha_{s+1}}}^{\omega_{\alpha'_{s+1}}} \\
&\quad + \text{Tr}_{\alpha_{s+2}} \left( \mathbf{E}^{s+1}(\hat{I}) \right) \langle n'_s n'_{s+1} | \hat{H}_{sr} | n_s n_{s+1} \rangle \delta_{\alpha_s}^{\alpha'_s} \\
&\quad + \langle \omega_{\alpha'_{s+1}} | \hat{H}_r | \omega_{\alpha_{s+1}} \rangle \delta_{n_s}^{n'_s} \delta_{\alpha_{s+1}}^{\alpha'_{s+1}}.
\end{aligned}
\tag{VII.72}$$

The terms  $\langle \alpha'_s | \hat{H}_l | \alpha_s \rangle$  and  $\langle \omega_{\alpha'_{s+1}} | \hat{H}_r | \omega_{\alpha_{s+1}} \rangle$  lead, of course, to similar expressions that can be used recursively in order to compute efficiently the quadratic form of the Hamiltonian. The typical terms are

$$\langle n'_s | \hat{H}_s | n_s \rangle = \left[ \frac{U}{2} n_s (n_s - 1) + (\epsilon_s - \mu) n_s \right] \delta_{n_s}^{n'_s},
\tag{VII.73}$$

and

$$\begin{aligned}
\langle n'_s n'_{s+1} | \hat{H}_{sr} | n_s n_{s+1} \rangle &= -t \left( \sqrt{n_s} \sqrt{n_{s+1} + 1} \delta_{n_s-1}^{n'_s} \delta_{n_{s+1}+1}^{n'_{s+1}} \right. \\
&\quad \left. + \sqrt{n_s + 1} \sqrt{n_{s+1}} \delta_{n_s+1}^{n'_s} \delta_{n_{s+1}-1}^{n'_{s+1}} \right).
\end{aligned}
\tag{VII.74}$$

## VII.3 Lanczos

The Lanczos algorithm is a technique that can be used to solve Hermitian sparse eigenproblems

$$(VII.75) \quad \mathbf{H}\vec{\phi} = E\vec{\phi},$$

when only the extreme eigenvalues are required. The method consists on successive applications of  $\mathbf{H}$  into an initial random vector  $\vec{\psi}$ . This process generates the basis  $\{\vec{\psi}_n\}$ , where  $\vec{\psi}_n = \mathbf{H}^n\vec{\psi}$ . Note that if  $n \rightarrow \infty$  then  $\psi_n/|\psi_n|$  tends to the eigenvector with the largest eigenvalue. Once this basis is orthogonalized by Gram-Schmidt decomposition the vectors  $\vec{\phi}^n$  are transformed into the *Lanczos* vectors that generate the so-called Krylov space. The Hamiltonian projection onto that space is a tri-diagonal matrix  $\mathbf{T}$  that can be solved by much simpler methods such as the QR decomposition<sup>[179]</sup>. When the number of elements in the Krylov space equals the dimension of the Hamiltonian matrix, the result is equivalent to a full diagonalization. However, one of the advantages of this method is that accurate enough information about the ground-state can be retrieved after a small number of iterations<sup>[180]</sup>.

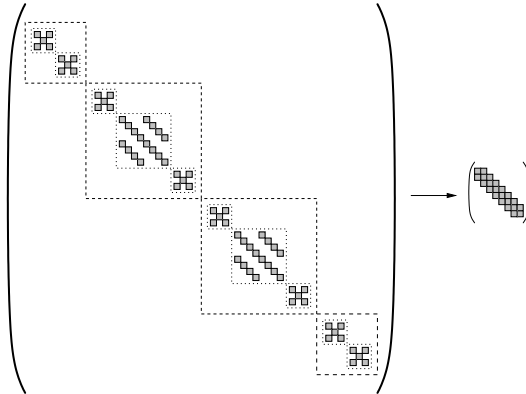


Figure VII.6: General structure of the Hamiltonian that may be solved by Lanczos. It is a sparse matrix and if there is a conserved quantity then it shows a block structure. The main idea is to take the relevant part and transform it into a tri-diagonal matrix.

In order to compare the power of the method, we recall that a full diagonalization of the system requires  $\mathcal{O}(d^3)$  operations, where  $d = \dim(\mathbf{H})$ . For the Lanczos algorithm, only matrix vector multiplication is required which goes like  $\mathcal{O}(d^2)$ . In the case of a sparse matrix, this quantity can be further reduced since not all operations are necessary to perform and therefore the algorithm scales as  $\sim \mathcal{O}(d)$ . The most expensive calculation we have performed was for the calculation of the ground state of a spin-1 chain with  $L = 16$  in chapter VI. In that example,  $d = 5.2 \times 10^6$ , which would require  $\mathcal{O}(1.2 \times 10^{20})$  operations with the full diagonalization technique.

Nowadays, several codes had been developed in order to implement the most efficient algorithm. One of those, ARPACK<sup>[181]</sup> has been used and implemented in our calculations. Although the main core of the algorithm is externally implemented, we provide the method with the most efficient way of computing the matrix vector multiplication  $\mathbf{H}\vec{\psi}$ . Besides that, several further implementations can be done in order to reduce the computational effort. Here, we list a few of the most straightforward methods.

Before going into the detail of the different implementations, it is worth to point out that the method depends strongly on the basis in which the Hamiltonian is written. As an example, let us consider a double-well system of spin-1/2 fermions. On each site, it is possible to have  $d = 4$  different states and thus  $d = 4^2$  total number of states for the whole system. Now, we can impose the different restrictions to the system:

					X	X	X
					X	✓	X
					✓	✓	X
					✓	X	✓
					✓	✓	✓

Figure VII.7: Total basis of two sites and spin-1/2 fermions. Depending on the restrictions done to the system, several elements are neglected. In this case, we restrict to  $N = 2$ ,  $S^z = 0$  within the Mott insulator of one particle per site.

- Particle number conservation:

The Hubbard Hamiltonian has the property that  $[\hat{H}, \hat{N}] = 0$  and therefore we can restrict ourselves to a manifold with constant number of particles. There are several procedures to conserve such quantity like using a chemical potential in a grand-canonical ensemble. However, if we work exactly in the canonical ensemble, the system dimension is reduced, as well as the possibility of error.

In the case of spinful particles, the condition of total conserved magnetization applies exactly in the same way as the conservation of particles.

- Symmetry implementation: Several non-trivial symmetries can be implemented in similar ways. In particular, as mentioned in chapter V, the spin-3/2 chain has a  $SU(2) \otimes SU(2)$  symmetry that is exploited to retrieve the ground state properties with the Lanczos method.

- Momentum conservation:

The translational symmetry of several Hamiltonians can be also useful in the reduction of the effective dimension of the problem. The main idea is to pack all the translationally equivalent states into one state that represents them all. The cost of this procedure comes when a state is retrieved and the routine has to search what class this state belongs to. This procedure can be very long if the basis is big. However, this problem can be solved if one expresses the Hamiltonian in the momentum space. Unfortunately, this may ruin the efficiency in the implementation of other symmetries. Nonetheless, this symmetry is particularly interesting when considering the problem of excitons formed on top of a polarized spin-3/2 chain in the Mott regime, as discussed in chapter III.



## Conclusions and outlook

In this Thesis, we have considered different problems regarding both polar bosons and spinor gases in one-dimensional optical lattices. We start in chapter I introducing the Bose-Hubbard Hamiltonian, analyzing by energy considerations (SCE) and correlation functions (MPS) the boundaries between the Mott insulator and the superfluid.

*In chapter II*, we have analyzed the physics of dipolar gases in unconnected parallel one-dimensional optical lattices<sup>[182]</sup>. The presence of the non-local dipole-dipole interaction between wires induces a direct Mott insulator to pair superfluid phase transition that distorts notoriously the shape of the Mott lobes. The most dramatic effect can be observed on the lowest Mott lobe boundary where for a critical strong attractive interaction it becomes constant as a function of the hopping and for an even stronger interaction it changes its slope. This sets a re-entrant configuration that is also present in higher dimensions and up to the second Mott lobe.

This particular effect leads to a highly non-trivial behavior of the Mott insulator plateaux in experiments with an axial harmonic confinement<sup>[183]</sup>. In fact, for small enough hopping, the Mott plateaux may become insensitive to the mobility of the particles, or even counter-intuitively, grow for larger hopping values.

It is also important to emphasize that these results apply to two-component Bose gases, and thus they lead to very interesting predictions for experiments in boson mixtures loaded into optical lattices, where the long-range interactions may give rise to exotic new states such as pair-super-solids<sup>[67,184]</sup>.

*In chapter III*, we studied that spin flips on top of a polarized repulsive high-spin Fermi gas may lead to formation of novel types of bound composites, which we illustrated for the case of 1D spin-3/2 hard-core fermions in the Mott phase. In that case the composites are formed by an exciton-like excitation and an anti-symmetric biexcitons-like one. Intriguing dynamics and stability properties of the composites result from a non-trivial interplay

between SCC, QZE and exciton momentum. We have explored and shown the high stability of the exciton gas against inelastic interactions. This opens exciting possibilities for the creation of intricate novel quantum composite phases.

In chapter V, we saw that spin-3/2 fermions present a rich diagram of Mott phases as a function of the scattering lengths and the QZE. Various types of phase transitions are predicted between a gapped dimerized phase, a gapless spin-liquid and an isotropic Heisenberg anti-ferromagnet. The latter phase occurs at large-enough QZE and is protected by a high  $SU(2) \otimes SU(2)$  symmetry which remains at any QZE, contrary to the case of spinor bosons.

These phases and phase transitions may be revealed in experiments with four-component fermions in optical lattices, under similar entropy and temperature requirements to those demanded for Néel ordering in spin-1/2 fermions in 3D lattices. This comes from the fact that the observation of the dimerized phase requires a temperature ( $T$ ) scale with an upper bound provided by the spin gap  $\Delta$ , which is maximal at  $g \sim 1$  and  $q = 0$ , being from our results  $\Delta \simeq t^2/g_0$ .

The different phases may be experimentally characterized by different means, including monitoring  $\tau$  in standard Stern-Gerlach-like experiments in time-of-flight, and using Faraday rotation<sup>[185]</sup>. Finally, note that with a shallow harmonic trap along the lattice, the MI phase occupies the central region, surface effects are negligible and our results apply.

In chapter VI, we have calculated the boundaries of the dimer phase in one-dimensional spin-1 chains with anti-ferromagnetic interactions under the influence of a external field that generates a quadratic Zeeman coupling. The calculations were done following the level crossing method and the spectra were calculated using the Lanczos exact diagonalization technique. The computational analysis of the system allows us to reduce both the matrix dimension and the number of operations required.

As a result three different regions are delimited. For a large enough and positive QZE, a XY-Nematic phase is found. By lowering the magnitude of the external field, an Kosterlitz-Thouless phase transition takes place and the ground state of the system transforms into a dimerized state. When crossing the line of zero external field, the manifold of local magnetization zero begins to be favored. As the QZE increases in absolute value, the state losses its  $m = \pm 1$  components and it transforms through a Ising phase transition into a polar state on the large- $D$  region.

The field induced phase transitions may be explored in  $^{23}\text{Na}$  which presents anti-ferromagnetic coupling. Besides, the external field that generates the quadratic Zeeman coupling may be controlled by microwave and optical techniques<sup>[186,187]</sup>.

We stress that such field-induced transitions are fundamentally precluded in spin-1/2 systems, due to the conservations of magnetization. Moreover, the



field-induced phase transitions discussed in this and the previous chapters, constitute a novel qualitative feature of spinor gases. we would like to note that similar transitions have been recently observed for spin-1 BEC's in the bulk<sup>[73,90]</sup>.

The results of this Thesis open interesting perspectives for future studies. Polar molecules in ladder-like potentials (as those studied in chapter II) may present pair-supersolid phases in presence of inter-rung interactions<sup>[67]</sup>. Other phases (as Haldane-like insulators) may occur in the presence of tunneling between the wires<sup>[188]</sup>.

The rich physics of spinor lattice gases in the presence of QZE has been only partially unveiled in chapters V and VI. An even richer physics may occur for higher fillings (i.e. Mott of 2 particles per site for spin-3/2 fermions) and for ladder-like potentials. Exciting new developments will surely follow in this sense.



## BIBLIOGRAPHY

- [1] I. Bloch, *Physics World* **17**, 25 (2004).
- [2] T. Rom, T. Best, O. Mandel, A. Widera, M. Greiner, T. W. Hänsch and I. Bloch, *Phys. Rev. Lett.* **93**, 073002 (2004).
- [3] I. Bloch, *Nat. Phys.* **1**, 23 (2005), ISSN 1745-2473.
- [4] M. P. A. Fisher, P. B. Weichman, G. Grinstein and D. S. Fisher, *Phys. Rev. B* **40**, 546 (1989).
- [5] D. Jaksch, C. Bruder, J. I. Cirac, C. W. Gardiner and P. Zoller, *Phys. Rev. Lett.* **81**, 3108 (1998).
- [6] M. Greiner, O. Mandel, T. Esslinger, T. W. Hansch and I. Bloch, *Nature* **415**, 39 (2002).
- [7] I. Bloch, J. Dalibard and W. Zwerger, *Rev. Mod. Phys.* **80**, 885 (2008).
- [8] R. Feynman, *Foundations of Physics* **16**, 507 (1986), ISSN 0015-9018, 10.1007/BF01886518.
- [9] S. N. Bose, *Zeitschrift für Physik* p. 178 (1924).
- [10] A. Einstein, *Sitzungsberichte der Preußischen Akademie der Wissenschaften* p. 261 (1924).
- [11] J. H. de Boer and E. J. W. Verwey, *Proceedings of the Physical Society* **49**, 59 (1937).
- [12] N. F. Mott and R. Peierls, *Proceedings of the Physical Society* **49**, 72 (1937).
- [13] J. Hubbard, *Proc. R. Soc. Lond. A* pp. 238–257 (1963).
- [14] E. H. Lieb and F. Y. Wu, *Phys. Rev. Lett.* **20**, 1445 (1968).

- [15] W. D. Phillips, *Rev. Mod. Phys.* **70**, 721 (1998).
- [16] P. D. Lett, R. N. Watts, C. I. Westbrook, W. D. Phillips, P. L. Gould and H. J. Metcalf, *Phys. Rev. Lett.* **61**, 169 (1988).
- [17] W. Ketterle and N. V. Druten, vol. 37 of *Advances In Atomic, Molecular, and Optical Physics*, pp. 181 – 236 (Academic Press, 1996).
- [18] Nobelprize.org, *The Nobel Prize in Physics 1997*, url-[http://nobelprize.org/nobel\\_prizes/physics/laureates/1997](http://nobelprize.org/nobel_prizes/physics/laureates/1997) (1997).
- [19] M. H. Anderson, J. R. Ensher, M. R. Matthews, C. E. Wieman and E. A. Cornell, *Science* **269**, 198 (1995).
- [20] K. B. Davis, M. O. Mewes, M. R. Andrews, N. J. van Druten, D. S. Durfee, D. M. Kurn and W. Ketterle, *Phys. Rev. Lett.* **75**, 3969 (1995).
- [21] Nobelprize.org, *The Nobel Prize in Physics 2001*, url-[http://nobelprize.org/nobel\\_prizes/physics/laureates/2001](http://nobelprize.org/nobel_prizes/physics/laureates/2001) (2001).
- [22] J. K. Freericks and H. Monien, *Phys. Rev. B* **53**, 2691 (1996).
- [23] C. Kollath, U. Schollwöck, J. von Delft and W. Zwerger, *Phys. Rev. A* **69**, 031601 (2004).
- [24] T. Lahaye, C. Menotti, L. Santos, M. Lewenstein and T. Pfau, *Reports on Progress in Physics* **72**, 126401 (2009).
- [25] S. Yi and L. You, *Phys. Rev. A* **61**, 041604 (2000).
- [26] K. Góral, K. Rzażewski and T. Pfau, *Phys. Rev. A* **61**, 051601 (2000).
- [27] L. Santos, G. V. Shlyapnikov, P. Zoller and M. Lewenstein, *Phys. Rev. Lett.* **85**, 1791 (2000).
- [28] S. Giovanazzi and D. H. J. O'Dell, *The European Physical Journal D - Atomic, Molecular, Optical and Plasma Physics* **31**, 439 (2004).
- [29] T. Lahaye, J. Metz, B. Fröhlich, T. Koch, M. Meister, A. Griesmaier, T. Pfau, H. Saito, Y. Kawaguchi and M. Ueda, *Phys. Rev. Lett.* **101**, 080401 (2008).
- [30] R. Nath, P. Pedri and L. Santos, *Phys. Rev. Lett.* **102**, 050401 (2009).
- [31] M. Peccianti, C. Conti, G. Assanto, A. De Luca and C. Umeton, *Nature* **432**, 733 (2004).
- [32] P. Pedri and L. Santos, *Phys. Rev. Lett.* **95**, 200404 (2005).

- [33] I. Tikhonenkov, B. A. Malomed and A. Vardi, *Phys. Rev. Lett.* **100**, 090406 (2008).
- [34] R. Nath, P. Pedri and L. Santos, *Phys. Rev. Lett.* **101**, 210402 (2008).
- [35] L. Santos, G. V. Shlyapnikov and M. Lewenstein, *Phys. Rev. Lett.* **90**, 250403 (2003).
- [36] S. Komineas and N. R. Cooper, *Phys. Rev. A* **75**, 023623 (2007).
- [37] S. Ronen, D. C. E. Bortolotti and J. L. Bohn, *Phys. Rev. Lett.* **98**, 030406 (2007).
- [38] M. Baranov, *Physics Reports* **464**, 71 (2008), ISSN 0370-1573.
- [39] M. A. Baranov, M. S. Mar'enko, V. S. Rychkov and G. V. Shlyapnikov, *Phys. Rev. A* **66**, 013606 (2002).
- [40] M. A. Baranov, L. Dobrek and M. Lewenstein, *Phys. Rev. Lett.* **92**, 250403 (2004).
- [41] G. M. Bruun and E. Taylor, *Phys. Rev. Lett.* **101**, 245301 (2008).
- [42] N. R. Cooper and G. V. Shlyapnikov, *Phys. Rev. Lett.* **103**, 155302 (2009).
- [43] J. Quintanilla, S. T. Carr and J. J. Betouras, *Phys. Rev. A* **79**, 031601 (2009).
- [44] K. Góral, L. Santos and M. Lewenstein, *Phys. Rev. Lett.* **88**, 170406 (2002).
- [45] M. A. Baranov, K. Osterloh and M. Lewenstein, *Phys. Rev. Lett.* **94**, 070404 (2005).
- [46] E. H. Rezayi, N. Read and N. R. Cooper, *Phys. Rev. Lett.* **95**, 160404 (2005).
- [47] H. P. Büchler, E. Demler, M. Lukin, A. Micheli, N. Prokof'ev, G. Pupillo and P. Zoller, *Phys. Rev. Lett.* **98**, 060404 (2007).
- [48] C. Menotti, C. Trefzger and M. Lewenstein, *Phys. Rev. Lett.* **98**, 235301 (2007).
- [49] S. Y. T. van de Meerakker, H. L. Bethlem and G. Meijer, *Nat. Phys.* **4**, 595 (2008).
- [50] J. M. Doyle, B. Friedrich, J. Kim and D. Patterson, *Phys. Rev. A* **52**, R2515 (1995).

- [51] J. D. Weinstein, R. deCarvalho, T. Guillet, B. Friedrich and J. M. Doyle, *Nature* **395**, 148 (1998).
- [52] D. Egorov, T. Lahaye, W. Schöllkopf, B. Friedrich and J. M. Doyle, *Phys. Rev. A* **66**, 043401 (2002).
- [53] S. Ospelkaus, A. Pe'er, K.-K. Ni, J. J. Zirbel, B. Neyenhuis, S. Kotochigova, P. S. Julienne, J. Ye and D. S. Jin, *Nat Phys* **4**, 622 (2008), ISSN 1745-2473.
- [54] K.-K. Ni, S. Ospelkaus, M. H. G. de Miranda, A. Pe'er, B. Neyenhuis, J. J. Zirbel, S. Kotochigova, P. S. Julienne, D. S. Jin and J. Ye, *Science* **322**, 231 (2008).
- [55] T. Köhler, K. Góral and P. S. Julienne, *Rev. Mod. Phys.* **78**, 1311 (2006).
- [56] J. Deiglmayr, A. Grochola, M. Repp, K. Mörtlbauer, C. Glück, J. Lange, O. Dulieu, R. Wester and M. Weidemüller, *Phys. Rev. Lett.* **101**, 133004 (2008).
- [57] K.-K. Ni, S. Ospelkaus, D. Wang, G. Quemener, B. Neyenhuis, M. H. G. de Miranda, J. L. Bohn, J. Ye and D. S. Jin, *Nature* **464**, 1324 (2010), ISSN 0028-0836.
- [58] K. Góral and L. Santos, *Phys. Rev. A* **66**, 023613 (2002).
- [59] C. Bruder, R. Fazio and G. Schön, *Phys. Rev. B* **47**, 342 (1993).
- [60] A. van Otterlo and K.-H. Wagenblast, *Phys. Rev. Lett.* **72**, 3598 (1994).
- [61] G. G. Batrouni, R. T. Scalettar, G. T. Zimanyi and A. P. Kampf, *Phys. Rev. Lett.* **74**, 2527 (1995).
- [62] E. G. Dalla Torre, E. Berg and E. Altman, *Phys. Rev. Lett.* **97**, 260401 (2006).
- [63] F. D. M. Haldane, *Phys. Rev. Lett.* **50**, 1153 (1983).
- [64] L. Amico, G. Mazzearella, S. Pasini and F. S. Cataliotti, *New Journal of Physics* **12**, 013002 (2010).
- [65] M. Horikoshi and K. Nakagawa, *Applied Physics B: Lasers and Optics* **82**, 363 (2006), ISSN 0946-2171, 10.1007/s00340-005-2083-z.
- [66] J. Sebby-Strabley, M. Anderlini, P. S. Jessen and J. V. Porto, *Phys. Rev. A* **73**, 033605 (2006).

- [67] C. Trefzger, C. Menotti and M. Lewenstein, *Phys. Rev. Lett.* **103**, 035304 (2009).
- [68] A. Kuklov, N. Prokof'ev and B. Svistunov, *Phys. Rev. Lett.* **92**, 050402 (2004).
- [69] G. G. Batrouni, V. Rousseau, R. T. Scalettar, M. Rigol, A. Muramatsu, P. J. H. Denteneer and M. Troyer, *Phys. Rev. Lett.* **89**, 117203 (2002).
- [70] R. Jördens, N. Strohmaier, K. Gunter, H. Moritz and T. Esslinger, *Nature* **455**, 204 (2008).
- [71] U. Schneider, L. Hackermüller, S. Will, T. Best, I. Bloch, T. A. Costi, R. W. Helmes, D. Rasch and A. Rosch, *Science* **322**, 1520 (2008).
- [72] T.-L. Ho, *Phys. Rev. Lett.* **81**, 742 (1998).
- [73] L. E. Sadler, J. M. Higbie, S. R. Leslie, M. Vengalattore and D. M. Stamper-Kurn, *Nature* **443**, 312 (2006).
- [74] C. Klempt, O. Topic, G. Gebreyesus, M. Scherer, T. Henninger, P. Hyllus, W. Ertmer, L. Santos and J. J. Arlt, *Phys. Rev. Lett.* **104**, 195303 (2010).
- [75] D. M. Stamper-Kurn, M. R. Andrews, A. P. Chikkatur, S. Inouye, H.-J. Miesner, J. Stenger and W. Ketterle, *Phys. Rev. Lett.* **80**, 2027 (1998).
- [76] H. Schmaljohann, M. Erhard, J. Kronjäger, M. Kottke, S. van Staa, L. Cacciapuoti, J. J. Arlt, K. Bongs and K. Sengstock, *Phys. Rev. Lett.* **92**, 040402 (2004).
- [77] N. N. Klausen, J. L. Bohn and C. H. Greene, *Phys. Rev. A* **64**, 053602 (2001).
- [78] A. Griesmaier, J. Werner, S. Hensler, J. Stuhler and T. Pfau, *Phys. Rev. Lett.* **94**, 160401 (2005).
- [79] M. Koashi and M. Ueda, *Phys. Rev. Lett.* **84**, 1066 (2000).
- [80] W. Zhang, S. Yi and L. You, *New Journal of Physics* **5**, 77 (2003).
- [81] C. K. Law, H. Pu and N. P. Bigelow, *Phys. Rev. Lett.* **81**, 5257 (1998).
- [82] E. V. Goldstein and P. Meystre, *Phys. Rev. A* **59**, 3896 (1999).
- [83] H. Pu, C. K. Law, S. Raghavan, J. H. Eberly and N. P. Bigelow, *Phys. Rev. A* **60**, 1463 (1999).

- [84] J. P. Burke, P. S. Julienne, C. J. Williams, Y. B. Band and M. Trippenbach, *Phys. Rev. A* **70**, 033606 (2004).
- [85] D. R. Romano and E. J. V. de Passos, *Phys. Rev. A* **70**, 043614 (2004).
- [86] W. Zhang, D. L. Zhou, M.-S. Chang, M. S. Chapman and L. You, *Phys. Rev. A* **72**, 013602 (2005).
- [87] T. Ohmi and K. Machida, *Journal of the Physical Society of Japan* **67**, 1822 (1998).
- [88] A. E. Leanhardt, Y. Shin, D. Kielpinski, D. E. Pritchard and W. Ketterle, *Phys. Rev. Lett.* **90**, 140403 (2003).
- [89] T. Isoshima, K. Machida and T. Ohmi, *Phys. Rev. A* **60**, 4857 (1999).
- [90] J. Stenger, S. Inouye, D. M. Stamper-Kurn, H.-J. Miesner, A. P. Chikkatur and W. Ketterle, *Nature* **396**, 345 (1998).
- [91] L.-M. Duan, J. I. Cirac and P. Zoller, *Phys. Rev. A* **65**, 033619 (2002).
- [92] H. Pu and P. Meystre, *Phys. Rev. Lett.* **85**, 3987 (2000).
- [93] A. N. Wenz, T. Lompe, T. B. Ottenstein, F. Serwane, G. Zürn and S. Jochim, *Phys. Rev. A* **80**, 040702 (2009).
- [94] L.-W. He, C. E. Burkhardt, M. Ciocca, J. J. Leventhal and S. T. Manson, *Phys. Rev. Lett.* **67**, 2131 (1991).
- [95] T. Fukuhara, Y. Takasu, M. Kumakura and Y. Takahashi, *Phys. Rev. Lett.* **98**, 030401 (2007).
- [96] C. Honerkamp and W. Hofstetter, *Phys. Rev. Lett.* **92**, 170403 (2004).
- [97] T. Paananen, J.-P. Martikainen and P. Törmä, *Phys. Rev. A* **73**, 053606 (2006).
- [98] A. Rapp, G. Zaránd, C. Honerkamp and W. Hofstetter, *Phys. Rev. Lett.* **98**, 160405 (2007).
- [99] R. W. Cherg, G. Refael and E. Demler, *Phys. Rev. Lett.* **99**, 130406 (2007).
- [100] X. W. Guan, M. T. Batchelor, C. Lee and H.-Q. Zhou, *Phys. Rev. Lett.* **100**, 200401 (2008).
- [101] C. Wu, J.-p. Hu and S.-c. Zhang, *Phys. Rev. Lett.* **91**, 186402 (2003).



- [102] S. Capponi, G. Roux, P. Azaria, E. Boulat and P. Lecheminant, *Phys. Rev. B* **75**, 100503 (2007).
- [103] D. Controzzi and A. M. Tsvelik, *Phys. Rev. Lett.* **96**, 097205 (2006).
- [104] S. Capponi, G. Roux, P. Lecheminant, P. Azaria, E. Boulat and S. R. White, *Phys. Rev. A* **77**, 013624 (2008).
- [105] G. Roux, S. Capponi, P. Lecheminant and P. Azaria, *The European Physical Journal B - Condensed Matter and Complex Systems* **68**, 293 (2009), ISSN 1434-6028, 10.1140/epjb/e2008-00374-7.
- [106] F. Werner, O. Parcollet, A. Georges and S. R. Hassan, *Phys. Rev. Lett.* **95**, 056401 (2005).
- [107] M. A. Cazalilla, A. F. Ho and M. Ueda, *New Journal of Physics* **11**, 103033 (2009).
- [108] A. V. Gorshkov, M. Hermele, V. Gurarie, C. Xu, P. S. Julienne, J. Ye, P. Zoller, E. Demler, M. D. Lukin and A. M. Rey, *Nature Physics* **6**, 289 (2010).
- [109] P. Lecheminant, E. Boulat and P. Azaria, *Phys. Rev. Lett.* **95**, 240402 (2005).
- [110] C. Wu, *Phys. Rev. Lett.* **95**, 266404 (2005).
- [111] L. Gerland, L. Frankfurt, M. Strikman, H. Stöcker and W. Greiner, *Phys. Rev. Lett.* **81**, 762 (1998).
- [112] M.-S. Chang, C. D. Hamley, M. D. Barrett, J. A. Sauer, K. M. Fortier, W. Zhang, L. You and M. S. Chapman, *Phys. Rev. Lett.* **92**, 140403 (2004).
- [113] C. Klempt, O. Topic, G. Gebreyesus, M. Scherer, T. Henninger, P. Hylus, W. Ertmer, L. Santos and J. J. Arlt, *Phys. Rev. Lett.* **103**, 195302 (2009).
- [114] H.-H. Tu, G.-M. Zhang and L. Yu, *Phys. Rev. B* **74**, 174404 (2006).
- [115] K. Eckert, L. Zawitkowski, M. J. Leskinen, A. Sanpera and M. Lewenstein, *New Journal of Physics* **9**, 133 (2007).
- [116] D. J. Papoular, G. V. Shlyapnikov and J. Dalibard, *Phys. Rev. A* **81**, 041603 (2010).
- [117] P. O. Fedichev, Y. Kagan, G. V. Shlyapnikov and J. T. M. Walraven, *Phys. Rev. Lett.* **77**, 2913 (1996).

- [118] B. Sutherland, *Phys. Rev. B* **12**, 3795 (1975).
- [119] M. R. Hoffmann, *J. Phys. Chem.* **100**, 6125 (1996).
- [120] M. Greiner, C. A. Regal and D. S. Jin, *Nature* **426**, 537 (2003).
- [121] S. Jochim, M. Bartenstein, A. Altmeyer, G. Hendl, S. Riedl, C. Chin, J. H. Denschlag and R. Grimm, *Science* **302**, 2101 (2003).
- [122] M. Lewenstein, L. Santos, M. A. Baranov and H. Fehrmann, *Phys. Rev. Lett.* **92**, 050401 (2004).
- [123] K. Winkler, G. Thalhammer, F. Lang, R. Grimm, J. Hecker Denschlag, A. J. Daley, A. Kantian, H. P. Büchler and P. Zoller, *Nature* **441**, 853 (2006).
- [124] N. Strohmaier, D. Greif, R. Jördens, L. Tarruell, H. Moritz, T. Esslinger, R. Sensarma, D. Pekker, E. Altman and E. Demler, *Phys. Rev. Lett.* **104**, 080401 (2010).
- [125] R. Sensarma, D. Pekker, M. D. Lukin and E. Demler, *Phys. Rev. Lett.* **103**, 035303 (2009).
- [126] S. D. Huber and A. Rüegg, *Phys. Rev. Lett.* **102**, 065301 (2009).
- [127] F. Hassler, A. Rüegg, M. Sigrist and G. Blatter, *Phys. Rev. Lett.* **104**, 220402 (2010).
- [128] K. A. Al-Hassanieh, F. A. Reboredo, A. E. Feiguin, I. González and E. Dagotto, *Phys. Rev. Lett.* **100**, 166403 (2008).
- [129] L. G. G. V. Dias da Silva, K. A. Al-Hassanieh, A. E. Feiguin, F. A. Reboredo and E. Dagotto, *Phys. Rev. B* **81**, 125113 (2010).
- [130] F. Heidrich-Meisner, S. R. Manmana, M. Rigol, A. Muramatsu, A. E. Feiguin and E. Dagotto, *Phys. Rev. A* **80**, 041603 (2009).
- [131] J.-P. Nguenang and S. Flach, *Phys. Rev. A* **80**, 015601 (2009).
- [132] W. S. Bakr, J. I. Gillen, A. Peng, S. Folling and M. Greiner, *Nature* **462**, 74 (2009).
- [133] J. F. Sherson, C. Weitenberg, M. Endres, M. Cheneau, I. Bloch and S. Kuhr, *Nature* **467**, 68 (2010).
- [134] R. Jördens, L. Tarruell, D. Greif, T. Uehlinger, N. Strohmaier, H. Moritz, T. Esslinger, L. De Leo, C. Kollath, A. Georges, V. Scarola, L. Pollet, E. Burovski, E. Kozik and M. Troyer, *Phys. Rev. Lett.* **104**, 180401 (2010).

- [135] A. Koetsier, R. A. Duine, I. Bloch and H. T. C. Stoof, *Phys. Rev. A* **77**, 023623 (2008).
- [136] J. Catani, G. Barontini, G. Lamporesi, F. Rabatti, G. Thalhammer, F. Minardi, S. Stringari and M. Inguscio, *Phys. Rev. Lett.* **103**, 140401 (2009).
- [137] J.-S. Bernier, C. Kollath, A. Georges, L. De Leo, F. Gerbier, C. Salomon and M. Köhl, *Phys. Rev. A* **79**, 061601 (2009).
- [138] C. Wu, *Modern Physics Letters B* **20**, 1707 (2006).
- [139] T. Itakura and N. Kawakami, *Journal of the Physical Society of Japan* **64**, 2321 (1995).
- [140] K. Rodríguez, A. Argüelles, M. Colomé-Tatché, T. Vekua and L. Santos, *Phys. Rev. Lett.* **105**, 050402 (2010).
- [141] K. Rodríguez, *Non-equilibrium Dynamics and Quantum Magnetism in 1D Optical Lattices*, Ph.D. thesis, Leibniz Hannover University (2010).
- [142] K. Okamoto and K. Nomura, *Physics Letters A* **169**, 433 (1992), ISSN 0375-9601.
- [143] K. Nomura and K. Okamoto, *Journal of Physics A: Mathematical and General* **27**, 5773 (1994).
- [144] T. Vekua and A. Honecker, *Phys. Rev. B* **73**, 214427 (2006).
- [145] T. Giamarchi, *Quantum Physics in One Dimension* (Oxford University Press, 2004).
- [146] T. Giamarchi and H. J. Schulz, *J. Phys. France* **49**, 819 (1988).
- [147] M. D. Barrett, J. A. Sauer and M. S. Chapman, *Phys. Rev. Lett.* **87**, 010404 (2001).
- [148] M. Snoek and F. Zhou, *Phys. Rev. B* **69**, 094410 (2004).
- [149] K. Harada, N. Kawashima and M. Troyer, *Journal of the Physical Society of Japan* **76**, 013703 (2007).
- [150] E. Demler and F. Zhou, *Phys. Rev. Lett.* **88**, 163001 (2002).
- [151] S. K. Yip, *Phys. Rev. Lett.* **90**, 250402 (2003).
- [152] F. Zhou and M. Snoek, *Annals of Physics* **308**, 692 (2003), ISSN 0003-4916.

- [153] A. Imambekov, M. Lukin and E. Demler, *Phys. Rev. A* **68**, 063602 (2003).
- [154] M. Rizzi, D. Rossini, G. De Chiara, S. Montangero and R. Fazio, *Phys. Rev. Lett.* **95**, 240404 (2005).
- [155] A. V. Chubukov, *Journal of Physics: Condensed Matter* **2**, 1593 (1990).
- [156] A. V. Chubukov, *Phys. Rev. B* **43**, 3337 (1991).
- [157] G. Fáth and J. Sólyom, *Phys. Rev. B* **51**, 3620 (1995).
- [158] C. D. Batista, G. Ortiz and J. E. Gubernatis, *Phys. Rev. B* **65**, 180402 (2002).
- [159] J. J. García-Ripoll, M. A. Martin-Delgado and J. I. Cirac, *Phys. Rev. Lett.* **93**, 250405 (2004).
- [160] O. Romero-Isart, K. Eckert and A. Sanpera, *Phys. Rev. A* **75**, 050303 (2007).
- [161] A. Klümper, *EPL (Europhysics Letters)* **9**, 815 (1989).
- [162] M. N. Barber and M. T. Batchelor, *Phys. Rev. B* **40**, 4621 (1989).
- [163] L. A. Takhtajan, *Physics Letters A* **87**, 479 (1982), ISSN 0375-9601.
- [164] H. M. Babujian, *Physics Letters A* **90**, 479 (1982), ISSN 0375-9601.
- [165] I. Affleck, T. Kennedy, E. H. Lieb and H. Tasaki, *Phys. Rev. Lett.* **59**, 799 (1987).
- [166] A. Imambekov, M. Lukin and E. Demler, *Phys. Rev. Lett.* **93**, 120405 (2004).
- [167] M.-C. Chung and S. Yip, *Phys. Rev. A* **80**, 053615 (2009).
- [168] N. Papanicolaou, *Nuclear Physics B* **305**, 367 (1988), ISSN 0550-3213.
- [169] K. R. guez, A. Argüelles, A. K. Kolezhuk, L. Santos and T. Vekua, *arXiv: 1009.3875v1*, 1 (2010).
- [170] V. E. Korepin, *Phys. Rev. Lett.* **92**, 096402 (2004).
- [171] S. R. White, *Phys. Rev. Lett.* **69**, 2863 (1992).
- [172] F. Verstraete, D. Porras and J. I. Cirac, *Phys. Rev. Lett.* **93**, 227205 (2004).

- [173] N. Schuch and J. I. Cirac, Phys. Rev. A **82**, 012314 (2010).
- [174] G. Vidal, Phys. Rev. Lett. **93**, 040502 (2004).
- [175] G. Vidal, Phys. Rev. Lett. **91**, 147902 (2003).
- [176] A. Ekert and P. L. Knight, American Journal of Physics **63**, 415 (1995).
- [177] F. Verstraete, J. J. García-Ripoll and J. I. Cirac, Phys. Rev. Lett. **93**, 207204 (2004).
- [178] J. J. García-Ripoll, New Journal of Physics **8**, 305 (2006).
- [179] W. H. Press, S. A. Teukolsky, W. T. Vetterling and B. P. Flannery, *Numerical Recipes 3rd Edition: The Art of Scientific Computing* (Cambridge University Press, 2007), 3 ed., ISBN 0521880688.
- [180] E. Dagotto, Rev. Mod. Phys. **66**, 763 (1994).
- [181] R. B. Lehoucq, D. C. Sorensen and C. Yang, *ARPACK Users' Guide: Solution of Large Scale Eigenvalue Problems with Implicitly Restarted Arnoldi Methods* (Society of Industrial and Applied Mathematics, 1998).
- [182] A. Argüelles and L. Santos, Phys. Rev. A **75**, 053613 (2007).
- [183] S. Fölling, A. Widera, T. Müller, F. Gerbier and I. Bloch, Phys. Rev. Lett. **97**, 060403 (2006).
- [184] M. Iskin and J. K. Freericks, Phys. Rev. A **79**, 053634 (2009).
- [185] K. Eckert, O. Romero-Isart, M. Rodriguez, M. Lewenstein, E. S. Polzik and A. Sanpera, Nat. Phys. **4**, 50 (2008), ISSN 1745-2473.
- [186] F. Gerbier, A. Widera, S. Fölling, O. Mandel and I. Bloch, Phys. Rev. A **73**, 041602 (2006).
- [187] L. Santos, M. Fattori, J. Stuhler and T. Pfau, Phys. Rev. A **75**, 053606 (2007).
- [188] X. Deng, T. Vekua and L. Santos, *In preparation*.



## List of publications

1. K. Rodríguez, A. Argüelles, M. Colomé-Tatché, T. Vekua and L. Santos, *Mott-Insulator Phases of Spin-3/2 Fermions in the Presence of Quadratic Zeeman Coupling*, Phys. Rev. Lett. **105**, 050402 (2010).
2. A. Argüelles and L. Santos, *Repulsively-bound exciton-biexciton states in high-spin fermions in optical lattices*, arXiv:1011.0388v3 [cond-mat.quant-gas] (2010).
3. K. Rodríguez, A. Argüelles, A. K. Kolezhuk, L. Santos and T. Vekua, *Field-induced phase transitions of repulsive spin-1 bosons in optical lattices*, arXiv:1009.3875v1 [cond-mat.quant-gas] (2010).
4. A. Argüelles and L. Santos, *Mott-insulator phases of nonlocally coupled one-dimensional dipolar Bose gases*, Phys. Rev. A **75**, 053613 (2007).

Other publications of the author:

1. A. Argüelles and T. Dittrich, *Wigner function for discrete phase space: Exorcising ghost images*, Physica A: Statistical Mechanics and its Applications **356**, 72 (2005).





## Acknowledgements

When every author reaches this point, realizes that to thank the people involved in the project in whatever order, is always unfair. Thinking about it, I realized that this comes because the help, the support, the advise and the encouragement, from different persons, are all together in a mixture that keeps building research, even though, not all contributions were scientific. Therefore dear reader, do not feel offended if you are not in the first places of the list or even worse if you are there at all!

However at first, I would like to express my fond gratitude to the person who was not only the leading head of my research group, but also a model as a scientist, as person and always a friend, Prof. Luis Santos. Many, many thanks. My immense gratitude does not come only for the pages I wrote in this Thesis. It comes from your warmth welcome to your research group and to the exotic and always amazing field of ultracold gases. Of course, I would not miss the opportunity to extend my gratitude to your family members that made, without any doubt, both Stuttgart and Hannover happier places to live. Rocio, Noah, Alba... and Lucky... thanks a lot for all those delicious afternoons and evenings spent cooking and playing.

The time here in Germany, this work, what I learnt, all is just a blink in comparison with the journey I am doing. Fortunately, I am not alone on it. There is my soul-mate, my wife, my college, my partner Karen Rodríguez. All of this would not be the same without your special company. I am truly thankful for all the moments, in and outside the institute, and I am already looking forward to take the next step always with you.

I am also very thankful to Prof. Temo Vekua since great part of this work was highly boosted by his ideas and encouragement. Several fruitful discussions were held that opened a wider insight into the problems we were considering. Furthermore, I would like to acknowledge also his refereeing of this Thesis. And last but not least, I would like to recognize his and Debra Noe's hospitality and friendship.

I would like to mention that the core of the results from the present work were obtained by elaborated numerical procedures. In this respect, I regard the

patience and knowledge from both J. García-Ripoll, from whom I learn the MPS algorithms and optimization procedures, and S. Weßel, whose *ula* was behind any matrix manipulation used throughout the Thesis.

I would like to express my gratitude to Prof. Wolfgang Ertmer, whose hard work in the SFB407 and QUEST allowed me to learn not only from Hannover, but also from several interesting places where many conferences were held.

Of course, I cannot forget to thank my fellows and friends that made the different institutes a enjoyable place for working, not only due to the interesting physics discussions but also for the entertaining chats. First of all, my long standing former roommate Rejish Nath. Philipp Hyllus for the German-Spanish exchange. Giovanni Mazzarella and Garu Gabrayesus for the nice visits at home. Ulrich Ebling, Mattia Jona Lasinio, María Colomé and Jörg Duhme for many activities and, of course, Alexander Pikovski for the pleasant coffee-breaks and for providing the German version of the abstract, and Michael and Maria Klawunn for the unforgettable moments. Besides them, Prof. A. Muramatsu, S. Manmana, J. Falb, S. Sinha, S. Harrer, F. Karim and A. Jacob from Stuttgart and N. Bornemann, K. Lakomy, S. Aloui, F. Deuretzbacher, A. Grabinski and all the people from the ITP in Hannover. Also, the nice people of the IQO which made of both the initiation club and the Denmark trips, the best way to learn physics.

Since big part of my work was done in computers, I am really thankful for the help and support of Catia Lavalle, Carsten von Zobeltitz, Alex Cojuhovski and Jan Grelik. For the administrative part, I would like to thank Idilko Poljak, Gitta Richter and Catharina Bolz from whom I got all the help I needed to solve countless bureaucracy details.

I want to dedicate a little space for all the people that was part of my non-academic life. Among them, the Nano- and Festkörperphysik groups for the soccer matches and my fellows in the capoeira training.

Finally, I want to say thank you to my family and friends that always support and encourage me to pursuit my dreams. In particular, to my parents and my wife.

## Curriculum Vitae

Address : Marienstr. 7, 30171 Hannover, Germany  
Phone : +49(0)511 762 4836(office)  
          +49(0)176 93110854(mobile)  
Email : arturo@itp.uni-hannover.de  
Homepage : <http://www.itp.uni-hannover.de/arturo/>

### Personal profile

Date of Birth : 28th February 1978  
Place of Birth : Bogotá, Colombia  
Gender : Male  
Marital Status : Married  
Nationality : Colombian  
Language : Spanish, English, German

### Education

2006 - 2011      PhD  
                    Leibniz Hannover University, Hannover, Germany  
2005 - 2006      Research assistant  
                    Stuttgart University, Stuttgart, Germany  
2001 - 2005      Master of science - Physics  
                    National University of Colombia, Bogotá, Colombia  
1996 - 2001      B. Sc. Physics  
                    National University of Colombia, Bogotá, Colombia  
1989 - 1994      Secondary school. Programming technician  
                    Central Technical Institute, Bogotá, Colombia  
1984 - 1988      Primary school



## Selbstständigkeitserklärung

Hiermit versichere ich, die vorliegende Doktorarbeit selbstständig und unter ausschließlicher Verwendung der angegebenen Hilfsmittel angefertigt zu haben.

Hannover, den 2. Februar 2011

---

Arturo Argüelles